Silicate melt inclusions in the new millennium: A review of recommended practices for preparation, analysis, and data presentation

Rose-Koga EF[1], Bouvier A-S[2], Gaetani GA[3], Wallace PJ[4], Allison CM[5], Andrys JA[6], Angeles de la Torre CA[7], Barth A[8], Bodnar RJ[9], Bracco Gartner AJJ[10], Butters DA[11], Castillejo A[3], Chilson-Parks B[12], Choudhary BR[13], Cluzel N[1], Cole M[14], Cottrell E[15], Daly A[3], Danyushevsky LV[16], DeVitre CL[5], Drignon MJ[17], France L[18], Gaborieau M[1], Garcia MO[19], Gatti E[20], Genske FS[21], Hartley ME[22], Hughes EC[20], Iveson AA[23], Johnson ER[14], Jones M[3], Kagoshima T[24], Katzir Y[25], Kawaguchi M[1,44], Kawamoto T[26], Kelley KA[6], Koornneef JM[10], Kurz MD[3], Laubier M[1], Layne GD[27], Lerner A[4], Lin K-Y[28], Liu P.-P.[29], Lorenzo-Merino A[30], Luciani N[10], Magalhães N[31,32], Marschall HR[33], Michael PJ[34], Monteleone BD[3], Moore LR[9], Moussallam Y[1,8], Muth M[4], Myers ML[1], Narvaez DF[1], Navon O[35], Newcombe ME[31], Nichols ARL[36], Nielsen RL[17,41], Pamukcu A[3], Plank T[8], Rasmussen DJ[8], Roberge J[7], Schiavi F[1], Schwartz DM[37], Shimizu Kei[38], Shimizu K[39], Shimizu N[3], Thomas JB[40], Thompson GT[40], Tucker JM[38], Ustunisik G[41], Waelkens C[42], Zhang Y[43], Zhou T[45].

Affiliations:

1: CNRS, Université Clermont Auvergne, IRD, OPGC, Laboratoire Magmas et Volcans, F-63000 Clermont-Ferrand, France

2: Institut des Sciences de la Terre, Université de Lausanne, Switzerland

3: Department of Geology and Geophysics, Woods Hole Oceanographic Institution, Woods Hole, Massachusetts 02543, USA

4: Department of Earth Sciences, University of Oregon, Eugene, OR 97403-1272, United States

5: Department of Earth and Atmospheric Sciences, Cornell University, Ithaca, NY 14853, USA

6: Graduate School of Oceanography, University of Rhode Island, Narragansett, RI 02882, USA.

7: ESIA-Ticoman, Instituto Politecnico Nacional (IPN), D.F. 07340, Mexico

8: Lamont-Doherty Earth Observatory of Columbia University, Palisades, NY 10960, USA

9: Department of Geosciences, Virginia Tech, Blacksburg, Virginia 24061, U.S.A.

10: Faculty of Science, Vrije Universiteit Amsterdam, De Boelelaan 1085, 1081 HV Amsterdam, The Netherlands

11: Department of Earth Sciences, Wills Memorial Building, Queen's Road, University of Bristol, Bristol BS8 1RJ, UK.
12: Department of Geological Sciences, Brown University, Providence, RI 02912, USA.
13: Guangzhou Institute of Geochemistry, Chinese Academy of Sciences, Guangzhou 510640, China
14: Dept. Geological Sciences, New Mexico State University, Las Cruces, NM 88003, USA
15: Department of Mineral Sciences, National Museum of Natural History, Smithsonian Institution, 10th & Constitution Ave., Washington DC, 20560, USA
16: Earth Sciences and CODES, University of Tasmania, PB79, Hobart TAS 7001, Australia
17: College of Earth, Ocean, and Atmospheric Sciences, Oregon State University, Corvallis, OR 97331-5503, USA
18: Centre de Recherches Pétrographiques et Géochimiques, Université de Lorraine, CNRS UMR 7358, Nancy, France.
19: Hawaii Center for Volcanology, Department of Geology and Geophysics, University of Hawaii, Honolulu, HI 96822, USA
20: Division of Geological and Planetary Sciences, California Institute of Technology, Pasadena, California 91125, USA
21: Institut fur Mineralogie, Westfälische Wilhelms-Universität Münster, Corrensstrasse 24, 48149 Münster, Germany
22: Department of Earth and Environmental Sciences, University of Manchester, Oxford Road, Manchester, M13 9PL, UK
23: Department of Earth Sciences, Durham University, Durham DH13LE, UK
24: GeologicaI lnstitute, University of Tokyo, Tokyo 113, Japan
25: Department of Geological and Environmental Sciences, The Faculty of Natural Sciences, Ben-Gurion University of the Negev, P.O. Box 653,Beer Sheva 84105, Israel
26: Faculty of Science, Department of Geosciences, Shizuoka University, 422-8529, Japan.
27: Department of Earth Sciences, IIC 1047, Memorial University, St. John's, Newfoundland A1B 3X5, Canada
28: Department of Earth Sciences, University of Delaware, Newark, DE 19711, USA
29: Key Laboratory of Orogenic Belts and Crustal Evolution, School of Earth and Space Sciences, Peking University, Beijing 100871,China.
30: Instituto de Geofisica, UNAM, Ciudad de Mexico, 04510, Mexico
31: Department of Geology, University of Maryland, College Park, MD 20742, USA
32: Department of Earth Sciences, University of Toronto, Toronto, ON M5S 3B1, Canada
33: Goethe Universität Frankfurt, Altenhöferallee 1, 60438 Frankfurt am Main, Germany
34: College of Engineering & Natural Sciences, University of Tulsa, 800 S. Tucker Drive Tulsa, OK 74104, USA
35: Institute of Earth Sciences, The Hebrew University of Jerusalem, 91904 Jerusalem, Israel

36: School of Earth and Environment, University of Canterbury, Private Bag 4800, Christchurch 8140, New Zealand
37: Department of Geosciences, Boise State University, 83725, Boise, ID, USA
38: Department of Terrestrial Magnetism, Carnegie Institution for Science, Washington, DC 20015, USA.
39: Kochi Institute for Core Sample Research, Japan Agency for Marine-Earth Science and Technology, Nankoku 783-8502, Japan.
40: Department of Earth Sciences, Syracuse University, Syracuse, NY 13244, USA
41: Geology and Geological Engineering, South Dakota School of Mines and Technology, Rapid City, SD 57701, USA
42: Department of Earth and Planetary Sciences, McGill University, Montreal, Quebec, Canada H3A 0E8
43: Institute of Oceanology, Chinese Academy of Sciences, Beijing, China
44: Kumamoto University, Graduate School of Science and Technology, Kurokami 2-36-1, Kumamoto 860-8555, Japan
45: China University of Petroleum (East China), Qingdao, China, 266580

Abstract

Mineral-hosted melt inclusions have become an important source of information on magmatic processes. As the number of melt inclusion studies increases, so does the need to establish best practice guidelines for collecting and reporting melt inclusion data. These guidelines are intended to ensure certain quality criteria are met and to achieve consistency among published melt inclusion data in order to maximize their utility in the future. Indeed, with the improvement of analytical techniques, new processes affecting melt inclusions are identified. It is thus critical to be able to reprocess any previously published data, such that reporting the raw data is one of the first "best practices" we recommend for authors and a publication-criteria that reviewers should be sensitive to. Our guidelines start with melt inclusion selection, which is a critical first step, and then continue on to melt inclusion preparation and analysis, covering the entire field of methods applicable to melt inclusions.

Dedication

In March of 2000, a melt inclusion workshop was held at the Chateau de Sassenage in Grenoble and a companion issue of Chemical Geology entitled "Melt Inclusions at the Millennium" was published. Erik Hauri was heavily involved with the meeting and contributed two landmark papers to the topical issue of Chemical Geology on the use of secondary ion mass spectrometry to analyze volatiles in melt inclusions. When the melt inclusion community re-convened at Woods Hole Oceanographic Institution in August of 2018, we were saddened that Erik was unable to join us due to his failing health. Less than a month later came the devastating news of his passing at only 52 years of age. In recognition of his incredible contributions to science in general and to the *in situ* analysis of melt inclusions in particular, the participants and organizers of the WHOI melt inclusion workshop dedicate this collegial paper to Erik Hauri, our colleague, mentor and friend. Thank you Erik.

Introduction

Melt inclusions have long been recognized as unique petrologic indicators, starting with the classic descriptions of melt inclusions by Sorby in 1858. These small pockets of silicate, carbonate, sulfide and other types of melts entrapped within growing mineral grains have been used to study a wide range of topics, including mantle melting, pre-eruptive magmatic volatile budgets, the oxidation state of the upper mantle, the metal contents of ore-forming magmas and partitioning behavior of elements and chemical species between minerals, melts and fluids. The information recorded by melt inclusions is unique because entrapped melts are physically isolated from most interactions with the external environment and preserved for later examination. The study of melt inclusions involves careful sample selection and preparation, application of state-of-the-art analytical methods, and meticulous attention to potential artifacts related to post-entrapment processes. As the melt inclusion community has grown and access to *in situ* analytical techniques expanded, the number of publications using melt inclusion data has dramatically increased. The numbers speak for themselves: in 1990 there were about 10 publications on melt inclusions, which grew to 60–100 research papers in 2000, to

more than 300 publications in 2017–2018 (source: Science Direct, using keywords search for "melt inclusion" in the abstract or title). It is therefore important to periodically assess the state of the field. In August of 2018, a melt inclusion workshop – attended by 74 researchers from 14 countries – was convened at Woods Hole Oceanographic Institution (WHOI) with this goal in mind.

Much of the collective knowledge amassed by the melt inclusion community is passed along from one lab to another *viva voce*, making it difficult for a motivated novice to know where to start. One outcome of the WHOI melt inclusion workshop was a set of recommended practice guidelines for collecting and reporting melt inclusion data. They are appropriate for silicate melt inclusion compositions and mainly applicable to olivine host-mineral phases, but *in situ* analytical methods can be adapted to other host minerals. These guidelines are presented here as a resource for the broader melt inclusion community. An earlier paper by Cannatelli et al. (2016) highlighted guidelines to novices on how to conduct studies on silicate melt inclusions. Our work extends the discussion to the use of analytical techniques of recent application to the study of glass inclusions (e.g. 3D XRT, XANES) and provides a detailed treatment of the problems encountered in data analysis and interpretation, accompanied by a summary of the best practices to follow in the study of inclusions.

The paper is divided into two complementary sections. The first section discusses protocols for choosing appropriate melt inclusions for study, documenting their textural characteristics, assessing the extent of post-entrapment modifications, and the types of corrections that can be made to analytical data to account for those modifications, as needed. The second section describes best practices for commonly-used analytical techniques.

One objective of this paper is to provide the scientific melt inclusion community with a resource documenting how to collect and process high-quality melt inclusion data and to suggest guidelines for the type of data that should be reported and included in publications. Adherence to these guidelines will bring some uniformity to characterizing melt inclusions and reporting those characteristics, making the data much more useful for application to future studies. As you read through the text, it is instructive to remember the words used by Henry Clifton Sorby to close his 1857 address before the Geological

Society of London: *"I argue that there is no necessary connexion between the size of an object and the value of a fact, and that, though the objects I have described are minute, the conclusions to be derived from the facts are great."*

Melt inclusion selection and correcting for post-entrapment processes

1.1. Choice of melt inclusions

What is the pre-eruptive magmatic volatile budget of a volcano? What is the nature of the mantle source region for mafic magmas from different tectonic and geodynamic environments? How much water can be lost or gained by melt inclusions by post-entrapment diffusive processes? What is the cooling history of a crystal? What was the metal content of the ore-forming melt? How are elements partitioned between melts, minerals and fluids? These are examples of questions that can be addressed using data from melt inclusions.

The first step in a melt inclusion study is to identify the problem or question that is being addressed. This information is required to select the appropriate melt inclusions for study, and to identify the various steps one should follow to obtain the highest quality and most detailed information from the melt inclusions. In many, if not most samples, some or all of the melt inclusions may be crystallized to various extents, and this, in turn, determines the steps required to prepare the inclusions for analysis. Thus, rapidly quenched, glassy melt inclusions can be exposed and analyzed directly, whereas crystallized melt inclusions may require heating and homogenization before exposure. If the goal is to determine the pre-eruptive volatile content of the melt, a homogeneous (glassy) melt inclusion is required. Conversely, if one is determining the metal (Cu, Au, Zn, etc.) content of the melt associated with ore formation, crystallized MI can be analyzed as is using LA-ICP-MS to determine the metal content.

The nature of the melt inclusions in any given sample is a function of the history of trapping and later evolution of the host rock, and can produce MI that range from being totally homogenous and glassy to those that are completely crystallized. Student and

Bodnar (1999), for example, discuss the various processes that determine the phase state of MI "as found". Both types of melt inclusions (glassy and crystallized; photos. Fig. 1A and C, respectively) are potentially useful, depending on the question or problem being addressed, and glassy melt inclusions are not always "better" than crystallized melt inclusions.

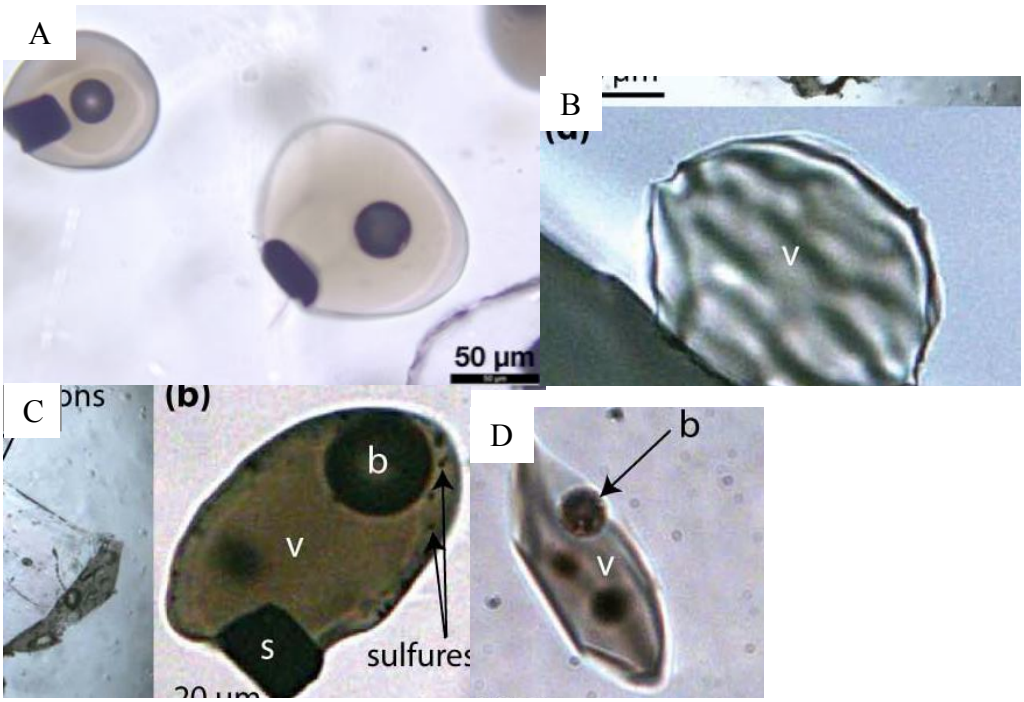

Fig. 1: (A) picture of two glassy olivine-hosted melt inclusions from the Ambae volcano. Inside both inclusions, we can see the very circular bubble and the squarish spinel. (B) Sometimes the adopt the faceted crystal shape of the host mineral giving the inclusion this "raisin" aspect. (C) BSE image of a crystallized inclusions with dendritic microcrystals (m), several small bubbles (b) and a glassy matrix, (D) picture in transmitted light of a devitrified melt inclusion from Pan de Azucar volcano (pictures B, C and D from Le Voyer, PhD 2009).

Thus, glassy melt inclusions with no bubble are not necessarily less affected by post-entrapment crystallization compared to crystallized melt inclusions. It may just be less obvious, and one may still need to correct for the compositional effects of post-entrapment modifications. There is not one single procedure that is applicable to all melt inclusions, and all questions being addressed. Rather a variety of approaches can and should be applied, depending on the nature of the melt inclusions and the question you want to address.

Because melt inclusions often experience post-entrapment modifications, it is critical to assess whether the MI to be studied have recorded and preserved the original conditions at trapping, and this can be addressed through the study of melt inclusion assemblages (MIA). The concept of MIA is based solely on petrographic observations and echoes the definition for fluid inclusion assemblages that is, groups of melt inclusions that were all trapped at the same time (e.g. Bodnar and Student, 2006; Cannatelli et al. 2016). A MIA is often identified as a group of melt inclusions that occur within a three-dimensional grouping within a phenocryst, or are distributed along either growth surfaces or healed fractures. Excellent examples of MIAs are shown in Bodnar and Student, 2006, Figs. 1-5 and 1-15; Esposito et al., 2013, Figs. 3 and 4). Tools such as cathodoluminescence (CL) zoning in quartz (Peppard et al., 2001) or phosphorous (P) zoning in olivine obtain by electron probe or nanoSIMS (e.g. Milman-Barris et al., 2008; Welsch et al., 2014; Shea et al., 2019; Manzini et al., 2017b) can be combined with petrographic observations to help identify MIAs. Melt inclusions are usually best investigated in polished thin or thick sections. Similar chemical composition of all of the melt inclusions in an assemblage indicates that the melt inclusions all trapped a single homogeneous phase (melt) that has not been modified after trapping, or, that all of the melt inclusions in the MIA experienced the same extent of modification (which is highly unlikely).

Melt inclusion size and position inside the grain are also of importance and should be reported in melt inclusion studies (see Table 1 for templates). For olivine-hosted melt inclusions, for example, the size of the inclusion, the size of a vapor bubble and secondary mineral inclusions (if present), and the distance shortest to the rim of the crystal must be documented and reported in the supplementary material (Table 1). As an example of why this is important, larger inclusions located in the interiors of large olivine host-crystals are less susceptible to H diffusive loss (e.g. Qin et al., 1992; Chen et al., 2011; Gaetani et al., 2012), therefore their H_2O contents are more likely to represent the pre-eruptive H_2O content. Another important consideration is that the lack of correlation between bubble size and melt inclusion size in MIAs may indicate heterogeneous entrapment of vapor in some of the melt inclusions (Steele-MacInnis et al., 2017).

1.2. Textural features, imaging of melt inclusions and orientation of the crystal

Melt inclusion textures (shapes, sizes, and distributions within crystals) are often overlooked in favor of compositional data, yet they can hold information on magmatic processes, conditions, and timescales. For example, several studies have noted that melt inclusion morphologies vary from irregularly-shaped to ellipsoidal to faceted (negative crystal shape giving the inclusion a "raisin-like" aspect; Fig. 1B; e.g., Chaigneau et al. 1980, Beddoe-Stephens et al. 1988, Manley 1996, Anderson et al. 2000, Gualda et al. 2012) and a geospeedometer based on faceting of quartz-hosted melt inclusions was recently proposed, which can be used to assess quartz crystallization timescales and growth rates (Gualda et al. 2012, Pamukcu et al. 2013, 2015). Combining such information from melt inclusion textures with melt inclusion and/or host crystal compositions can be an especially powerful approach to understanding magmatic systems.

Given the small size and three-dimensional (3D) nature of melt inclusions, high-resolution 3D methods are necessary for accurate quantification of their sizes and shapes (Richard et al., 2018). The spatial distribution and context of melt inclusions within crystals also has implications for interpreting 2D images and compositional data (Créon et al., 2018). In particular, an unexposed melt inclusion hidden below the crystal surface may affect CL intensities and backscattered electron signals, as well as compositional analyses from electron and scanning electron microprobes, depending on the excitation volume for a given set of beam conditions.

Traditionally, optical microscopy has been the primary method for describing and documenting melt inclusion textures. Today, increased accessibility of 3D X-ray tomography (XRT) and the development of new methods for imaging materials with XRT allows for rapid (minutes to hours), non-destructive, high-resolution (≤ 1 μm/voxel) 3D imaging of crystals and their melt inclusions (Richard et al., 2018). This has significantly increased the accuracy and precision of quantitative measurements of melt inclusion textures; however, the approach is not without its shortcomings, and the

following points should be considered when deciding to use 3D XRT for studies of melt inclusion in crystals:

Low density contrast between melt inclusion and crystal host (e.g., rhyolitic melt inclusions in quartz) precludes the use of standard XRT approaches and grayscale filtering for image processing. In these circumstances, propagation phase-contrast XRT can instead be used to enhance object edges, and edge-detection algorithms can be used for image processing (see Pamukcu et al., 2013). However, this approach is most effective on synchrotron-based XRT systems, where the sample-to-detector distance can be changed significantly.

Imaging with synchrotron-based XRT has the advantage that analyses are relatively quick (~15–30 minutes) and the systems typically do not have user fees (except in cases of proprietary research). However, users generally have to submit research proposals, and obtaining time on these systems can be competitive. Consequently, access and data collection are limited by proposal acceptance, time allotted, and – in some cases – cost. In addition, for these setups, crystals are typically imaged individually (depending on their size). In comparison, access and costs for desktop XRT systems are lab-specific, and analyses can take much longer (up to 12+ hours), although multiple crystals can often be scanned at once.

Substantial time may be required for image processing (up to hours for individual melt inclusions). Large datasets (up to tens of GB) may require significant computing resources (i.e., large number of CPU cores and memory). Future developments in image processing methods could substantially reduce the time and computing power required for this step.

Precise imaging of crystals is also essential for one that strive to capture parental water contents in melt inclusion. Any elemental diffusion work requires careful crystal orientation and good practices are exposed in detailed in Shea et al., 2015. With H diffusion being so anisotropic, it is important that melt inclusions should be sectioned with awareness, ideally in oriented crystals. The diffusivities are much faster (Ferriss et al., 2018; Barth et al., 2019) than those inferred in bulk from the dehydration-hydration experiments on unoriented olivines that contain melt inclusions (e.g. Portnyagin et al., 2008; Gaetani et al., 2012, 2014; Chen et al., 2011, 2013). Recently published

experimental results provide a new bulk D for the highly anisotopic diffusion that can lead to large errors in interpretation, specifically for olivine-hosted melt inclusions with a nearby rim along the a-axis (Barth et al., 2019).

Best practices:

The first step in a melt inclusion study is to conduct a detailed petrographic study to determine the range in sizes, shapes, textures and distribution of MI within host phenocrysts. This information is critical to selecting MI that are related to the geologic question or problem being addressed, and to identify MI that may have been modified following trapping. Conventional petrographic examination of the MI may be sufficient in many cases, or may be supplemented by cathodoluminescence (CL) of MI in quartz (e.g., Peppard et al., 2001), major and minor element mapping by electron microprobe, phosphorous zoning in olivine (e.g., Welsch et al., 2014), or 3D propagation phase-contrast XRT, to better constrain the physical characteristics of the MI and their relationship to host-crystal growth. Subsequent analyses of these crystals and melt inclusions, and interpretation of results, should take melt inclusion textures into account. While precise textural analysis requires a lot of effort, the extent of detailed imaging is also dependent on the question being addressed, so microscope imaging might be sufficient. We recommend reporting imaging conditions, image resolution, and any image processing approaches used on 3D datasets. During image processing, be careful not to overwrite the original data.

1.3. Homogenization and chemical composition reconstruction

1.3.1. Homogenization

Homogenization experiments can be performed in three ways: in a microscope heating stage (e.g. Sobolev et al., 1980), in a 1-atm furnace (e.g. Sinton et al.,1993, for plagioclase), and heating the melt inclusions in an autoclave under pressure. The first two procedures were compared using quartz-hosted inclusions and have been extensively discussed elsewhere (Student and Bodnar, 1999). They concluded that the temperature of homogenization is independent of inclusion size when the procedure is performed in a 1-atm furnace with a small temperature increment (10 ºC per minute), and the temperature of homogenization corresponded to the known temperature of formation. In contrast, in a

microscope heating stage, the temperature of homogenization is higher than the formation temperature and a positive correlation exists between the size of the quartz-hosted melt inclusions and the heating rates. Their advice for quartz-hosted melt inclusions was to use the data of the smallest melt inclusions that were homogenized with slow heating rates (<1 ºC/min). However, in the case of olivine-hosted melt inclusions, we explain below that one will need to check for diffusive loss of H_2O from the melt inclusions through the olivine after homogenization, since small melt inclusions are prone to losing H^+ faster than bigger ones (e.g. Gaetani et al., 2012).

For crystallized olivine-hosted melt inclusions, homogenization experiments consist of heating experiments to melt the crystals, followed by rapid cooling to quench the melt to glass (fundamentals of the method are described in Roedder, 1979, 1984). While the goal of heating experiments is usually not to determine the entrapment temperature, the entrapment temperature can be determined if the melt inclusions are re-heated under a confining pressure that is equivalent to the trapping pressure (see discussion in Student and Bodnar, 2004; Cannatelli et al., 2016). The purpose of a heating experiment is to homogenize the contents to produce a single homogeneous melt (glass) upon quenching that can be later analyzed. Temperatures of homogenization (T_h) of melt inclusions systematically increase with time during heating experiments, regardless of their major element composition and their H_2O content, likely due to deformation of the inclusion in response to the pressure gradient between the inclusion and the exterior of the host olivine (e.g. Sobolev and Danyushevsky, 1994; Massare et al., 2002; Tison, 2006; Schiavi et al, 2016). Visual inspection during heating of the melt inclusion is essential, meaning the use of a Vernadsky-type stage (designed by Sobolev et al., 1980) or equivalent is the best approach. Care must be taken to assess the extent to which the heating procedure may have affected volatile concentrations, especially H_2O, in the melt inclusions. For example, diffusive exchange is temperature-dependent and some studies have shown that complete diffusive exchange of H_2O between a melt inclusion and the external melt through a 1-mm-diameter host olivine happens within 2 days at 1250 ºC (Gaetani et al. 2012), while even after 2 days complete equilibrium will not be attained at 1140 ºC (Portnyagin et al. 2008) and not at all at 1100 ºC (Bucholz et al., 2013). Careful homogenization procedures are required to minimize H_2O loss (e.g. Chen et al., 2011;

<10 min above 1200 ºC for a 20-µm-radius melt inclusion in a 300-µm-diameter olivine will not produce significant H_2O loss). H_2O loss during homogenization is much less of a problem in quartz; Severs et al. (2007) documented insignificant H_2O loss after 12 hours of heating at the inferred trapping temperature of 800 °C at a confining pressure of 1 kbar.

It is now established that one conclusive test for proton diffusion during homogenization is to confirm that there is no negative correlation between H_2O content and the D/H isotope ratio. Gaetani et al. (2012) and Bucholz et al. (2013) assess the consequence of diffusive re-equilibration using the MATLAB script given in Bucholz Appendix B. Other volatile elements like Cl and F are not affected by diffusive re-equilibration during homogenization (Bucholz et al., 2013), but it is not clear yet if S is sensitive to diffusion through the olivine host.

Another post-entrapment effect that can be investigated using homogenization experiments is the transfer of low-solubility CO_2 to a bubble. Homogenization experiments in a heating stage (Wallace et al., 2015), a 1-atm furnace (Tuohy et al., 2016), and an internally heated pressure vessel (Mironov et al., 2015) have all been successful in redissolving CO_2 in bubbles back into the melt (see also Moore et al., 2018). Loss of CO_2 to vapor bubbles is discussed in more detail below.

While melt inclusion CO_2-H_2O concentration data (with bubble and with no CO_2 bubble restoration) provide a "vapor saturation pressure", such pressures do not necessarily convert directly into entrapment depth. Vapor saturation pressures yield a minimum entrapment depth (≈ minimum pressure of crystallization; e.g. Anderson et al., 1989) unless it can be shown that the melts were vapor saturated at the time of trapping. However, in the absence of independent evidence that the melts were volatile saturated at the time of trapping, such as the presence of melt and fluid inclusions that were trapped simultaneously, there is no basis for concluding that melt inclusions were vapor saturated during entrapment, and thus pressures determined from the MI will be minimum entrapment pressures. Additionally, because rapid H diffusion through olivine can re-equilibrate melt inclusions following entrapment, CO_2-H_2O vapor saturation pressures may have been further modified to reflect the external melt H_2O content during the final

storage conditions prior to rapid ascent and eruption, rather than initial entrapment conditions.

While the solubilities of all common volatile components in silicate melts vary with pressure, CO_2 solubility is especially sensitive to pressure. When melts are trapped inside growing crystals, the melt could have already degassed/exsolved some fraction of its initial CO_2 and therefore not reflect the CO_2 concentration of the original magma at its source region. In this case, the CO_2 concentration reflects that of the melt at the pressure of trapping. Alternatively, the CO_2 content could be well below the saturation value so that, even though the solubility is pressure-dependent, the melt may not have reached volatile saturation before being trapped at some lower pressure.

Best practice:

Fundamental historical references for homogenization exist describing in detail the method and the pitfalls of the procedure (Roedder, 1979, 1984; Student and Bodnar, 1999; and review by Lowenstern 1995) and for the heating mechanism used (e.g. Schiano, 2003; Chen et al., 2011). If possible, visual inspection during homogenization of inclusions is best and ideally you should test your heating procedure on a few melt inclusions to determine the homogenization temperature of the MI before heating the rest of your samples.

Diffusive H_2O loss can occur during magma ascent in nature and during heating in the laboratory. The best evidence that MI have experienced loss of H_2O (or other volatiles) is if the MI within a melt inclusion assemblage show variable concentrations, as any type of modification, including H_2O loss, depends on inclusion size, shape, location within a crystal, and other factors. Diffusive H_2O loss may be identified through a negative correlation between H_2O and D/H. If you do not have access to a SIMS for D/H measurements, then looking for a relationship between melt inclusion size and H_2O content should be investigated. A positive correlation between melt inclusion diameters and H_2O concentrations is a sign that diffusive loss of hydrogen has occurred. If diffusive loss occurred during ascent, the largest, most H_2O-rich inclusions provide the best estimate for pre-eruptive H_2O concentration in the melt.

1.3.2. Compositional corrections

A melt inclusion will record the composition of the trapped melt if the MI remains a chemically and physically isolated system following entrapment. Following entrapment, however, a melt inclusion may experience modifications in response to changing P-T-X-fO_2 conditions in the magma, post-entrapment crystallization (PEC) of the host mineral, thermoelastic deformation, plastic deformation and chemical exchange resulting from diffusive re-equilibration with host olivine (and other minerals) and even the external magma (e.g., Watson, 1976; Qin et al., 1992; Tait, 1992; Zhang, 1998; Sobolev and Danyushevsky, 1994; Sobolev and Chaussidon, 1996; Danyushevsky et al., 2000; Gaetani and Watson, 2000; Danyushesky et al., 2002a; Portnyagin et al., 2008; Gaetani et al., 2012; Chen et al., 2013). These modifications must be identified to correct for their effects to reconstruct the original melt inclusion compositions. However, not all processes are reversible and therefore one may not always be able to correct for their effects. The plastic deformation (e.g. Zhang, 1998) is an irreversible process. Hereafter we discuss the PEC corrections for olivine-hosted melt inclusions.

<u>For major elements</u>

In the case of olivine-hosted melt inclusions where olivine is the only crystallizing phase, the Fe-Mg contents of the trapped melt can be determined based on the equilibrium distribution coefficient Kd relating the partitioning of Fe and Mg between olivine and melt (Roeder and Emslie, 1970). This correction is described in detail in the following paragraph and affects mainly MgO, FeO_T and SiO_2. All other elements (major, minor, volatile and incompatible elements) are affected to the same degree because they do not enter into the host phase and thus their concentrations are all diluted by the PEC-correction. Between formation at depth and eruption at the surface, an olivine-hosted melt inclusion may undergo crystallization in response to, for example, cooling or diffusive H_2O loss. A layer of olivine crystallizing along the melt inclusion wall will modify the major element composition of the residual melt, particularly affecting Fe and Mg contents. This PEC can be corrected for numerically (e.g. Danyushevsky et al., 2002b). This involves adding small increments of equilibrium olivine back into the measured melt inclusion composition until the Fe-Mg partition coefficient Kd reaches the equilibrium value. The equilibrium value for the Mg-Fe exchange coefficient between olivine and

liquid, Kd, is known to depend on T, P, H_2O, and alkali content (e.g. Ford et al., 1983; Sack et al. 1987; Toplis, 2005). As an accurate knowledge of Kd is required for PEC correction, we recommend using a Kd model accounting for as many of these parameters as possible (e.g. Toplis, 2005, where T and P are inputs to the model and you calculate an "expected Kd"). In addition, because the concentration of Fe^{2+} depends on the oxygen fugacity, the Fe^{3+}/Fe_{tot} ratio is needed for the PEC calculation and has to be assessed (e.g. Kress and Carmichael, 1991).

We acknowledge there are several ways of correcting for this PEC, but the general procedure is to calculate the $Kd=(Fe/Mg)_{olivine}/(Fe/Mg)_{melt}$ of a melt inclusion and recalculate this Kd after each increment of olivine addition. The value of $(Fe/Mg)_{olivine}$ should come from analysis of the olivine directly adjacent to the melt inclusion, so it is important to check for olivine zoning (e.g. Ruscitto et al., 2010) and when possible, to analyze along two orthogonal Fe-Mg profiles radially to the inclusion. The process of olivine addition stops when calculated Kd = "expected Kd". The mean mass of olivine added can therefore be calculated and PEC correction applied. PEC is highly variable, from a few percent to more than 20% (e.g. Rasmussen et al., 2017). Throughout the years, softwares have been developed to perform this PEC correction, such as the Petrolog3 software (Danyushevsky and Plechov, 2011). It is important to recognize that Petrolog3 is a tool that incorporates many different model choices, meaning that simply stating a PEC correction was carried out using Petrolog3 is too vague. It is advisable to report which models were used for mineral-melt equilibrium, the $Fe^{3+}/\Sigma Fe$ of the melt, FeO_T etc. as implemented in Petrolog3.

A corollary to this recommendation is that the raw data, not normalized to 100 wt. % should be reported in the supplementary material of every melt inclusion study.

Some post-entrapment processes are more challenging to correct. For example, the chemical composition of an olivine-hosted melt inclusion is susceptible to Fe-Mg exchange reaction via Fe-Mg olivine/ melt equilibrium and interdiffusion in olivine (Gaetani and Watson, 2000; Danyushevsky et al. 2000). This process can be assessed by analyzing the host olivine to look for broad compositional gradients adjacent to the melt inclusion (e.g., Fig. 5 of Gaetani and Watson, 2000) or by comparing the FeO_T contents of associated lavas with the FeO_T of the melt inclusions as a function of MgO (e.g.,

Danyushevsky et al., 2000). Danyshevsky et al. (2000) proposed a correction scheme to deal with this diffusive exchange that can be implemented in Petrolog3.

One alternative to correcting for PEC and diffusive Fe-Mg exchange is to compare melt inclusion compositions using pseudo-ternary projection schemes (O'Hara, 1968; Walker et al., 1979). In this case, inclusion compositions are recalculated into mineral components (typically olivine, plagioclase, clinopyroxene, and quartz). Projecting the recalculated inclusions from the olivine apex eliminates the effects of PEC, and combining Fe and Mg on a molar basis eliminates the influence of Fe-Mg exchange.

For melt inclusions hosted in quartz, PEC correction would imply adding SiO_2 but criteria for knowing when to stop are to be identified. Theoretically, reverse crystallization calculations for plagioclase and clinopyroxene are available using Petrolog3 and PEC correction could be possible, but so far no literature data describes this.

<u>For H_2O and CO_2: post-entrapment bubble formation</u>

Following trapping, some portion of the volatile components in the melt may exsolve to form a separate phase (e.g. Roedder, 1979; Anderson and Brown, 1993; Kamenetsky & Kamenetsky, 2010; Moore et al. 2015). It is very common for olivine-hosted melt inclusions to have a single, CO_2-rich vapor bubble. The post-entrapment decrease of pressure in inclusions that leads to bubble formation has two main causes: crystallization of olivine along the inclusion-host interface, and the greater thermal expansion of melt compared to olivine, which causes the melt to contract more than the host phase (cavity) during cooling (Roedder, 1979; Anderson and Brown, 1993). Other factors contributing to bubble formation include melt density changes during post-entrapment crystallization, diffusive loss of H from inclusions, and elastic deformation of the host mineral during pressure changes. The magnitude of the two main factors (crystallization and differential shrinkage of the included melt and host) are such that it is common for a bubble to occupy about 1 to 5 volume percent of the inclusion, and it is important to note that much of the total volume expansion takes place rapidly during eruption and quenching as the included melt cools to its glass transition temperature (Riker, 2005; Moore et al., 2015). The presence of MIAs that all contain the same proportions of melt and vapor provides

strong evidence that bubbles formed after trapping (Roedder, 1984). In this case, it is reasonable to conclude that the composition of the melt that was trapped is represented by the bulk composition of the inclusion (glass + bubble).

In general, determining the bulk volatile concentration of melt inclusions in which some portion of the volatile components have fractionated into a separate vapor phase requires the same approach that would be used to account for the presence of daughter crystals or post-entrapment crystallization: experimental reheating, *in situ* microanalysis and mass balance calculations, and/or numerical modeling (Moore et al., 2015; Aster et al., 2016; Tuohy et al., 2016; Esposito et al., 2016). The approach of experimental reheating involves re-dissolving the vapor bubble back into the melt and then quenching so that the glass can be directly analyzed for CO_2 (Mironov et al., 2015; Wallace et al., 2015). For the mass balance approach (e.g., Esposito et al., 2008; 2011; Hartley et al., 2014; Moore et al., 2015), it is necessary to determine the dissolved volatile concentrations in the glass, the room temperature density of CO_2 in the bubble, and the relative proportions of the glass and the bubble. The density of CO_2 in the bubble can be determined using Raman spectroscopy (e.g., Moore et al., 2015 and described in section 2.1.1.), and the volume proportion occupied by the bubble can be determined petrographically or by using X-ray tomography (e.g. Richard et al., 2018). The numerical approach involves modeling of bubble formation and CO_2 exsolution as a function of PEC (Anderson & Brown, 1993; Steele-MacInnis et al., 2011; Wallace et al., 2015; Aster et al., 2016). Moore et al. (2018) discuss some of the relative strengths and weaknesses of different techniques applied to primitive olivine-hosted melt inclusions that contain CO_2-rich bubbles. Applying multiple methods whenever possible and looking for consistency between the different results provides confidence that the initial CO_2 concentrations of melt inclusions thus determined is correct.

In some cases, the accuracy of the mass balance calculation used to determine total CO_2 could be influenced by the presence of solid phases such as carbonate crystals or native S on the wall of the bubble (e.g. Esposito et al., 2016). However, the amount of CO_2 sequestered in carbonates may not be significant in most cases. When melt inclusions are heated long enough to destabilize most or all of the carbonate, the total CO_2 is in the range of melt inclusion containing carbonate (Pamukcu and Gaetani, unpublished data).

A number of studies have employed the Ideal Gas Law or some other equation of state to calculate the density of the vapor within bubbles and then used their observed volume to calculate the mass of CO_2 (e.g. Shaw et al., 2008, 2010). This method, however, does not account for (disequilibrium) expansion of the bubble during quenching, and systematically overestimates the CO_2 content of bubbles compared to *in situ* Raman analysis (Moore et al., 2015).

Finally, some host mineral grains may contain MIAs that include melt inclusions with a range of bubble sizes (Hartley et al., 2014; Moore et al., 2015) approaching 100 volume percent of the inclusion (Roedder et al., 1963; i.e., CO_2-rich fluid inclusions with a volumetrically minor glassy rim). While this occurrence provides strong evidence that the melts were volatile-saturated at the time of trapping, these larger melt inclusion bubbles, if not associated with decrepitation of the melt inclusion, likely represent heterogeneously entrapped inclusions (e.g., Steele-MacInnis et al. 2017). In this case, the bulk composition of the inclusions would overestimate the dissolved CO_2 concentration of the melt at the time of entrapment. However, as described by Steele-MacInnis et al. (2017), the presence of this co-trapped fluid may better preserve the CO_2 concentration of the glass since the pressure drop due to PEC will be less.

<u>For trace elements</u>

Similar to major elements that are compatible in the host mineral, compatible trace element abundances will be affected by PEC of melt inclusions. Models for the evolution of trace element concentrations during PEC highlight that the type of process considered for PEC (i.e., equilibrium versus fractional) has a major influence on the post-entrapment (PE) contents of melt inclusions (Figure 2 a-f).

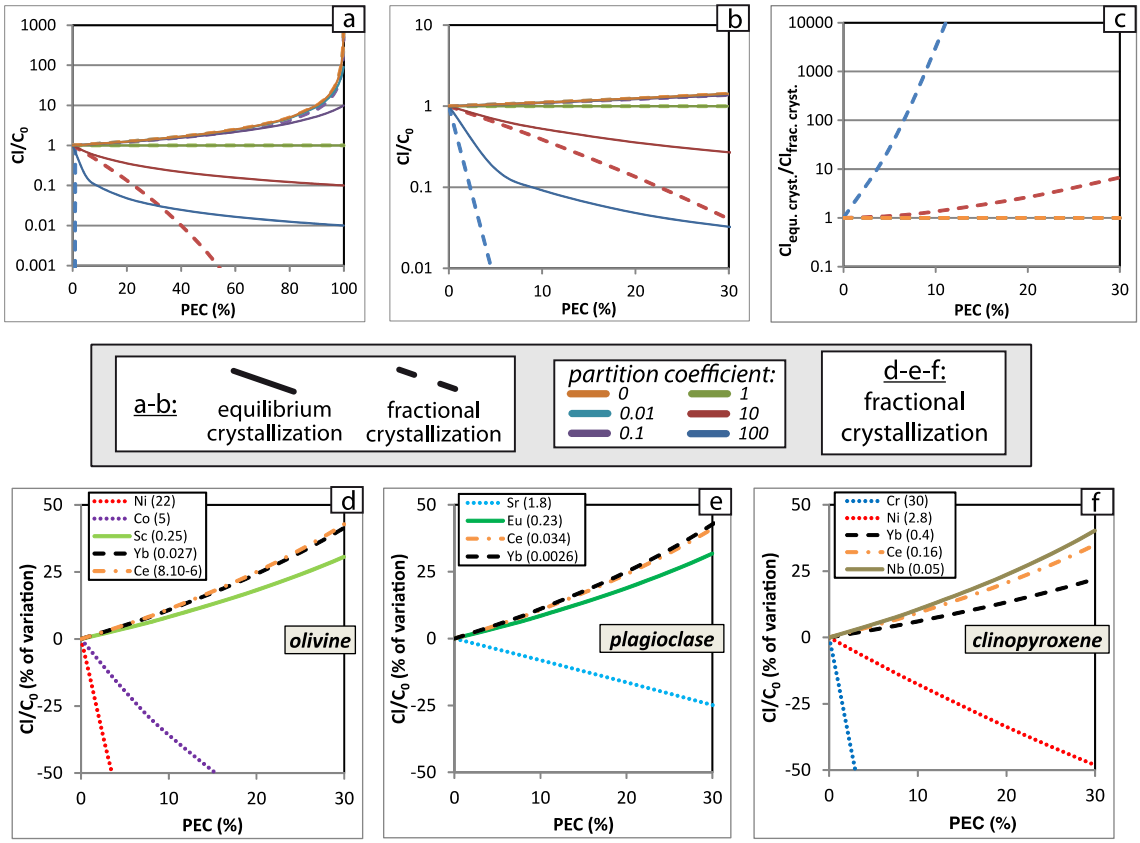

Fig. 2: Evolution of trace elements contents during PEC. a-b) present the evolution of the melt inclusion content (Cl) relative to initial content (C_0) for elements with various partition coefficients. In c-e) the variation is presented in percent of variation relative to C_0. In a-b) both equilibration crystallization (solid lines), and fractional crystallization (dashed lines) models are presented for theoretical elements with various partition coefficients (from D= 0 to D=100). In c-e) an equilibrium crystallization model is used, and specific elements are considered for PEC of melt inclusions in olivine (c), plagioclase (d), and clinopyroxene (e). Considered partition coefficients are presented between brackets for each element, and are from Laubier et al. (2014) for all elements except Ce in olivine from Sun and Liang (2013), and Cr in clinopyroxene from Bacon and Druitt (1988). Eu partition coefficient value is for redox conditions buffered with NNO.

Compatible elements are depleted in the melt as soon as crystallization begins, this depletion being extreme when considering a fractional crystallization model (Figure 1a-b). Incompatible element contents are significantly affected only after extensive crystallization (e.g., the concentration of a perfectly incompatible element only increases by a factor of 1.4 - thus by 40% - after 30% of crystallization; Figure 2b), and only varies marginally depending on the considered crystallization model in the first ~50% of

crystallization (Fig. 2a). The choice of the crystallization model to consider (equilibrium or fractional; Fig 2c) should therefore be clarified if we are to quantify post-entrapment variation of compatible elements. Although fractional crystallization can (and does) occur during PEC, the evidence for this is the existence of compositional gradients adjacent to inclusions. These are not produced by equilibrium crystallization. During equilibrium crystallization, the melt would remain in equilibrium with the host and PEC would be impossible to identify. Therefore, for the correction of the compatible element composition (for example Ni in olivine Fig. 2d, Sr in plagioclase Fig. 2e), we advise that fractional crystallization equations should be used.

Accordingly, the evolution of key compatible and incompatible elements during PE evolution of melt inclusions hosted in olivine, plagioclase, and clinopyroxene are presented in Fig. 2d-f, and highlight that PEC corrections should be applied when considering compatible element contents.

For incompatible and compatible trace elements, the reliability of the melt inclusion to represent the composition of the trapped mantle melt depends on the diffusion transport of these elements through their host crystal during magma ascent, eruption and cooling (e.g., Gaetani and Watson, 2000). The effect of PEC on both compatible and incompatible elements is a common process happening on potentially short timescales. For PEC of only a few percent, the effects on incompatible elements will be small. Diffusive reequilibration with external melt will require much longer timescales and is only a factor for compatible elements. Experiments on REE diffusion in natural olivine (Cherniak et al., 2010) have shown that melt inclusions trapped in olivine (50 µm and 1 mm radii, respectively) will preserve their REE composition for a few decades to tens of thousands of years, which encompasses the duration of melt inclusion residence and transport through the crust. Faster REE diffusion are also described (Spandler et al., 2007), which are possibly due to “fast path” diffusion along dislocation cores. As a community we do not particularly see the kind of fast diffusion they advocate in natural systems, although we acknowledge that such a process might exist. Incompatible element variations are more restricted but, regardless of the extent of PEC, we recommend PEC corrections for incompatible elements (as well as for major and compatible elements).

Best practice:

For PEC correction of major element compositions, the methods used and values for key parameters such as olivine-melt Kd must be documented. Raw data (without any compositional corrections) should be reported, not normalized to 100 wt% (we provide a template of a table as an example; Table 1). It is important to document sizes of melt inclusions and vapor bubbles and to check for coherent bubble volume proportions within MIAs. The precise determination of the melt inclusion and bubble volume is crucial for using the Raman spectroscopic method and mass balance approach for adding back the CO_2 in the bubble to the melt.

Melt inclusion analysis

We hereafter summarize the different analyses you can perform on a melt inclusion, progressing from non-destructive to increasingly destructive methods (Fig. 3). They are reported as a function of their destructive impact on the integrity of the melt inclusion and should they all be needed, they should be performed in the order described. The durations of sample preparation and measuring times of each analytical technique are highly variable, reflecting the complexity, pitfalls, and/or availability of certain instruments.

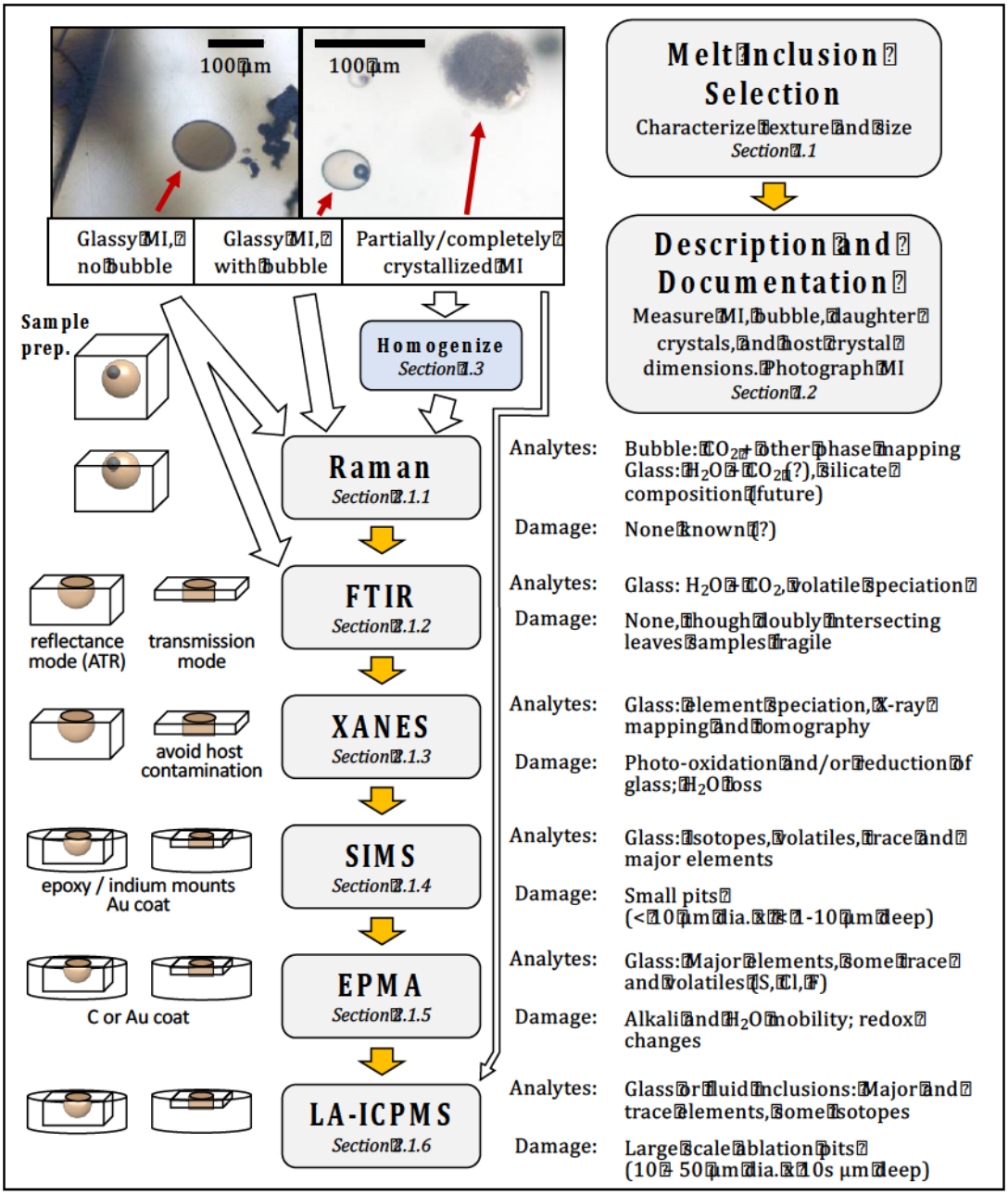

Fig. 3: Idealized flow-chart for melt inclusion (MI) sample analyses given sample preparation and analysis-induced damage considerations. Depending on the intended research, particular steps may be skipped. Samples can be re-polished to remove upper surfaces that were damaged by various techniques (EPMA, SIMS, LA-ICPMS). See text for references and for more details on preparation and best practices for MI sample selection, MI homogenization, each for analytical technique. Melt inclusions in inset photos are from Kīlauea Volcano's 2018 Lower East Rift Zone eruption.

2.1. In situ analysis

2.1.1. Raman spectrometry

Raman spectrometry is a non-destructive analytical technique that has been applied to both fluid and melt inclusions for well over 50 years. Indeed, motivation for development of the Raman spectrometric technique was driven in part by the need for an analytical method that could be applied to the tiny fluid and melt inclusions contained in natural samples (Delhaye and Dhamelincourt, 1975; Rosasco and Roedder, 1975; Dhamelincourt et al., 1979; Rosasco et al., 1979). Modern Raman systems allow for the rapid analysis of any form of matter (solid, liquid or vapor) that contains covalent bonds, and is Raman active, with approximately 1μm spatial resolution. The time required to complete a single analysis varies greatly as a function of the scattering efficiency of the species being analyzed, the concentration of the species in the analytical volume, background noise from the sample, including fluorescence, and interference from other species that show Raman bands that overlap with those of the species of interest. For more details on the Raman technique in general, and its application to fluid and melt inclusions, the reader is referred to Burke (2001), Frezzotti et al. (2012), Thomas and Davidson (2012). Raman spectrometry has been applied to melt inclusions in three general areas: (1) to determine the volatile contents of silicate (and other) glass phases contained in melt inclusions; (2) to identify and quantitatively analyze the volatile species contained in vapor bubbles in melt inclusions; (3) to identify solid phases contained in melt inclusions that have undergone partial to total crystallization following trapping. The Raman technique can be applied to melt inclusions that are exposed at the sample surface as well as to those that are beneath the surface and totally enclosed by the host crystal – this allows the mutual spatial relationships between the different phases to be preserved for multi-phase melt inclusions. The glass phase in melt inclusions is analyzed by focusing the laser beam at the surface or slightly below the surface. Spectra are generally obtained in two ranges, the 150–2000 cm^{-1} range (to cover aluminosilicate framework vibration) and 3000–4000 cm^{-1} range (to cover OH-stretching) relative to the exciting laser light (Fig. 4).

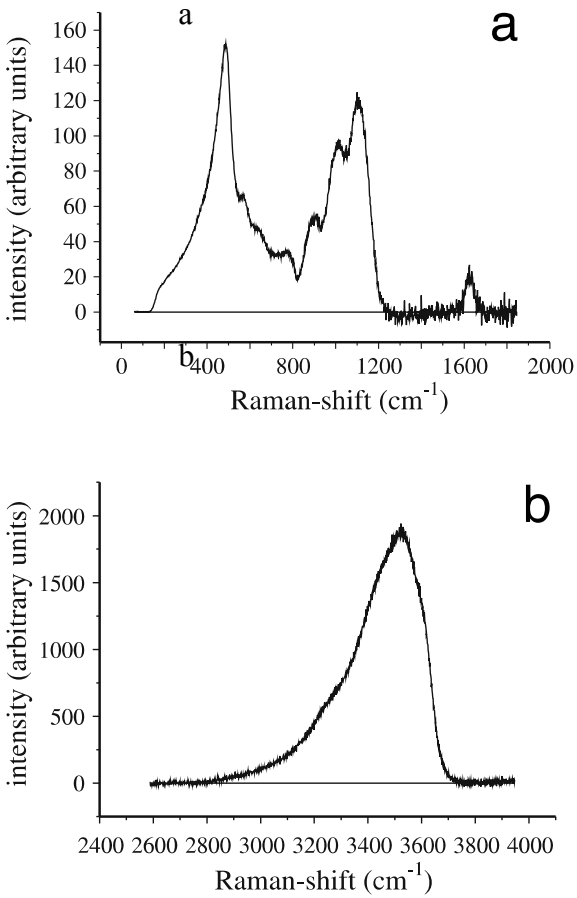

Fig. 4: Raman spectra after frequency-temperature correction (a) of the aluminosilicate framework vibration range and (b) of the OH-stretching range ("water band").

Determining the H_2O and CO_2 concentrations of melt inclusion glass by Raman spectroscopy (McMillan, 1984) has become common in melt inclusion studies (e.g. Thomas, 2000, 2006; Chabiron et al., 2004; Zajacz et al., 2005; Mercier et al., 2010; Morizet et al.; 2013; Créon et al., 2018). Thomas (2000) proposed a simple technique to determine the H_2O content of melt inclusion glass by comparing the intensity of the Raman H_2O band with that obtained from a glass standard with known H_2O content collected at identical analytical conditions. Zajacz et al. (2005) described a method that corrected the intensities of the Raman band for H_2O to account for differences in the glass composition that affect intensity, thus eliminating the effect of glass composition on the estimated water content. Severs et al. (2007) applied Raman analysis to determine the H_2O content of rhyolitic-composition melt inclusion, and used a UV (244 nm) laser to eliminate fluorescence background that is commonly associated with analyses using a

green (514 or 532 nm) laser. In some cases, Raman is the only method (other than, perhaps, nano-SIMS) to analyze the very small (~5 μm) "nano-granite" melt inclusions that occur in anatectic samples formed in the deep crust (Bartoli et al., 2013). Compared to H_2O, researchers have had less success in determining the CO_2 concentration in glass by Raman analysis, mostly because the CO_2 bands overlap with many of the bands produced by the silicate species in the glass, and because carbon occurs in more than one structural state in the melt (glass) (Mysen and Virgo, 1980; Morizet et al., 2013). In spite of these complications, Morizet et al. (2013) developed a method to quantify the CO_2 content of the glass using area under the carbonate ν_1 peak(s) and the area ratio for the aluminosilicate peaks in the range 700–1200 cm^{-1}. The authors report that the calibration is valid from 0.2 to 16 wt.% CO_2 with an analytical precision of ±0.4 wt.% CO_2. The ideal melt inclusion to study is one that contains only a homogeneous glass (melt) phase at ambient surface conditions. In some cases, especially for melt inclusions contained in lavas or in plutonic rocks, the melt inclusions may have undergone complete crystallization during cooling. Such melt inclusions are often difficult to identify and analyze, and are often overlooked during normal petrography (Yang & Bodnar, 1994; Thomas et al. 2002; 2003; Bodnar & Student, 2006). In most cases, the crystals in the melt inclusions are fine-grained and intergrown with other crystals, making their identification using petrography or SEM difficult if not impossible. Occasionally, however, such phases are large enough to be analyzed by Raman in order to identify the minerals. Thus, Student and Bodnar (2004) were able to identify the presence of feldspar in crystallized melt inclusions from the Red Mountain, Arizona, porphyry copper deposit using Raman spectroscopy. Similarly, Mernagh et al. (2011) were able to identify alkali-Ca carbonates, with varying proportions of cations, and Na-Ca-Ba sulphates (without any evidence of H_2O) in melt inclusions from "dry" kimberlites, whereas melt inclusions from "wet" kimberlites were found to contain bassanite, pirssonite, and hydromagnesite, consistent with higher amounts of water in the residual magmas. Similarly, Shatsky et al. (2019) identified clinopyroxene in melt inclusions in eclogitic diamonds using *in situ* Raman analysis. Raman can also be used to detect the presence of nanolites in the glass (magnetite nano-crystals 30–1000 nm in diameter) by a peak at ~670 cm-1 (Mujin et al., 2017; Di Genova et al., 2017; 2018). Among the more significant developments in melt

inclusion research in recent years has been the growing recognition that the vapor bubbles in melt inclusions are important reservoirs for volatiles contained in the originally trapped melt. Perhaps the first researcher to recognize the importance of vapor bubbles and attempt to include the contents of the vapor bubble in estimates of formation pressures of melt inclusions was Fred Anderson (Anderson and Brown, 1993), who recognized that the CO_2 content of the glass phase in bubble-free and bubble-bearing melt inclusions from the 1959 eruption of Kilauea Iki was different. These workers further summarized that the "missing" CO_2 in the bubble-bearing melt inclusions was contained in the vapor bubbles and then reconstructed the CO_2 content of the trapped melt based on the bubble size and assumptions concerning the amount of CO_2 in the bubbles using an equation of state. More recently, various researchers have shown that the Raman spectrum of CO_2 varies as a function of CO_2 density (or pressure) and densimeters describing the relationship between splitting of the Fermi diad and CO_2 density (pressure) have been developed (see a summary and comparison of the various densimeters in Lamadrid et al., 2017). Esposito et al. (2008; 2011) combined the earlier methodology described by Anderson and Brown (1993) with the Raman densimeters that had recently been developed to describe a method to reconstruct the volatile contents of melt inclusions by accounting for CO_2 in the vapor bubble. The results showed that a large proportion of the CO_2 in a melt inclusion is hosted in the bubble. Therefore the CO_2 content of the glass alone, and therefore calculated saturation pressures, are significantly under-estimated if the CO_2 content of the bubble is ignored. This has led to a series of studies that applied the Raman densimeter to determine the density of CO_2 in the bubble, followed by a reconstruction of the CO_2 content of the melt that was originally trapped in the melt inclusions (Hartley et al., 2014; Moore et al., 2015; Aster et al., 2016; Drignon et al, 2019a, b). The amount of CO_2 in a melt inclusion vapor bubble that can be detected and quantified depends on the density of the CO_2 in the bubble and the depth of the bubble beneath the surface. In general, the CO_2 content of a vapor bubble that is a few μm or less beneath the polished surface and has a density of greater than approximately 0.05 g/cm^3 can be quantified. An important result of the several recent studies that have been conducted to analyze the proportion of the total CO_2 in the melt inclusions that is contained in the vapor bubble demonstrates that between 30 to 90% of the CO_2 is present

in the vapor bubble. This has important implications concerning the estimated entrapment pressures and degassing paths. Analysis of the vapor bubble in melt inclusions at room temperature usually does not show evidence for H_2O. This is because at these conditions the H_2O that was in the original single fluid phase that exsolved from the melt has condensed to form a thin (nanometer scale) rim of liquid H_2O at the bubble-glass interface that is unresolvable by Raman. However, if the melt inclusion is heated slightly, the liquid H_2O evaporates into the CO_2-rich vapor to produce a homogeneous fluid containing both H_2O and CO_2. Analysis of the bubble at elevated temperature then shows peaks for both H_2O and CO_2, and their relative concentrations can be determined from the peak areas (Berkesi et al., 2009; Lamadrid et al., 2014). As researchers have begun to focus on the analysis of the vapor bubbles in melt inclusions, they have started to recognize other features associated with the volatile components in or adjacent to the vapor bubbles. For example, using Raman spectroscopy, Kamenetsky et al. (2002) identified carbonates, sulfates, sulfides and hydrous silicates at the interface between the vapor bubble and the glass in melt inclusions from various tectonic settings, including For example, using Raman spectroscopy, Kamenetsky et al. (2002) identified carbonates, sulfates, sulfides and hydrous silicates at the interface between the vapor bubble and the glass in melt inclusions from various tectonic settings, including mid-ocean ridges, ocean islands, and various modern and ancient backarc–island arc settings. They suggested that the various phases precipitated after the melt inclusions were trapped and a vapor bubble formed. The volatile components in the vapor bubble (CO_2, H_2O, S) interacted with either the glass in the melt inclusion or with other species in the vapor phase (Ca, Na, Fe, Mg, etc.) to form the carbonates, sulfates, sulfides and hydrous silicates identified by Raman analysis. Similarly, Esposito et al. (2016) identified liquid H_2O, native sulfur and calcite at the interface between the vapor bubble and glass in melt inclusions from the Mount Somma-Vesuvius volcano, Italy, and Moore et al. (2018) identified magnesite, native sulfur and arsenopyrite in vapor bubbles from Klyuchevskoy volcano, Kamchatka. Li and Chou (2015) identified hydrogen (H_2), as well as CH_4, N_2, H_2O, disordered graphite, and possibly higher hydrocarbons, in silicate melt inclusions in quartz from the Jiajika granite in China. These and other studies show that in order to obtain an accurate assessment of the volatile budget of melts using melt inclusions, both the fluid and solid phases in the

vapor bubbles must be quantified and used to reconstruct the original melt composition. An important recent development in Raman spectroscopy that has been applied to melt (and fluid) inclusions is the Raman mapping technique, whereby a 2- or 3-D map showing Raman spectral properties is used to identify and determine the spatial distribution of phases within melt inclusions. Thus, Guzmics et al. (2019) constructed a 3-D Raman map of the vapor bubble within a silicate melt inclusion in nepheline phenocrysts from the Kerimasi volcano in the East African Rift and identified, in addition to a CO_2 fluid, crystals of natrite (Na_2CO_3) and nacholite ($NaHCO_3$) within the bubble. The nacholite is thought to have formed as a result of subsolidus interaction of the CO_2-rich fluid with the surrounding glass.

Best practice:

<u>Type of data produced:</u>
Concentrations of H_2O and CO_2.

<u>Sample requirements:</u>
Solid (glass or minerals) or fluid inside a solid with a flat polished surface.

<u>Analytical conditions:</u>
For analysis of CO_2 in bubbles, it is important to analyze samples of known CO_2 density to confirm the accuracy of the densimeter for the individual Raman instrument (e.g., Lamadrid et al. 2017). Raman can be used to determine the H_2O, and to a lesser extent, CO_2 in the glass phase of melt inclusions, and can identify H_2O, CO_2 and other volatiles in the vapor bubble.

<u>Analytical details:</u>
For CO_2 measurements, the MI will need to be exposed avoiding diamond paste solutions or any carbon-bearing polishing disks, corundum will be preferred and care will be taken to analyze a glassy area far from any cracks, hole or partially-open bubble since all these surface defects are source of contamination.

<u>Reporting requirements:</u>
Report the types of Raman instruments used since there are several commercially available, and different protocols have been used to analyze melt inclusions with Raman, so it is necessary to describe in detail the analytical equipment and conditions so that results from different labs may be compared

Report how the Raman peak positions were calibrated when using peak position to determine compositions or densities.

Often the volatile components in the vapor phase react with the surrounding glass in the melt inclusion to produce hydrous phases as well as carbonates, sulfates and sulfides that are easily identified by Raman. Any calculation methods to quantify the volatile contents of melt inclusions should be described in detail, and volumes of melt inclusions and bubbles should be reported

Report calibration standards used, detection limits, precisions and accuracy.

2.1.2. Fourier transform infrared spectroscopy

Fourier-transform infrared spectroscopy (FTIR) is widely used to analyze H_2O and CO_2 species dissolved in silicate glass and minerals (e.g., see von Aulock et al., 2014). It has the advantage of being relatively inexpensive, easy to use, non-destructive during analysis, and capable of measuring the speciation and concentrations of H_2O and CO_2. The conventional method involves an infrared beam transmitted through a sample. In the ideal case, where melt inclusions are large enough, sample wafers are prepared so that the inclusion is exposed and polished on both sides and spectra are uncontaminated by the host crystal. This is a drawback of FTIR as preparing very small inclusions can be challenging or impossible. Vibrations of different bonds in H-O and C-O species absorb energy at specific wavenumbers. These absorbances are used with the Beer-Lambert law (Stolper, 1982) for calculating species concentrations. The Beer-Lambert law requires knowledge of the molecular weight of the absorbing species of interest, the sample density and thickness, and a composition-dependent molar absorption coefficient (also known as an extinction coefficient). Molar absorption coefficient values have been published for specific melt compositions (e.g., Table 1 in von Aulock et al., 2014), and there are also equations allowing them to be calculated as a function of melt composition (e.g., Mandeville et al., 2002) that can be used. Direct measurements of melt inclusion densities are impractical. As a result, density values are usually calculated on the basis of the chemical composition (e.g., Lange 1997; Ochs & Lange 1999). Thickness can be measured directly (1) using a digital micrometer, (2) by viewing a sample wafer edgewise under the microscope and using the eye-piece reticle (Wallace et al., 1999), or (3) using a stage where the focus depth has been calibrated (e.g., Befus et al, 2012). Alternatively, the thickness of a sample wafer can be determined using the frequency of interference

fringes over an interval of wavenumbers on a FTIR spectra collected in reflectance mode (e.g., Tamic et al., 2001; Wysoczanski & Tani, 2006). In practice this method requires the knowledge of the refractive index (RI) of the material you are analyzing. You can obtain a more accurate measurement of the thickness of the host mineral immediately adjacent to the inclusion where you can use a larger aperture to get better reflectance spectra and because the host mineral's RI is easier to constrain than that of the glass phase (e.g., using Deer et al., 1997). There are errors associated with each of the parameters used in the Beer-Lambert law (Agrinier & Jendrzejewski, 2000), giving an overall error of about 10% relative on the species concentration. Examples of spectra you obtain are shown on Fig. 5.

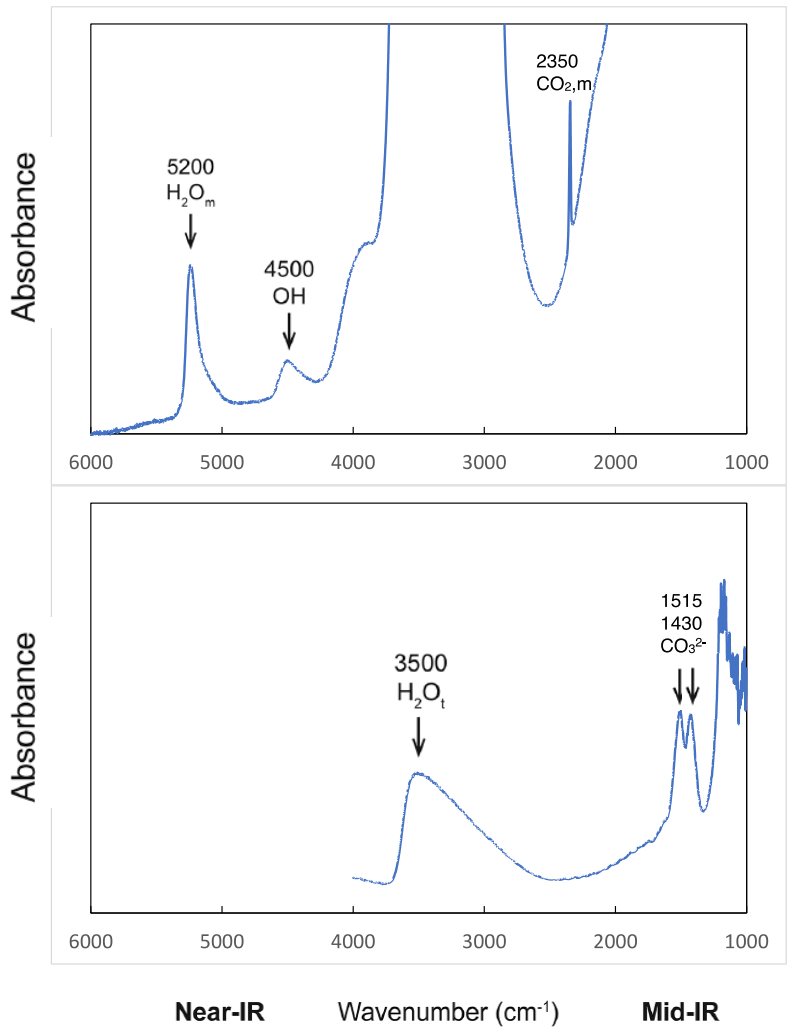

Fig. 5: H_2O and CO_2 absorption bands in FTIR spectra of hydrous rhyolitic (top) and basanitic (bottom) melt inclusions. In the rhyolite spectrum, the 5200 cm^{-1} (molecular

H_2O) and 4500 cm^{-1} (OH) bands can be seen, but the mid-IR fundamental OH stretching band (3550 cm^{-1}), which gives total H_2O, is oversaturated. The 2350 cm^{-1} band (molecular CO_2) can also be seen. In the basanite spectrum, total H_2O is much lower and therefore can been seen at 3550 cm^{-1}. The doublet at 1515 and 1430 cm^{-1} is for dissolved carbonate, which is the primary solution mechanism for CO_2 in mafic compositions. Data are from Roberge et al. (2013) and Rasmussen et al. (2017).

Detection limits depend on sample thickness. Very low volatile contents can only be detected in thicker samples, whereas high volatile contents require thinner samples to avoid saturation of the detector. For example, the detection limits for a basaltic glass inclusion with a 50 µm thickness are ~0.02 wt.% H_2O (at ~3500 cm-1) and ~50 ppm CO_2 as carbonate (both depending on composition, which affects the molar absorption coefficient), but these limits are halved by doubling the wafer thickness to 100 µm. If inclusions are too small to be exposed on both sides, there are other methods that can be applied. Volatile contents of unexposed inclusions can be determined by the Beer-Lambert law as long as spectral contamination from the host crystal does not overlap with the absorbance bands of interest and the thickness of the unexposed inclusion within the host crystal can be measured. Unexposed inclusion thickness can be determined under the microscope as above, as the average of the dimensions of the inclusion in *x* and *y* orientations (Befus et al., 2012; this assumes the inclusion has a regular shape), or using spectral features (Tollan et al., 2019). For inclusions hosted in olivine, the thickness of the olivine in the beam path can be determined using peaks related to olivine and then subtracting this from the overall thickness of the sample wafer (i.e., host crystal + inclusion) to obtain the inclusion thickness (Nichols & Wysoczanski, 2007). In an attempt to further simplify sample preparation, efforts have been made to calibrate reflectance FTIR spectra to calculate concentrations of H_2O and CO_2 species (Hervig et al., 2003). However, reflectance FTIR spectra are much less intense than those in transmitted light resulting in much higher detection limits (~0.5 wt.% water). To improve the signal to noise ratio and reduce detection limits, Yasuda (2014) has conducted FTIR measurements under vacuum using a narrow band detector, reducing detection limits to <0.3 wt.% H_2O. King & Larsen (2013) manipulate reflectance FTIR spectra using a Kramers-Kronig transform, which causes H_2O and CO_2 spectral bands to increase in

intensity, enabling H_2O and CO_2 species concentrations to be calculated with errors of ~20% relative. More sensitive still is micro-attenuated total reflectance (ATR) FTIR (Lowenstern & Pitcher, 2013), where an ATR crystal is placed in contact with the sample surface. This has a detection limit of <0.2 wt.% H_2O and gives errors of about 20% relative. Unfortunately, none of these reflectance methods yields sufficiently low detection limits for either molecular CO_2 or carbonate to enable their analysis in melt inclusions. Use of a synchrotron source, instead of the conventional globar or tungsten-halogen white light bench source, will greatly improve the signal to noise ratio, and thus detection limits, on FTIR spectra in both transmitted and reflected light.

Best practice:

<u>Type of data produced:</u>
Concentrations and speciation of H_2O and CO_2.

<u>Sample requirements:</u>
Solid (glass or minerals) with a flat polished surface. Melt inclusions should be intersected and polished on both sides to avoid host contamination in the FTIR spectra whenever possible.

<u>Analytical conditions:</u>
The adjustable aperture in an FTIR microscope should be set as large as possible without overlapping into the adjacent mineral host. Background spectra should be taken after each melt inclusion spectrum to ensure use of the same aperture setting. Most instruments are set up with both white light and IR (globar) light sources. The white light source provides better intensity for collection of near IR spectra, whereas an IR source is required for analysis of the carbonate doublet peak in basaltic glasses.

<u>Analytical details:</u>
Replicate spectra on a given melt inclusion should be taken with slightly different aperture sizes to check for consistency of results. Reflectance spectra taken to determine sample thickness should be measured on two or three spots on the mineral host adjacent to the inclusion.

<u>Reporting requirements:</u>
Publish measured peak heights in a supplemental table.

Report sample thicknesses, the absorption coefficients that were used to calculate concentrations, the background subtraction method used (e.g., straight line or flexicurve), and the reference used for density calculations.

Inclusions that were not doubly intersected to avoid host contamination in the spectra should be noted and details given as to the correction scheme used to calculate H_2O and CO_2 concentrations.

Report detection limits (if analyzed concentrations are very low), precision estimated from replicate spectra, and accuracy.

Include sample spectra in supplemental material.

2.1.3. X-ray absorption near edge structure spectroscopy

X-ray Absorption Near Edge Structure (XANES) spectroscopy corresponds to the analysis of the spectra obtained in X-ray absorption spectroscopy experiments. XANES spectroscopy is sensitive to element valence state, which, for certain elements, changes in response to the oxygen fugacity of a system. It is a non-destructive *in situ* method with a spatial resolution of about 10×10 µm capable of extracting redox information from silicate glasses. Re-heated melt inclusions may have been re-equilibrated (unless the homogenization was short enough...) and might not give pertinent XANES results. We have focused on measuring the valence state (oxidation state) of Fe in melt inclusions using XANES in fluorescence mode, as this setup is the most common.

The Fe pre-(*K*-) edge peak in Fe XANES spectra is a combination of two peaks corresponding to the photon absorption that arises due to a 1s → 3d electron shell transition. The contributions of Fe^{2+} and Fe^{3+} in a glass are related to the relative intensities of the pre-edge doublet and with increasing fO_2 the relative peak intensities in the doublet changes gradually from Fe^{2+}-dominated to Fe^{3+}-dominated.

a) Sample preparation

For naturally glassy melt inclusions hosted in iron-bearing minerals such as olivine or pyroxene you will need to prepare doubly intersected polished wafers with both sides of the melt inclusion exposed, leaving a clear path through the glass over a minimum 10×10 μm^2 area. The X-ray beam penetrates the sample and interacts with Fe to a depth of several tens of µm, so if you prepare singly polished melt inclusions the X-rays may

interact with the Fe in the host behind the inclusion, or Fe in a standard glass slide, resulting in a contaminated (and therefore useless) fluorescence spectrum. Fe-free glass slides are useful for mounting wafered samples to avoid potential spectral contamination. If the host mineral is entirely iron-free (e.g., quartz, etc.) you can prepare samples that are exposed on one side only.

It is best not to subject your inclusions to any other analytical technique using an X-ray, electron, ion or laser beam prior to XANES analysis. The valence of Fe in the glass can be modified fairly easily by such techniques, especially if the inclusion is water-rich. XANES analysis should therefore be one of the first techniques you subject your inclusion to.

b) Spectrum processing

Fig. 6A shows examples of XANES spectra covering a large range of $Fe^{3+}/\sum Fe$ ratios. The pre-edge region (7110- 7118 eV) at the Fe K-edge corresponds to the 1s→3d electronic transition. This region of the spectrum varies most strongly with changes in Fe valence state and coordination (e.g.,Wilke *et al.*, 2001, 2004; Berry *et al.*, 2003; Farges *et al.*, 2004).

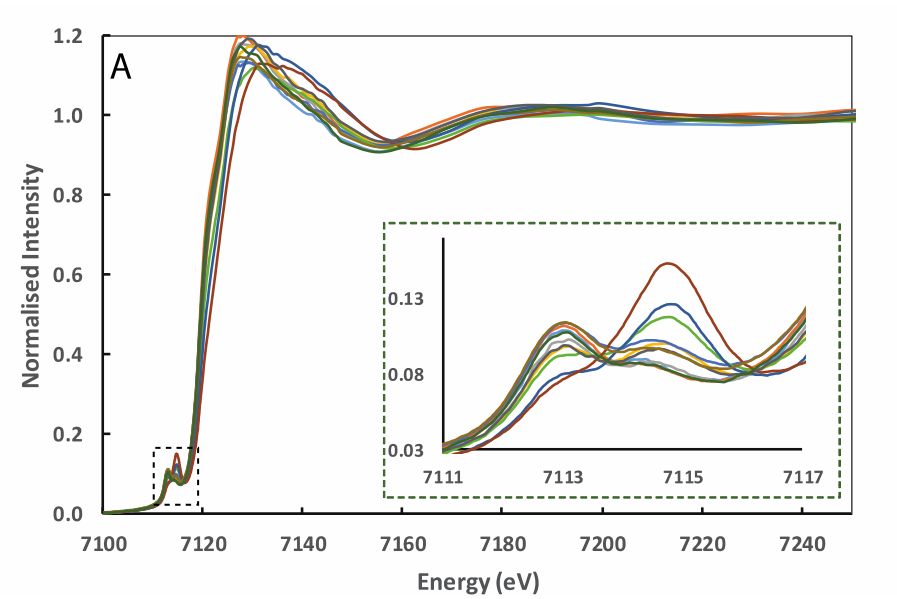

Fig. 6A: Edge-step normalised XANES spectra of the Smithsonian basaltic standard glasses. Inset shows show spectra over the pre-edge region energy range (data from Moussallam et al., 2016).

During XANES analysis the inclusion is typically held at 45° to the incident beam; thus, even spectra from doubly polished inclusions may be contaminated if the incident X-rays interact with the iron-bearing host mineral near the inclusion wall. An easy way to check whether an inclusion can be analyzed without contamination is to measure an intensity profile across the inclusion at a fixed energy above the Fe K-edge. Suitable inclusions will return U-shaped profiles with a flat central region; the beam should be positioned over this central region to make the analysis. If there is no flat central region in the profile, then there is no suitable spot where the inclusion can be analyzed without contamination from the host mineral. Contamination can usually be visually identified in the edge and post-edge part of the spectrum (e.g. Fig. S6 in Moussallam *et al.*, 2014). Principal component regression over the edge and post-edge energy range (7125–7300 eV) can also be used to identify contaminated spectra, since one of the principal components will be correlated with the extent of host contamination (Hartley et al., 2017).

To extract information from XANES spectra, several processing methods have been proposed. The three most common are detailed here.

i. <u>The peak height ratio method</u>

This is the most straightforward method. The relative intensity of the Fe^{2+} (~7112.5 eV) and Fe^{3+} (~7114.3 eV) pre-edge peaks is used to calibrate for $Fe^{3+}/\sum Fe$ ratio (see standards and calibration section). The intensity ratio can either be taken directly from the edge step-normalized spectrum, or after background removal (see centroid method section). This method is advantageous when dealing with noisy spectra that cannot be processed using another method, but its lower precision makes it less suitable for examining small differences in $Fe^{3+}/\sum Fe$ within a sample suite.

ii. <u>The centroid method</u>

This method works best for high-quality spectra, and is less suitable for noisy spectra. The background of the pre-edge region is fitted, often by a combination of linear and damped harmonic oscillator (DHO) functions, and Gaussian functions are then fitted to

the Fe^{2+} and Fe^{3+} peaks. The centroid (area-weighted average) of the background-subtracted pre-edge region is then calculated and parameterized against $Fe^{3+}/\sum Fe$ (e.g., Cottrell *et al.*, 2009; Cottrell and Kelley, 2011, 2013; Moussallam *et al.*, 2014, 2016, 2019a). The centroid method yields very precise results and is ideal for investigating small differences in $Fe^{3+}/\sum Fe$ within sample suites. Because this technique is becoming standard, using it has the added advantage of increased inter-study comparability.

iii. <u>The principal component regression method</u>

Principal component regression (PCR) identifies spectral features corresponding to the maximum variance in the dataset through conventional principal component analysis (PCA). The principal components are linearly correlated with $Fe^{3+}/\sum Fe$, meaning that reference spectra can be used to generate a linear mixing model to determine Fe3+/∑Fe in unknowns (e.g., Farges *et al.*, 2004; Shorttle *et al.*, 2015; Hartley *et al.*, 2017). An advantage of the PCR method over the critical pre-edge region of 7105–7119 eV is that it uses all redox-sensitive features of the spectra, including the absolute position of the main absorption edge, and hence is theoretically most sensitive to small differences in $Fe^{3+}/\sum Fe$ between spectra.

c) Standards and calibration

XANES is not an absolute analytical method, and the pre-edge feature is sensitive to coordination geometry as well as valence state; therefore it always requires reference materials of similar composition to be analyzed during the same analytical session as the unknowns to obtain a valid calibration (Fig. 6B; modified from Moussallam et al., 2019a).

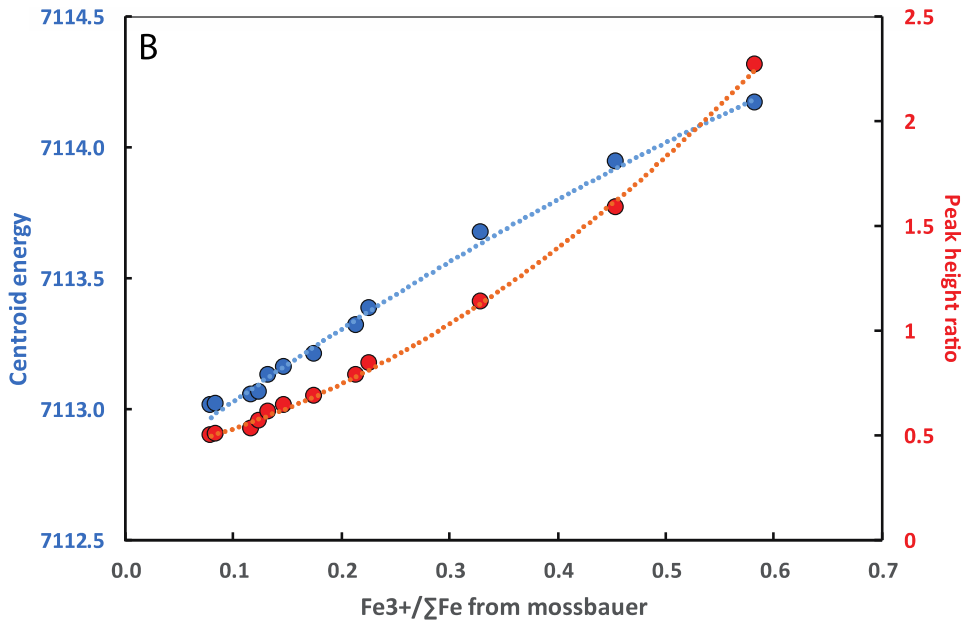

Fig. 6B: Calibration curve for the centroid position (blue) and peak height ratio (red) determined by XANES compared with the $Fe^{3+}/\sum Fe$ ratios of the Smithsonian basaltic standard glasses determined by Mössbauer spectroscopy (data from Moussallam et al., 2019a).

However, in the specific case of andesites and hydrous basaltic glasses, a calibration with anhydrous basalts standards has proven to be adequate (Dauphas et al., 2014, Zhang et al., 2016, 2018; Cottrell et al 2018) provided there is no beam damage. This means that while XANES measurements can be very precise, their accuracy is only as good as that of the independent method(s) used to determine the $Fe^{3+}/\sum Fe$ in the reference standards (usually Mössbauer spectroscopy or wet chemistry). To measure the absolute oxidation state of Fe in melt inclusions, well-characterized standards are critical.

Available international standards

Standards should be selected to match the composition of the unknowns as closely as possible. The Smithsonian Institution National Museum of Natural History (NMNH) holds three sets of reference glasses of basaltic, andesitic and pantelleritic compositions (Cottrell *et al.*, 2009; Zhang *et al.*, 2016) that can be requested by any researcher through their loan program. These standard sets have been widely used and are particularly useful for direct inter-study comparisons. The absolute calibration of the NMNH basaltic glass standards (Cottrell *et al.*, 2009) has been the subject of contention. Two independent

revisions of their calibration have been proposed (Zhang *et al.*, 2018; Berry *et al.*, 2018), diverging because of different interpretation of the corresponding Mössbauer spectra. Other authors have created sets of standards for basalt (e.g., Berry *et al.*, 2003; Wilke *et al.*, 2004; Botcharnikov *et al.*, 2005; Dauphas *et al.*, 2014), andesite, dacite, rhyolite (e.g., Dauphas *et al.*, 2014), alkali-silicate glasses (e.g., Knipping *et al.*, 2015), basanites (e.g., Moussallam *et al.*, 2014), haplotonalites, haplogranites (e.g., Wilke *et al.*, 2006) and felsic glasses (Fiege et al., 2017). Some of these standards may be available on request. To date, most standard suites have been synthesized at 1 atmosphere and are therefore mostly volatile-free.

<u>Making your own standards</u>

While international standards offer useful opportunities for inter-study comparisons, they may not cover the compositional or fO_2 range of interest to your study. In this case, it is best to create your own standards by synthesizing glasses of the desired compositions over a range of fO_2 conditions using experimental apparatus such as a 1 atmosphere vertical gas-mixing furnace. Fe loss during the experiment should be dealt with either by using Re wires or pre-saturated Pt wires (at oxygen fugacities of FMQ-1 or below; with Pt wires pre-saturated with Fe). Under these conditions, there is limited Fe loss and hence no need to keep the experimental duration short. Sodium loss through volatilization is a tough problem to deal with, and pending a more elegant solution, it is best to use as much material as possible in order to minimize the surface-to-volume ratio of the bead, and to use the lowest gas flow rates possible. The $Fe^{3+}/\sum Fe$ of the synthesized materials must be determined by one or several independent methods before using them as XANES standards. The reference materials should cover the full range of expected natural variability in $Fe^{3+}/\sum Fe$ in the unknowns, and at an appropriate resolution.

d) Beam damage

Beam damage refers to changes to the sample composition induced by interaction with a monochromatic X-ray beam, such as oxidation/reduction of a cation and/or element migration. In silicate glasses the effect was first noticed for XANES analyses at the S K-edge (e.g., Wilke *et al.*, 2008; Métrich *et al.*, 2009; Klimm *et al.*, 2012; Moussallam *et*

al., 2014) but had previously been shown in S K_a shift measurements by electron microprobe (Wallace and Carmichael 1992; Rowe *et al.*, 2007). The extent of X-ray-induced photo-oxidation or reduction of Fe in silicate glasses is dependent on the glass composition, water content, and the photon flux (Goncalves Ferreira et al., 2013; Cottrell *et al.*, 2018). Fig. 6C shows the effect of using different beam attenuation conditions on the extent of induced beam damage during XANES analyzes of a water-rich basaltic glass. Inappropriate analytical conditions may result in extensive beam damage of unknowns, and hence unreliable results.

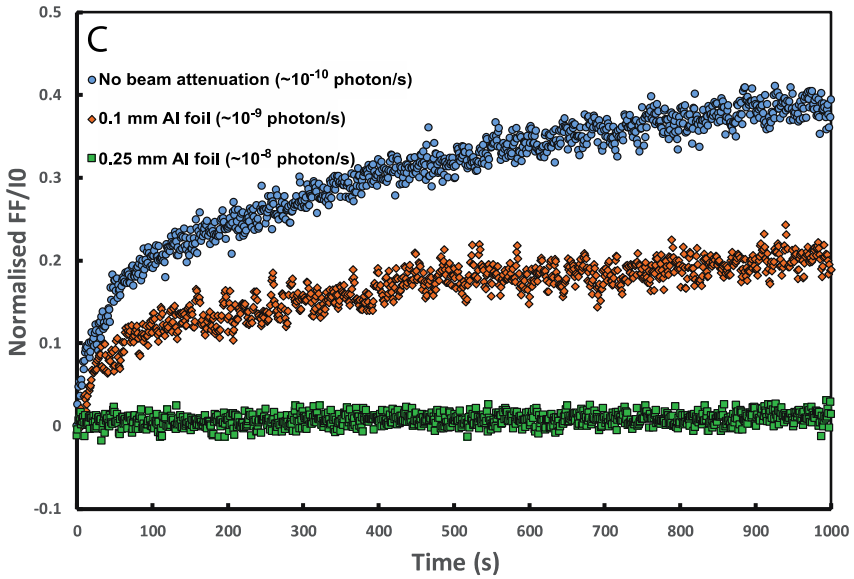

Fig. 6C: Time series of normalised fluoresced intensity (FF) over I0 at 7114.3 eV integrated over 1 s intervals for a hydrated (5.2 wt.% H_2O) basalt under three different beam attenuation conditions. A fresh spot was illuminated with a 2.5×1.2 µm beam for each analysis. Note that while photo-oxidation can clearly be seen with no beam attenuation and with an attenuation down to about 16% of the original beam flux (using a 0.1 mm Al foil), no photo-oxidation can be detected once the beam has been attenuated down to 1% of its original flux (using a 0.25 mm Al foil; data from Moussallam et al., 2019a)

Best practice (XANES):

<u>Type of data produced:</u>

Valence state of element of interest (examples detailed here are for Fe K-edge studies giving $Fe^{3+}/\sum Fe$)

Sample requirements:

Solid (examples detailed here are for glasses). For melt inclusions hosted in iron-bearing minerals such as olivine or pyroxene you will need to prepare doubly intersected polished wafers with both sides of the melt inclusion exposed, leaving a clear path through the glass over a minimum 10×10 μm^2 area. It is best is not to subject your inclusions to any other analytical technique using an X-ray, electron, ion beam or laser prior to XANES analysis. The valence of Fe in the glass can be modified by such techniques especially if the inclusion is water rich. XANES analysis should therefore be one of the first techniques you subject your inclusion to.

Analytical conditions:

Every XANES study should begin with a series of tests to define the analytical conditions under which the samples can be analyzed without inducing detectable beam damage. Tests should be performed on natural or synthetic glasses that have the same composition and the same (or higher) water content as the unknowns. The most common test is to illuminate the sample at a fixed energy, for example the Fe^{3+} peak of the pre-edge doublet at 7114.3 eV, and monitor the normalized fluoresced intensity during exposure to the beam (Fig. 6C in supplementary informations) (Burnham et al., 2010, 2014; Shorttle *et al.*, 2015; Cottrell *et al.*, 2018; Moussallam et al., 2019a). Another common test is to perform rapid scans to collect a series of complete spectra over short time periods (tens to hundreds of seconds depending on the setup) and monitor the evolution of the pre-edge region during beam exposure (e.g., Moussallam et al., 2014, 2016). As a result, specific analytical conditions will vary based on individual studies/samples. Generally, the scan region for Fe K-edge studies goes from 7000 to 7350 eV and the pre-edge region (7110-7118 eV) is typically acquired at higher resolution.

Analytical details:

XANES is not an absolute analytical method and therefore always requires reference materials of similar composition to be analysed during the same analytical session as your unknown to obtain a valid calibration. This means that while XANES measurements can be very precise, their accuracy is only as good as that of the accuracy of the independent method used to determine the $Fe^{3+}/\sum Fe$ in the reference standards (usually Mössbauer spectroscopy or wet chemistry). During XANES analysis the inclusion is typically held at 45° to the incident beam; thus, even spectra from doubly polished inclusions may be contaminated if the incident X-rays interact with the iron-bearing host mineral near the inclusion wall. An easy way to check whether an inclusion can be analysed without contamination is to measure an intensity profile across the inclusion at a fixed energy above the Fe K-edge. Suitable inclusions will return U-shaped profiles with a flat central region; the beam should be positioned over this central region to make the analysis. If there is no flat central region in the profile, then there is no suitable spot where the inclusion can be analyzed without contamination from the host mineral. Contamination can usually be visually identified in the edge and post-edge part of the spectrum (e.g. Fig. S6 in Moussallam *et al.*, 2014). Principal component regression over the edge and post-edge energy range (7125-7300 eV) can also be used to identify contaminated spectra, since one of the principal components will be correlated with the extent of host contamination (Hartley et al., 2017).

Reporting requirements:
Report the synchrotron, beamline, beam dimensions, monochromator, mode, detector, energy step sizes, dwell time, incident photon flux, photon density at the sample surface and geometry of the setup. Report results of your beam damage tests, for instance as a time series such as Fig. 6C in the supplementary materials. Report calibration standard used, calibration results and precisions and accuracy. We encourage publication of raw and edge step-normalized spectra from all unknowns and standards as supplementary information. Report the full composition, including volatile content of your unknowns and standards.

2.1.4. Secondary ion mass spectrometry

Secondary Ion Mass Spectrometry (SIMS) is a microanalytical technique that utilizes a finely focussed beam of primary ions (O^- or Cs^+ are most common for geochemical applications) to sputter secondary ions from the surface of a solid substance. These secondary ions are subsequently analyzed using a specially adapted mass spectrometer. As such, SIMS provides an extremely versatile tool for analysis of glassy melt inclusions that have experienced little or no PEC.

In addition to quantitative trace element (e.g., REE and other incompatible elements) and volatile (e.g., H_2O, CO_2, S, Cl, F; Hauri et al 2002a, Hauri 2002b ; Bracco Gartner 2019; Cadoux et al., 2017) analysis, a specific strength of SIMS is sub-per mil precision and reproducibility for a wide variety of stable isotope ratio determinations (δD, δ^7Li, δ^{11}B, δ^{34}S, δ^{37}Cl; Hauri, 2002b; Layne 2006; Manzini et al., 2017a) and radiogenic isotopes (^{204}Pb/^{206}Pb/^{207}Pb/^{208}Pb, Layne and Shimizu 1998a, 1998b, Kobayashi et al 2004).

In general, a lateral spatial resolution of 10 µm (with sputtered pit depths of less than a few µm) may be achieved for individual analyses (total sample size < ~10 ng). *In situ* SIMS microanalysis is thus compatible with the size range of many melt inclusion populations. Samples commonly require only simple preparation of a flat polished surface that exposes the melt inclusions, thus preserving information on both host minerals and textural context - although samples and mounting media must be compatible with the ultra-high vacuum of the SIMS sample chamber. Therefore, many SIMS facilities now encourage sample preparation in indium mounts for certain applications. A thin conductive layer, usually ultra-pure Au, is applied to the sample surface to mitigate

charging during analysis. Balanced electron flooding may also be required during analysis if using Cs^+ primary ion beams.

For determination of volatiles (F, Cl, S and especially H_2O and CO_2; Hauri et al., 2002a,b; Koga et al., 2003), or for light stable isotopes of trace element analytes (e.g., $\delta^{11}B$, Chaussidon et al., 1997; Straub and Layne 2002), an intrinsic advantage of SIMS is the ability to combine pre-sputtering of the sample surface with an appropriately restricted effective field of view (Field Aperture) for ions entering the mass spectrometer. This approach can be used to reduce extraneous signal from surface contamination to an insubstantial level – in fact, often well below the comparable "blank" levels that limit some other mass spectrometric approaches.

SIMS instruments are designed to resolve the complex mass spectra of secondary ions produced by the ion beam sputtering of solid materials, using energy filtering and/or mass resolution approaches (Layne, 2006). Degree of ionization to simple (generally monoatomic) secondary ions during sputtering varies by element, primary beam and major element matrix. As a consequence, quantification requires comparison to reference materials of similar bulk composition to the sample (Fig. 7), and the use of appropriate and well characterized reference materials is an important consideration in all forms of SIMS microanalysis. In the specific case of isotope ratio analysis, reference materials are required to calibrate for the combined instrumental mass fractionation (IMF) effects related to mass dependence in production of analyte secondary ions by sample sputtering, and to mass dependent effects in the ion detectors.

Many analyses are readily accomplished using smaller format (e.g., Cameca f-series) SIMS instruments (for example, $\delta^{11}B$; Chaussidon et al 1997). However, larger format (e.g., Cameca 1270/1280/1300HR) instruments have significant advantages for some analyses, especially those where a trace element analyte is used for isotope ratio analysis; for example, $\delta^{7}Li$ (Bouvier et al., 2008), $\delta^{11}B$ (Rose et al., 2001; Straub and Layne 2002) or $\delta^{37}Cl$ (Layne et al, 2009; Bouvier et al., 2019). The multi-collection arrays of larger format instruments can also become invaluable for the determination of $\delta^{37}Cl$ (Manzini et al 2017a, Fig. 7), $\delta^{18}O$ (e.g., Hartley et al., 2012; Manzini et al., 2019) or $\delta^{34}S$ (Cabral et

al., 2013) and both precision and accuracy for Pb isotope analysis can be improved (e.g supplementary material in Rose-Koga et al., 2012).

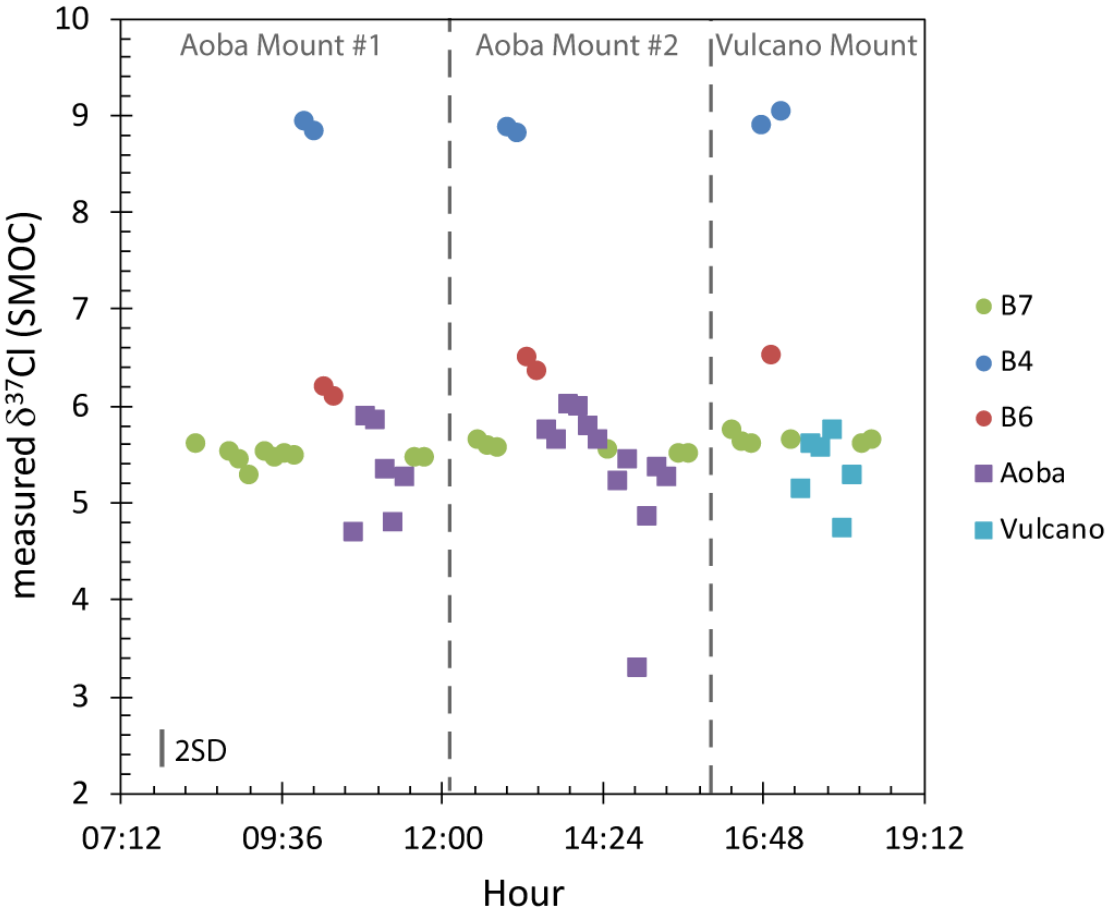

Fig. 7: Example of chlorine isotopes measurements by SIMS (not corrected for IMF) over a day. Round symbols represent different in-house standards, square symbols are for the melt inclusions samples from Aoba (Vanuatu) and Vulcano (Italy) volcanoes. Data are from Manzini et al. (2017).

Due to the gradual removal of material by sputtering, SIMS also inherently accumulates a time-resolved depth profile of the sample, allowing the selective elimination of signals from defects or micro inclusions. Image acquisition of elements via large geometry SIMS is also possible by rastering a large area (up to 500 µm squared), and accumulation of image layers allows 3D imaging of melt inclusions (Florentin et al., 2018). Imaging and diffusion profiles between melt inclusions and their host are more precise when using a Cameca NanoSIMS instrument. Indeed, due to a different geometry and ion

optical design, NanoSIMS can achieve superior lateral spatial resolution, typically 100–200 nm) compared to typically 10 μm for other SIMS instruments. NanoSIMS has been used, for example, to map the volatile distribution in and around melt inclusions (Hauri et al., 2011; Le Voyer et al., 2014). Similarly, to estimate residence time or ascent rate, exceptionally fine scale diffusion profiles can be obtained for volatile elements (e.g. Lloyd et al., 2014; Newcombe et al., 2014; Moussallam et al., 2019b) or trace elements (e.g. Manzini et al., 2017b).

There are a number of recent or on-going improvements in SIMS analysis that may contribute to the expansion of frontiers of melt inclusion research. Progressive improvement in SIMS capability for lateral imaging of trace elements has been left generally unexplored for applications such as assessing diffusion profiles between melt inclusions and host minerals. New finer spatial resolution and denser primary sources (e.g., Hyperion II™ RF O^- source) have the potential for applications to ultra-small inclusions, improved measurements of diffusion profiles by step traverse or imaging, and the informative assessment of microlites and other inhomogeneities within individual melt inclusions, as well as better precision on stable isotopes of trace elements (δ^7Li, δ^{11}B). Also, development of more sensitive detectors (for example, Faraday cup associated with 10^{12} Ω resistor) will allow a better precision on some stable isotopic systems (e.g., δ^{37}Cl, δ^{34}S) over a large range of composition of the targeted analyte.

Best practice:

<u>Type of data produced:</u>
Concentrations of volatile elements and isotope compositions.

<u>Sample requirements:</u>
Solid (glass or minerals) with a flat polished surface. Samples should be pushed in indium mount. High vacuum pre-preparation is especially important for the analysis of CO_2 or δD (Hauri et al 2002a), and preparation in an indium (instead of epoxy) mount is encouraged (mandatory in certain SIMS hosting institutions). Samples should be kept at least overnight in the airlock of the SIMS or several days in an oven at 70ºC prior to measurements.

<u>Analytical conditions:</u>

1) Provision of well characterized matrix-specific reference materials for the calibration of elemental concentrations and instrumental mass fractionation (IMF). A piece of the appropriate standard material(s) (acting as secondary standard) should be placed in each sample mount, in order to monitor possible instrumental drift or possible mount conductivity trouble. 2) Elimination of sample surface contamination and other exotic contributions through pre-sputtering and other means, including pre-preparation in high vacuum where necessary. 3) Calibration of accuracy and sensitivity (or relative sensitivity) of ion detectors (whether single or multiple array) over an adequate dynamic range. This last consideration is especially important for stable isotope determinations.

Analytical details:

For CO2 measurements, the MI will need to be exposed avoiding diamond paste solutions or any carbon-bearing polishing disks, corundum will be preferred and care will be taken to analyze a glassy area far from any cracks, hole or partially-open bubble since all these surface defects are source of contamination.

Reporting requirements:

Report the instrument manufacturer, model used for analyses.

Report the primary beam used (O2-, Cs+…), the use of electron gun or not and the intensity of the primary beam. The values of the contrast aperture and field aperture and the mass resolving power (MRP) should also be given and varies between concentration measurements and isotope measurements.

Report the counting time on each mass of elements, the pre-sputtering time and the deadtime applied. For comparison with other studies, the useful yield for the element of interest could be reported.

Report calibration standards used, detection limits, precisions and accuracy.

2.1.5. Electron Microprobe

Electron probe microanalysis (EPMA) is used to measure major and some volatile elements *in situ* in melt inclusions and their hosts. Since this analytical technique requires carbon coating the sample to make the surface conductive, it is best when possible to carbon coat the sample and conduct EPMA analyses after CO_2 has been analyzed by SIMS. Beam damage can be significant during EPMA of both mafic and rhyolitic composition, especially for hydrous glasses, resulting in mobile element migration (Na, K, and H; e.g. Morgan and London 1996; Humphreys et al., 2006), elevated concentrations of immobile elements (Si, Al; e.g. Morgan and London 1996), and redox

changes to Fe and S (e.g. Fialin et al., 2001; 2004; Fialin and Wagner, 2012). Therefore, the analytical conditions and routine must be carefully chosen. For instance, time-dependent intensity corrections can be used to correct for changes in element concentrations during analysis by extrapolation back time zero (Nielsen & Sigurdsson, 1981). Also, using mean atomic number (MAN) background (uses the measured relationship between background counts and MAN, rather than measured off-peak backgrounds, to calculate the background, Donovan & Tingle 1996) reduces analysis time and beam damage.

Using lower intensities, 2 to 4 nA, avoids migration but then count rates are low (e.g. Morgan and London, 1996). An alternative is to use two different beam conditions at a single location by analyzing Na, K, Si and Al at a first condition of 8–10 nA, and then the rest of the major elements and volatiles at a higher current of 40 nA. If limited in time and/or only allowed one beam condition, an 8 nA beam current, an accelerating voltage of 15 kV and a 20 µm defocused beam is recommended for glass analysis as repeated analysis (more than 1500 measurements) of the anhydrous basaltic standard VG-A99 show no significant sodium loss (Oladottir *et al.* 2011). Other studies have shown that for hydrous basaltic MI from arc samples, a substantial Na migration happens even at 10 nA (e.g. Vigouroux et al., 2008; Ruscitto et al., 2011). A weaker current of 4 nA is usually recommended in these cases to avoid sodium migration but results in a signal that is twice as low and longer counting times are required (on the order of 4 times longer). A beam size beyond ~20 µm will result in the wavelength dispersive spectrometers, which measure the X-ray intensities, going out of focus. Typical analytical uncertainties (1σ) in these conditions, obtained from replicate measurements of the basaltic glass standard VG-A99 (Jarosewich et al. 1979) are typically less than 3% for FeO and K_2O, 5% for Na_2O and P_2O_5, 30% for MnO and 2% for the other oxides. A test for the effect of beam defocusing on the analytical reproducibility consists of comparing analyses done with a 10 and 20 µm beam size in a single melt inclusion.

Chlorine, sulfur and fluorine analyses are best performed at higher currents, 40–80 nA, to ensure higher count rates, and with a 10–20 µm defocused beam together with the trace element acquisition program proposed in the company software (for example Cameca Peak Sight software). This quantification model takes into account the matrix

composition of the glass to calculate the trace element concentration. Details of the volatile element measurements are given elsewhere (e.g., Rose-Koga et al., 2017 and 2020). Depending on the counting times of Cl, S and F, detection limits can reach ~50, 50, and 150 ppm, respectively. The total analytical error for S, Cl, and F including precision and accuracy of measurements, is typically of 20% (relative uncertainty) for S, and 30% for Cl and F over the range of concentrations found in inclusions. There is excellent agreement between EPMA and SIMS measurements for F concentrations above 150 ppm and on 10 widely available referenced standards (Rose-Koga et al., 2020; Fig.

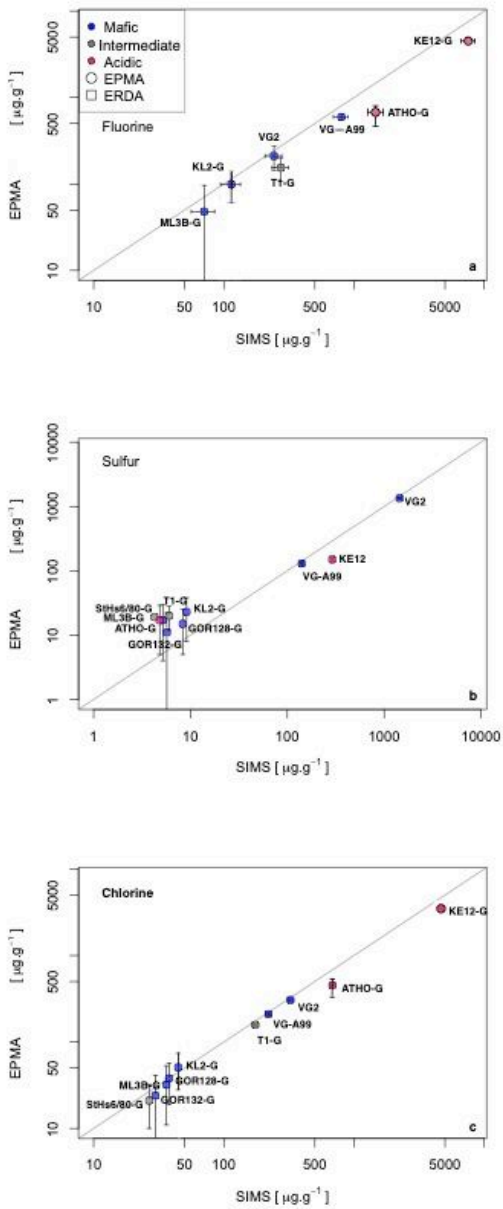

8).

Fig. 8: Log-Log plot of concentrations of F (**a**), S (**b**), and Cl (**c**) measured by SIMS vs. that measured by EPMA (circles). Standards are categorized according to their SiO_2 contents into mafic, intermediate, and acidic. The solid line is a one-to-one slope indicating the coherence of the fit (modified from Rose-Koga et al., 2020).

Precision and accuracy can be improved for EPMA at low concentrations (e.g., in MORB or ultra-depleted inclusions) by using two or more spectrometers simultaneously for the same element. Large analyzing crystals on some microprobes also provide lower detection limits and better precision. While analyzing elements with low concentrations (<100 ppm), it is also useful to run a "blank" by analyzing a material that has ≈0 ppm of the element(s) of interest to ensure that sample surfaces are not contaminated and that backgrounds are chosen correctly. A clear spot in the host crystal is readily available and is a good choice for many incompatible elements. SIMS analytical precision as well as detection limits on Cl, S, F are usually smaller (< 5% relative) and lower (< 10 ppm typically), but using EPMA has the advantage of being more accessible and less expensive. Given that S can occur in multiple oxidation states in a melt (Carroll and Rutherford, 1988; Jugo et al., 2010), the choice of standards and S-peak position measurement need to be considered for each sample suite.

Less commonly, EPMA is used to measure the S oxidation state of melt inclusions, as the peak position of SKα shifts with changes in oxidation state (e.g., Wallace & Carmichael, 1994). For such measurements, the spatial resolution is ~50 μm^2 with an error of ±0.05 on S^{6+}/S_{total} (e.g., Rowe et al., 2007). It has been shown that changes in the oxidation state of multivalent elements such as Fe and S may occur under the electron beam from overheating of inclusions, and therefore moving the beam position incrementally at a rate of 1μm/min seems to avoid the apparent increase in λ(SKα) (Wallace & Carmichael, 1994; Rowe et al., 2007).

Although not a direct measurement "volatiles by difference" (VBD), an estimate of the H_2O+CO_2 content of the glass, can be calculated from the difference between 100 wt% and the analytical total (e.g., Devine et al., 1995, Humphreys et al., 2006, Hughes et al., 2019). For very high CO_2, the CO_2 could be as much as 30% of the VBD value (e.g. Ross Island basanites, Rasmussen et al. 2017), in other cases authors have often assumed that

the CO_2 content was almost always so low in comparison to H_2O content, so that what they got by this difference method was H_2O. Profiles of major elements within melt inclusions can be used to estimate cooling timescales (Newcombe et al., 2014).

Best practice:

Type of data produced:

Concentrations of major and minor elements (including some volatile elements)

Sample requirements:

Solid (glass or minerals) with a flat polished surface; mount sample in indium (rather than epoxy) if you plan to do volatile analysis of the same sample mount using SIMS; do SIMS analysis before EPMA if you plan to carbon-coat the sample. Best results obtained if MI is greater than about 10 microns in diameter to avoid including host phase in the analysis. MI should not contain multiple solid phases (but may contain a vapor bubble). The area to be analyzed must be exposed on the sample surface.

Analytical conditions:

Analytical conditions will vary depending on what is being analyzed (glass versus mineral), mineral type and element. Use analytical conditions that are appropriate and analyze elements in an order that minimizes modifications, such as diffusion of Na, upon exposure to the electron beam. Calibrate using a standard that closely matches the unknown to be analyzed to avoid matrix effects.

Analytical details:

Analyze multiple spots if the MI is large enough (great than about 25 microns).

Measure the host composition in 2-3 different locations close (< 20 microns) to the melt inclusion. This may not be required for MI in quartz, depending on the question/problem being addressed

If doing transects to determine zoning of the host phase, collect two transects radial to the melt inclusion (90º from one another).

Reporting requirements:

Report the instrument manufacturer and model of the electron micropbe used for analyses.

Report calibration standards used and analytical conditions for each element analyzed (beam current, accelerating volatge, beam diameter, counting time, analytical uncertainties).

Report the size and shape of each MI analyzed and include a photomicrograph of each MI in supplementary data. On the photomicrograph place a mark to indicate the location

of each analysis within the MI and the surrounding host phase. Use the same identifier on the photo and in the data tables to allow easy comparison (i.e., a given analysis might have an identifier such as: 08102019-A-IV-1 where:

08102019 is the sample number (here it is identified based on the date it was collected – August 10, 2019.

A is the phenocryst or crystal in sample "08102019"

IV is the label for the MI in phenocryst "A" in sample "08102019"

1 is the first analysis of MI "IV" in phenocryst "A" in sample "08102019"

2.1.6. LA-ICP-MS

Laser Ablation-Inductively Coupled Plasma-Mass Spectrometry (LA-ICP-MS) is perhaps the most easily accessible and frequently used method for micro-analysis of minor and trace elements in melt inclusions and their mineral hosts. This method involves pulsing a UV wavelength laser (213 Nd-YAG or 193 nm ArF are most common) at a set frequency to ablate a small spot (tens to hundreds of μm) in a sample. The ablated material is swept away in a carrier gas (commonly He, Ar, or a mixture of the two) and transported to an inductively coupled plasma for ionization, and analysis by mass spectrometry. We note that if SIMS analysis were performed on the MI using the cesium (Cs) source, then Cs will be inplanted in the sample (Mourey et al., 2017) and laser data on Cs trace element measurements should be discarded. Advantages of this method over others (e.g., SIMS) include relatively low cost, rapid sample throughput, less matrix sensitivity, and a large suite of analyzable elements. Another major advantage is that LA-ICP-MS allows simultaneous analysis of elements over a 9-10 order of magnitude concentration range, thus permitting analysis of major (wt. %), minor and trace (ppb to ppm) elements at the same time. Yet, this method of analysis is particularly destructive to the sample, and so should be the final analytical method used in any planned sequence of analyses on a melt inclusion.

A background of the ICP-MS signals with the laser off is usually collected at the beginning of each analysis (~30-40 s), and an average of this background is then subtracted from the average count intensity on the sample for each element. Background-subtracted intensities are then typically normalized to the signal of an internal standard element whose concentration may either be inferred from stoichiometry or independently determined using another analytical method (e.g., for glasses, ^{47}Ti, ^{43}Ca, and ^{29}Si are

commonly used; Kelley et al., 2003; Lytle et al., 2012; Jenner & O'Neill, 2012). The technique is calibrated by analysis of a suite of standard glasses of known composition within the same analytical session as the unknowns. The effect of variable concentrations of the internal standard element from one sample or standard to the next is factored out of the normalized signal intensity through multiplying by its concentration. These modified intensities may then be referenced against known element concentrations in a suite of standards to build a working calibration curve that allows quantification of element concentrations in unknowns. For glasses many useful reference standards are now available (e.g., NIST, USGS, MPI-DING). Calibration methods vary among laboratories (e.g., a single-point calibration [Jenner & O'Neill, 2012] vs. a curve built from multiple reference glasses [Lloyd et al., 2013; Kelley et al., 2003]), but for inter-laboratory bias assessment, best practice should be to report the analysis of at least one reference standard run as an unknown. Some commercial software packages (e.g., GLITTER) and free software (AMS; Mutchler et al., 2008) are available to assist with data management and calculations. Most commercial laser systems allow users to adjust the spot size, either using a set of fixed-diameter round apertures or a rectangular spot whose dimensions may be controlled dynamically. In general, the larger the ablated area, the higher the signal intensity, so for melt inclusions, one larger spot will generate higher quality data for low-abundance elements than two smaller spots.

Because of the aggressive rate of sample consumption via laser ablation, sample thickness limits the duration of useable data. For thin samples, such as wafers prepared for FTIR or XANES, ablation time may be extended by slowing the repetition rate of the laser (e.g., from 10 Hz to 5 Hz; Kelley & Cottrell, 2012). Awareness of heterogeneities with depth in the sample is also important for LA-ICP-MS analysis, and spots should be placed to avoid vapor bubbles, co-included phases, and the host crystal if at all possible. In some cases, especially with partially to completely crystallized melt inclusions, it is necessary to analyze melt inclusions that are unexposed to avoid preferentially removing some portion of the heterogeneous melt inclusion contents during polishing to expose the melt inclusion at the mineral surface (Severs et al., 2007). In this case, the melt inclusion plus some amount of host phase that is above, peripheral to, and below the melt inclusion will be sampled. Then, the host contribution can be mathematically subtracted if the

concentration of one element in the MI is known, and the composition of the host is known (e.g., Halter et al., 2002). For this reason, at least one clean LA-ICP-MS analysis of the host mineral should accompany any melt inclusion analysis, in the event that it is necessary to reconstruct the melt composition by subtracting the contribution from the host.

Best practice:

Type of data produced:

Concentrations of major, minor, and trace elements

Sample requirements:

Solid (glass or minerals) with a flat polished surface; specific mounting media are not proscribed because these don't affect the performance of the laser, and most laser systems will accept a variety of common mounts including 1" round mounts typical for EPMA or SIMS analysis, and standard petrographic thin sections. Best results obtained if MI is greater than about 50 microns in diameter to ensure sufficient signal intensity and to avoid including host phase in the analysis. In the best case, MI should not contain multiple solid phases (but may contain a vapor bubble), although crystallized inclusions can be analyzed with meaningful results if the entire volume of the inclusion is ablated in bulk during analysis. The area to be analyzed may either be exposed on the sample surface or be unexposed below it, within a volume that the laser will ablate through time.

Analytical conditions:

Analytical conditions will vary depending on what is being analyzed (glass versus mineral), mineral type and element. Spot size is one of the most commonly adjusted instrument settings during LA-ICP-MS analysis, and it is advantageous to analyze a single, large spot instead of 2-3 smaller spots because the larger spot will produce greater signal intensity and enable better determination of the lowest-abundance elements. For thin samples (e.g., those that have been wafered for FTIR or XANES analysis), it can be advantageous to decrease the laser repeat rate (e.g., from 10 Hz to 5 Hz). Although this decreases the signal intensity, it increases the duration of ablation within the sample and ensures a quantifiable plateau in the spectrum (~20 seconds is a fair rule of thumb). Calibrate using standards that are similar to the unknowns to avoid matrix effects.

Analytical details:

Analyze multiple spots if the MI is large enough (> ~100 μm).

Measure the host composition close (< 20 microns) to the melt inclusion. This is particularly important if there is accidental contamination of the inclusion spectrum with the host mineral, and also for determining partitioning if desired.
For quantification of LA-ICP-MS data, you must either have previous analysis of an internal standard element by another method (e.g., Ca or Ti by EPMA), or you must be able to assume a stoichiometric concentration of an analyzed element in the host mineral
If doing transects to determine zoning of the host phase, collect two transects radial to the melt inclusion (90º from one another). If it is possible to customize the dimensions of the laser (e.g., with a rectangular, rotatable aperture), align the long axis of the rectangle perpendicular to the transect to afford the highest spatial resolution.

<u>Reporting requirements:</u>
Report the instrument manufacturer and model of the ICP-MS and the manufacturer, model, and wavelength of the laser ablation system.
Report calibration standards used, reference or report the concentrations used for calibration, and tabulate analytical conditions for each element analyzed (isotope, dwell time, resolution), and report the energy output of the laser in units of fluence (mJ/pulse/μm^2). Report any methods used to correct for interferences. Report the reproducibility of multiple spots, if applicable, and the analysis of a reference glass analyzed as an unknown.
Report the size and shape of each MI analyzed, and its vapor bubble if relevant, and include a photomicrograph of each MI in supplementary data. On the photomicrograph place a mark to indicate the location of each analysis within the MI and the surrounding host phase, or provide a labeled post-analysis photomicrograph showing the spots. Use the same identifier on the photo and in the data tables to allow easy comparison.

2.2. Radiogenic isotopes in melt inclusions

Analysis of radiogenic isotope ratios in melt inclusions is challenging because their size and elemental concentrations limit the available amount of the element of interest. In the late 90s, a pioneering study by Saal et al. (1998) used *in situ* SIMS techniques to determine Pb isotope compositions (including $^{208}Pb/^{206}Pb$ and $^{207}Pb/^{206}Pb$) of melt inclusions from three Polynesian lavas, which were shown to span 50% of the variation in Pb composition in worldwide OIBs. Subsequent studies analyzed melt inclusions from ocean island and subduction-related settings, revealing increased isotope variability compared to the host lava compositions (e.g., Yurimoto et al., 2004; Maclennan, 2008;

Rose-Koga et al., 2012; Schiavi et al., 2015; Nikogosian et al., 2016; Rose-Koga et al., 2017). In situ techniques were further developed for Sr isotopes in melt inclusions by LA-multicollector (MC)-ICP-MS (Jackson et al., 2006), and a subsequent paper by Sobolev et al. (2011) reported combined Sr-Pb isotope data obtained by laser ablation. These studies have highlighted the strength of using radiogenic isotopes in individual melt inclusions to study mantle heterogeneity and reveal processes unrecognized in bulk lavas. In 2009, the first Sr isotope data obtained from combined wet chemistry and TIMS analysis were reported for olivine-hosted melt inclusions from Iceland (Harlou et al., 2009). This approach allows interference-free isotope measurements, and hence yields a significant improvement in precision compared to in situ measurements. The authors evaluated the use of micro-milling and show that entrainment of a small amount of host olivine alongside the inclusion has a negligible effect on the measured isotope composition. It was, however, not until after 2015 that the analytical capabilities were optimized for combined measurement of $^{87}Sr/^{86}Sr$ and $^{143}Nd/^{144}Nd$ ratios in olivine-hosted melt inclusions by TIMS (Koornneef et al., 2015; Reinhard et al., 2018) and, ultimately, combined analyses of Sr, Nd and Pb isotopes including $^{208}Pb/^{204}Pb$ and $^{207}Pb/^{204}Pb$ ratios on individual inclusions (Koornneef et al., 2019). The optimizations included development of miniaturized, ultra-low blank chemical separation procedures combined with analytical techniques that use more sensitive amplifiers in the Faraday detection system of the TIMS (Koornneef et al., 2014). Use of these amplifiers, equipped with 10^{13} Ω resistors in their feedback loop, results in 10-fold increase in precision when analyzing sub-nanogram samples at low ion currents ($<2\times10^{-13}$ A). The techniques allow precise and accurate analyses of Sr-Nd-Pb isotope ratios in individual melt inclusions, provided they contain >1 ng Sr, >30 pg Nd and >200 pg Pb. The capability of MC-ICP-MS for the determination of radiogenic isotopes in melt inclusions (>1 ng Sr, >0.5 ng Nd) has also been demonstrated recently (Genske et al., 2019, Stracke et al., 2019). Current developments include optimizations to the ion-exchange chromatography procedure in order to yield residual matrix fractions that can be analyzed for trace element ratios by conventional ICP-MS methods (Bracco Gartner et al., 2019).

Recent isotopic studies on olivine-hosted melt inclusions have revealed a previously-unrecognized recycled component in the subduction-related mantle source below Italy

(Koornneef et al., 2019), as well as ubiquitous ultra-depleted domains in the source of mid-ocean ridge basalts (Stracke et al., 2019). The analytical developments open up new research directions that include intra-oceanic subduction zones, intraplate and mid-ocean ridge settings, and will likely lead to significant advances in our understanding of the processes that create isotopic variability in mantle-derived melts.

Best practice for analysis of radiogenic isotopes (TIMS / MC-ICP-MS):

Type of data produced:

Isotope ratios (i.e. radiogenic isotope over stable isotope of an element). Multiple isotope systems (e.g. Sr, Nd, Pb) can be analyzed in a single sample.

Sample requirements:

Melt inclusions should be selected so that the amount of the element of interest is sufficient with respect to potential blank contributions. The inclusion-bearing grain should be prepared so that the inclusion is effectively isolated (i.e. external contributions are negligible); this may necessitate micro-drilling or -milling to remove unwanted parts of the host grain, as well as leaching of the host grain to remove any adhering phases. Wet chemistry techniques (sample digestion) and ion-exchange chromatography are employed to isolate the element(s) of interest. These steps require ultra-pure reagents and minimal handling steps to minimize blank contributions. Representative aliquots of reference materials (closely matching the unknown samples) should be included throughout the procedure. Blanks should be actively monitored and cover the total procedure. If blank corrections are to be made, it is imperative to evaluate individual blank contributions, e.g. from sample preparation, reagents, ion-exchange chromatography, loading on TIMS filament, and their representativeness.

Analytical conditions:

Analyses are typically performed by TIMS or MC-ICP-MS equipped with 10^{11} Ω (for Sr and spiked-Pb fractions) and a mix of 10^{11} and 10^{13} Ω (for Nd and natural-Pb fractions) resistors in the feedback loop of Faraday cup amplifiers. Samples are generally run to exhaustion, ideally at the highest signal intensity for an acceptable number of analytical cycles. Cup configurations should be set so that any potential interfering isotopes are monitored. Standard reference materials (e.g. NIST SRM 987 for Sr) are used to monitor the repeatability and intermediate precision of measurements. For Sr and Nd, isotopic measurements can be corrected internally for instrumental mass fractionation. Double spike inversion for Pb analyses is performed offline, using publicly-available data reduction programs.

Analytical details:

Multiple inclusions in a single grain (e.g. MIA) or compositionally-similar inclusions/grains may be pooled to attain enough element of interest and/or the desired analytical precision.

Total procedural blanks can be corrected for using elemental abundances determined through isotope dilution by means of single (Sr and Nd) and double spike techniques (Pb).

Isotope ratios can be corrected for radioactive ingrowth of daughter isotopes over time by conventional age corrections.

Reporting requirements:

Report the manufacturer and model of the analytical instrument used.

Report reference materials used and analytical conditions for each isotope system analyzed (cup configuration, average signal intensity for each isotope, number of analytical cycles, propagated uncertainties).

Report the repeatability and intermediate precision of measurements on standard reference materials. It is advised to avoid usage of terms not defined by ISO (e.g. "external precision").

Report the size and shape of each inclusion analyzed and include a photomicrograph of each in supplementary data. Photomicrographs are ideally taken after micro-sampling and/or grain leaching, but should otherwise clearly indicate that part of the sample that was analyzed.

Report the elemental contributions for analyses that include inclusion and (part of the) host grain, ideally quantified using reported volume, density and elemental concentrations in both phases.

If an age correction was applied, report analyzed isotope ratios, calculated initial ratios and employed decay constants.

Conclusions

The study of melt inclusions has evolved over the past 2-3 decades to become a mature and commonly used method to characterize a wide variety of igneous and volcanic processes. However, to date there has not been a concerted effort to develop a set of guidelines to assist the beginning, and even experienced, researcher on the proper protocols to follow. As a community effort to constructively develop guidelines for the documentation, collection and reporting of data from melt inclusion studies, we provide recommendations to all scientists studying melt inclusions in an effort to systematize data collection and reporting to facilitate comparison and evaluation of reported melt inclusion

data. We are aware that these guidelines increase the amount of information that must be reported and will lead to an increase in the amount of text and images required, and this additional information can be provided mainly in the supplementary material of the publication. We encourage reviewers to request that images of melt inclusions be included, that raw data not be normalized to 100, and that analytical details for each method be described in detail. We also encourage journal editors to accept the consequent size of supplementary material that will be submitted in support of the conclusions and results presented in manuscripts. Data should also be added to various online databases, such as EarthChem (http://www.earthchem.org/portal) or Georock (http://georoc.mpch-mainz.gwdg.de/georoc/) for chemistry data or Puli for IR spectra (http://www.puli.mfgi.hu/).

Acknowledgements: The organizers thank WHOI for the rooms and catering during the workshop. ER-K and A-SB thank CAMECA-AMETEK for their sponsorship during the organization of the “2018 Melt Inclusion Workshop”. ER-K acknowledges the financial support from Region Auvergne-Rhône-Alpes (program SCUSI) and the Laboratory of Excellence ClerVolc, that allowed several PhD, post-docs and permanent scientists of Laboratoire Magmas et Volcans to travel to Woods Hole for the Workshop. This is Laboratory of Excellence ClerVolc contribution no xxx.

Figure caption:

Fig. 1: (A) picture of two glassy olivine-hosted melt inclusions from the Ambae volcano. Inside both inclusions, we can see the very circular bubble and the squarish spinel. (B) Sometimes the adopt the faceted crystal shape of the host mineral giving the inclusion this "raisin" aspect. (C) BSE image of a crystallized inclusions with dendritic microcrystals (m), several small bubbles (b) and a glassy matrix, (D) picture in transmitted light of a devitrified melt inclusion from Pan de Azucar volcano (pictures B, C and D from Le Voyer, PhD 2009).

Fig. 2: Evolution of trace elements contents during PEC. a-b) present the evolution of the melt inclusion content (Cl) relative to initial content (C_0) for elements with various partition coefficients. In c-e) the variation is presented in percent of variation relative to C_0. In a-b) both equilibration crystallization (solid lines), and fractional crystallization (dashed lines) models are presented for theoretical elements with various partition coefficients (from D= 0 to D=100). In c-e) an equilibrium crystallization model is used, and specific elements are considered for PEC of melt inclusions in olivine (c), plagioclase (d), and clinopyroxene (e). Considered partition coefficients are presented between brackets for each element, and are from Laubier et al. (2014) for all elements except Ce in olivine from Sun and Liang (2013), and Cr in clinopyroxene from Bacon and Druitt (1988). Eu partition coefficient value is for redox conditions buffered with NNO.

Fig. 3: Idealized flow-chart for melt inclusion (MI) sample analyses given sample preparation and analysis-induced damage considerations. Depending on the intended research, particular steps may be skipped. Samples can be re-polished to remove upper surfaces that were damaged by various techniques (EPMA, SIMS, LA-ICPMS). See text for references and for more details on preparation and best practices for MI sample selection, MI homogenization, each for analytical technique. Melt inclusions in inset photos are from Kīlauea Volcano's 2018 Lower East Rift Zone eruption.

Fig. 4 : Raman spectra after frequency-temperature correction (a) of the aluminosilicate framework vibration range and (b) of the OH-stretching range ("water band").

Fig. 5: H_2O and CO_2 absorption bands in FTIR spectra of hydrous rhyolitic (top) and basanitic (bottom) melt inclusions. In the rhyolite spectrum, the 5200 cm^{-1} (molecular H_2O) and 4500 cm^{-1} (OH) bands can be seen, but the mid-IR fundamental OH stretching band (3550 cm^{-1}), which gives total H_2O, is oversaturated. The 2350 cm^{-1} band (molecular CO_2) can also be seen. In the basanite spectrum, total H_2O is much lower and therefore can been seen at 3550 cm^{-1}. The doublet at 1515 and 1430 cm^{-1} is for dissolved carbonate, which is the primary solution mechanism for CO_2 in mafic compositions. Data are from Roberge et al. (2013) and Rasmussen et al. (2017).

Fig. 6A-C: A. Edge-step normalised XANES spectra of the Smithsonian basaltic standard glasses. Inset shows show spectra over the pre-edge region energy range (data from Moussallam et al., 2016). B. Calibration curve for the centroid position (blue) and peak height ratio (red) determined by XANES compared with the $Fe^{3+}/\sum Fe$ ratios of the Smithsonian basaltic standard glasses determined by Mössbauer spectroscopy (data from

Moussallam et al., 2019a). C. Time series of normalised fluoresced intensity (FF) over I0 at 7114.3 eV integrated over 1 s intervals for a hydrated (5.2 wt.% H_2O) basalt under three different beam attenuation conditions. A fresh spot was illuminated with a 2.5×1.2 µm beam for each analysis. Note that while photo-oxidation can clearly be seen with no beam attenuation and with an attenuation down to about 16% of the original beam flux (using a 0.1 mm Al foil), no photo-oxidation can be detected once the beam has been attenuated down to 1% of its original flux (using a 0.25 mm Al foil; data from Moussallam et al., 2019a)

Fig. 7: Example of chlorine isotopes measurements by SIMS (not corrected for IMF) over a day. Round symbols represent different in-house standards, square symbols are for the melt inclusions samples from Aoba (Vanuatu) and Vulcano (Italy) volcanoes. Data are from Manzini et al. (2017).

Fig. 8: Log-Log plot of concentrations of F (**a**), S (**b**), and Cl (**c**) measured by SIMS vs. that measured by EPMA (circles). Standards are categorized according to their SiO_2 contents into mafic, intermediate, and acidic. The solid line is a one-to-one slope indicating the coherence of the fit.

References

Agrinier P., Jendrzejewski N. (2000) Overcoming problems of density and thickness measurements in FTIR volatile determinations: a spectroscopic approach. *Contributions to Mineralogy and Petrology*, **139**, 265-272, https://doi.org/10.1007/s004100000141

Anderson, A.T., Newman, S., Wiliams, S.N., Druitt, T.H., Skirius, C. and Stolper, E. (1989) H_2O, CO_2, Cl and gas in Plinian and ash flow Bishop rhyolite. *Geology*, **17**, 221-225.

Anderson, A.T. and Brown, G.G. (1993) CO2 contents and formation pressures of some Kilauean melt inclusions. *American Mineralogist*, **78**, 794-803.

Anderson AT, Davis AM, Lu F (2000) Evolution of Bishop Tuff rhyolitic magma based on melt and magnetite inclusions and zoned phenocrysts. *Journal of Petrology*, **41**, 449-473.

Aster, E.M., Wallace, P.J., Moore, L.R., Watkins, J., Gazel, E., Bodnar, R.J. (2016) Reconstructing CO2 concentrations in basaltic melt inclusions using Raman analysis of vapor bubbles. *Journal of Volcanology and Geothermal Resources*, **323**, 148-162.

Bacon, C.R. and Druitt, T.H. (1988). Compositional Evolution of the Zoned Calcalkaline Magma Chamber of Mount-Mazama, Crater Lake, Oregon. *Contributions to Mineralogy and Petrology* **98**: 224-256.

Barth, A., Newcombe, M., Plank, T., Gonnermann, H., Hajimirza, S., Soto, G.J., Saballos, A., and Hauri, E.H. (2019) Magma decompression rate correlates with explosivity at basaltic volcanoes — Constraints from water diffusion in olivine, *Journal of Volcanology and Geothermal Research* **387**, p. 106664

Bartoli, O., Cesare, B., Poli, S., Bodnar. R. J., Acosta-Vigil, A., Frezzotti, M. L. & Meli, S. (2013) Uncovering the composition of melt and fluid regime at the onset of crustal anatexis and S-type granite formation. *Geology*, **41**, 115-118.

Beddoe-Stephens B, Aspden JA, Shepherd TJ (1988) Glass inclusions and melt compositions of the Toba Tuffs, Northern Sumatra. Contributions to Mineralogy and Petrology, 83, 278-287

Befus K. S., Gardner J. E., Zinke R. W. (2012) Analyzing water contents in unexposed glass inclusions in quartz crystals. American Mineralogist, 97, 1898-1904, https://doi.org/10.2138/am.2012.4206

Berkesi, M., Hidas, K., Guzmics, T., Dubessy, J., Bodnar, R. J., Szabó, Cs., Vajna, B. & Tsunogae, T. (2009) Detection of small amounts of H_2O in CO_2-rich fluid inclusions using Raman spectroscopy. Journal of Raman Spectroscopy, **40**, 1461-1463; http://10.1002/jrs.2440

Berry, A. J., O'Neill, H. S. C., Jayasuriya, K. D., Campbell, S. J. & Foran, G. J. (2003). XANES calibrations for the oxidation state of iron in a silicate glass. *American Mineralogist* **88**, 967–977.

Berry, A. J., Stewart, G. A., O'Neill, H. S. C., Mallmann, G. & Mosselmans, J. F. W. (2018). A re-assessment of the oxidation state of iron in MORB glasses. *Earth and Planetary Science Letters* **483**, 114–123.

Bodnar, R. J. & Student, J. J. (2006) Melt inclusions in plutonic rocks: Petrography and microthermometry. *In* Melt Inclusions in Plutonic Rocks (J. D. Webster, *ed.*) Mineral. Assoc. Canada, Short Course **36**, 1-26.

Botcharnikov, R. E., Koepke, J., Holtz, F., McCammon, C. & Wilke, M. (2005). The effect of water activity on the oxidation and structural state of Fe in a ferro-basaltic melt. *Geochimica et Cosmochimica Acta* **69**, 5071–5085.

Bouvier, A.S., Métrich, N., and Deloule, E. (2008) Slab-Derived Fluids in the Magma Sources of St. Vincent (Lesser Antilles Arc): Volatile and Light Element Imprints: *Journal of Petrology*, **49**, 1427–1448, doi: 10.1093/petrology/egn031.

Bouvier, A.-S., Manzini, M., Rose-Koga, E.F., Nichols, A.R.L., and Baumgartner, L.P. (2019) Tracing of Cl input into the sub-arc mantle through the combined analysis of B, O and Cl isotopes in melt inclusions : *Earth and Planetary Science Letters*, **507**, 30–39, doi: 10.1016/j.epsl.2018.11.036.

Bracco Gartner, A.J.J., Nikogosian, I.K., Luciani, N., Davies, G.R., and Koornneef, J.M. (2019). Coupled Sr-Nd-Pb isotope and trace element ratios in olivine-hosted melt inclusions from subduction-related magmatism in central Italy. Acta Mineralogica-Petrographica Abstract Series 10, 21.

Bucholz, C.E., Gaetani, G.A., and Behn, M.D. (2013) Post-entrapment modification of volatiles and oxygen fugacity in olivine-hosted melt inclusions: *Earth and Planetary Science Letters*, **374**, 145–155.

Burke, E. A.J. (2001) Raman microspectrometry of fluid inclusions. *Lithos*, **55**, 139-158.

Burnham, A.D., Berry, A.J., Wood, B.J., and Cibin, G. (2010) Chemical Geology: *Chemical Geology*, **330-331**, 228–232, doi: 10.1016/j.chemgeo.2012.09.002.

Burnham, A.D., and Berry, A.J. (2014) The effect of oxygen fugacity, melt composition, temperature and pressure on the oxidation state of cerium in silicate melts: *Chemical Geology,* **366**, 52–60, doi: 10.1016/j.chemgeo.2013.12.015.

Cabral, R.A., Jackson, M.G., Rose-Koga, E.F., Koga, K.T., Whitehouse, M.J., Antonelli, M.A., Farquhar, J., Day, J.M.D., and Hauri, E.H. (2013) Anomalous sulphur isotopes in plume lavas reveal deep mantle storage of Archaean crust: *Nature*, **496**, 490–493, doi: 10.1038/nature12020.

Cadoux, A., Iacono-Marziano, G., Paonita, A., Deloule, E., Aiuppa, A., Nelson Eby, G., Costa, M., Brusca, L., Berlo, K., Geraki, K., Mather, T.A., Pyle, D.M., and Di Carlo, I., (2017) A new set of standards for in – situ measurement of bromine abundances in

natural silicate glasses: Application to SR-XRF, LA-ICP-MS and SIMS techniques: Chemical *Geology*, **452**, 60–70, doi: 10.1016/j.chemgeo.2017.01.012.

Cannatelli, C., Doherty, A.L., Esposito, R., Lima, A., and De Vivo, B. (2016) Understanding a volcano through a droplet: a melt inclusion approach. *Journal of Geochemical Exploration*, **171**, 4-19.

Carroll, M., and Rutherford, M.J., 1988, Sulfur speciation in hydrous experimental glasses of varying oxidation state--results from measured wavelength shifts of sulfur X-rays: *American Mineralogist*, **73**, 845–849.

Chabiron, A., Pironon, J., and Massare, D., 2004, Characterization of water in synthetic rhyolitic glasses and natural melt inclusions by Raman spectroscopy: *Contributions to Mineralogy and Petrology*, **146**, 485–492, doi: 10.1007/s00410-003-0510-x.

Chaigneau M, Massare D, Clocchiatti R (1980) Contribution a l'etude des inclusions vitreuses et des elements volatils contenus dans la phenocristaux de quartz de roches volcaniques acides. *Bulletin Volcanologique*, **43**, 233-240.

Chaussidon, M., Robert, F., Mangin, D., Hanon, P., and Rose, E.F. (1997) Analytical procedures for the measurement of boron isotope compositions by ion microprobe in meteorites and mantle rocks: *Geostandards Newsletter*, **21**, 7–17.

Chen, Y., Provost, A., Schiano, P., and Cluzel, N. (2011) The rate of water loss from olivine-hosted melt inclusions: *Contributions to Mineralogy and Petrology*, **162**, 625–636, doi: 10.1007/s00410-011-0616-5.

Chen, Y., Provost, A., Schiano, P., and Cluzel, N. (2013) Magma ascent rate and initial water concentration inferred from diffusive water loss from olivine-hosted melt inclusions: *Contributions to Mineralogy and Petrology*, **165**, 525–541, doi: 10.1007/s00410-012-0821-x.

Cherniak, D.J. (2010) REE diffusion in olivine: *American Mineralogist*, **95**, 362–368, doi: 10.2138/am.2010.3345.

Cottrell, E., Kelley, K. A., Lanzirotti, A. & Fischer, R. A. (2009). High-precision determination of iron oxidation state in silicate glasses using XANES. *Chemical Geology* **268**, 167–179.

Cottrell, E. & Kelley, K. A. (2011). The oxidation state of Fe in MORB glasses and the oxygen fugacity of the upper mantle. *Earth and Planetary Science Letters* **305**, 270–282.

Cottrell, E. & Kelley, K. A. (2013). Redox Heterogeneity in Mid-Ocean Ridge Basalts as a Function of Mantle Source. *Science* **340**, 1314–1317.

Cottrell, E., Lanzirotti, A., Mysen, B., Birner, S., Kelley, K. A., Botcharnikov, R., Davis, F. A. & Newville, M. (2018) A Mössbauer-based XANES calibration for hydrous basalt glasses reveals radiation-induced oxidation of Fe. *American Mineralogist* **103**, 489–501.

Créon, L., Levresse, G., Remusat, L., Bureau, H., and Carrasco-Núñez, G. (2018) *Chemical Geology*, **483**, 162–173, doi: 10.1016/j.chemgeo.2018.02.038.

Danyushevsky, L., Della-Pasqua, F., and Sokolov, S. (2000) Re-equilibration of melt inclusions trapped by magnesian olivine phenocrysts from subduction-related magmas: petrological implications: *Contributions to Mineralogy and Petrology*, **138**, 68–83.

Danyushevsky, L. V., Sokolov, S. & Falloon, T. J. (2002a). Melt inclusions in olivine phenocrysts: using diffusive re-equilibration to determine the cooling history of a crystal, with implications for the origin of olivine-phyric volcanic rocks. *Journal of Petrology* **43**, 1651–1671.

Danyushevsky, L. V., McNeill, A. W. & Sobolev, A. V. (2002b). Experimental and petrological studies of melt inclusions in phenocrysts from mantle-derived magmas: an overview of techni- ques, advantages and complications. *Chemical Geology* **183**, 5–24.

Danyushevsky, L.V., and Plechov, P. (2011) Petrolog3: Integrated software for modeling crystallization processes: *Geochemistry Geophysics Geosystems*, **12**, doi: 10.1016/0098-3004(90)90074-4.

Dauphas, N., Roskosz, M., Alp, E.E., Neuville, D.R., Hu, M.Y., Sio, C.K., Tissot, F.L.H., Zhao, J., Tissandier, L., Medard, E., and Cordier, C. (2014) Magma redox and structural controls on iron isotope variations in Earth's mantle and crust: *Earth and Planetary Science Letters*, **398**, 127–140, doi: 10.1016/j.epsl.2014.04.033.

Deer WA, Howie RA, Zussman J (1997) Rock-forming minerals. Geological Society, London.

Delhaye, M. & Dhamelincourt, P. (1975) Raman microprobe and microscope with laser excitation. *Journal of Raman Spectroscopy*, **3**, 33–43.

Devine, J., Gardner, J.E., Brack, H.P., Layne, G.D. and Rutherford, M.J. (1995) Comparison of microanalytical methods for estimating H_20 contents of silicic volcanic glasses, *American Mineralogist*, **80**, 319-328.

Dhamelincourt, P., Bény, J.-M., Dubessy, J. & Poty, B. (1979) Analyse d'inclusions fluides à la microsonde MOLE à effet Raman. *Bulletin de Minéralogie*, **102**, 600–610 [in French].

Di Genova, D. Kolzenburg, S. Wiesmaier, S., Dallanave, E., Neuville, D.R., Hess, K.-U., Dingwell, D.B. (2017) A chemical tipping point governing mobilization and eruption style of rhyolitic magma. *Nature*, **552**, 235-238https://doi.org/10.1038/nature24488.

Di Genova, D., Caracciolo, A., Kolzenburg, S. (2018) Measuring the degree of "nanotilization" of volcanic glasses: Understanding syn-eruptive processes recorded in melt inclusions. *Lithos*, **318–319**, 209-218.

Donovan, J.J., and Tingle, T.N. (1996) An improved mean atomic number background correction for quantitative microanalysis: *JMSA*, **2**, 1–7.

Drignon, M. J., Nielsen, R. L., Tepley, F. J., III & Bodnar, R. J. (2019a) Upper mantle origin of plagioclase megacrysts from plagioclase ultraphyric MORB. *Geology*, **47**(1), 43-46. https://doi.org/10.1130/G45542.1

Drignon, M. J., Nielsen, R. L., Tepley, F. J., III & Bodnar, R. J. (2019b) Re-equilibration processes occurring in plagioclase-hosted melt inclusions from plagioclase ultraphyric basalts. *Geochemistry, Geophysics, Geosystems (G-cubed)*, **20** (1), 109-119. https://doi.org/10.1029/2018GC007795

Esposito, R., Bodnar, R. J., De Vivo, B., Lima, A., Fedele, L., Shimizu, N. & Belkin, H. (2008) Volatiles in the magma associated with the Solchiaro eruption in the Phlegrean Volcanic District (Italy). *Eos Trans. AGU*, **89**(52), Fall Meet. Suppl., Abstract V21A-2079.

Esposito, R., Bodnar, R. J., Danyushevsky, L. V., De Vivo, B., Fedele, L., Hunter, J., Lima, A. & Shimizu, N. (2011) Volatile evolution of magma associated with the

Solchiaro eruption in the Phlegrean Volcanic District (Italy). *Journal of Petrology*, **52**, 2431-2460. http://dx.doi.org/10.1093/petrology/egr051

Esposito, R., Lamadrid, H.M., Redi, D., Steele-MacInnis, M., Bodnar, R.J., Manning, C.E., De Vivo, B., Cannatelli, C., Lima, A. (2016) Detection of liquid H_2O in vapor bubbles in reheated melt inclusions: Implications for magmatic fluid composition and volatile budgets of magmas? *American Mineralogist*, **101**, 1691-1695.

Farges, F., Lefrère, Y., Rossano, S., Berthereau, A., Calas, G. & Brown, G. E. (2004). The effect of redox state on the local structural environment of iron in silicate glasses: a combined XAFS spectroscopy, molecular dynamics, and bond valence study. *Journal of Non-Crystalline Solids* **344**, 176–188.

Ferriss, E., Plank, T., Newcombe, M., Walker, D., Hauri, E. (2018) Rates of dehydration of olivines from San Carlos and Kilauea Iki, *Geochimica et Cosmochimica Acta* **242**, 165-190.

Fialin, M., Wagner, C., Métrich, N., Humler, E., Galoisy, L., and Bézos, A. (2001) Fe3+/ΣFe vs. FeLα peak energy for minerals and glasses: Recent advances with the electron microprobe : *American Mineralogist*, **86**, 456–465.

Fialin, M., Bézos, A., Wagner, C., Magnien, V., and Humler, E. (2004) Quantitative electron microprobe analysis of Fe3+/Fetot : basic concepts and experimental protocol for glasses: *American Mineralogist*, **89**, 654–662.

Fialin, M., and Wagner, C. (2012) Redox kinetics of iron in alkali silicate glasses exposed to ionizing beams: Examples with the electron microprobe, Journal of Non-Crystalline Solids: *Journal of non-crystalline solids*, **358**, 1617–1623, doi: 10.1016/j.jnoncrysol.2012.04.026.

Fiege, A., Ruprecht, P., Simon, A.C., Bell, A.S., Göttlicher, J., Newville, M., Lanzirotti, T., and Moore, G. (2017) Calibration of Fe XANES for high-precision determination of Fe oxidation state in glasses: Comparison of new and existing results obtained at different synchrotron radiation sources: American Mineralogist, v. 102, no. 2, p. 369–380, doi: 10.2138/am-2017-5822.

Florentin, L., Deloule, E., Faure, F., and Mangin, D. (2018) Chemical 3D-imaging of glass inclusions from allende (CV3) olivine via SIMS: A new insight on

chondruleformation conditions: *Geochimica et Cosmochimica Acta*, **230**, 83–93, doi: 10.1016/j.gca.2018.03.021.

Ford CE, Russell DG, Craven JA, Fisk MR (1983) Olivine–liquid equilibria: temperature, pressure and composition dependence of the crystal/liquid cation partition coefficients for Mg, Fe2+, Ca and Mn. J Petrol 24:256–265.

Frezzotti, M. L., Tecce, F. & Casagli, A. (2012) Raman spectroscopy for fluid inclusion analysis. *Journal of Geochemical Exploration*, **112**, 1-20, 10.1016/j.gexplo.2011.09.009

Gaetani, G.A., and Watson, E.B. (2000) Open system behavior of olivine-hosted melt inclusions: Earth and Planetary Science Letters, v. 183, no. 1, p. 27–41.

Gaetani, G.A., O'Leary, J.A., Shimizu, N., Bucholz, C.E., and Newville, M. (2012) Rapid reequilibration of H_2O and oxygen fugacity in olivine-hosted melt inclusions: Geology, 40, 915–918, doi: 10.1130/G32992.1.

Gaetani, G.A., O'Leary, J.A., Koga, K.T., Hauri, E.H., Rose-Koga, E.F., and Monteleone, B.D. (2014) Hydration of mantle olivine under variable water and oxygen fugacity conditions: *Contributions to Mineralogy and Petrology, 167*, 965–14, doi: 10.1007/s00410-014-0965-y.

Genske F., Stracke A., Berndt J., and Klemme S. (2019). Process-related isotope variability in oceanic basalts revealed by high-precision Sr isotope ratios in olivine-hosted melt inclusions. *Chemical Geology*, **524**, 1-10. doi: 10.1016/j.chemgeo.2019.04.031.

Goncalves Feierra, P., de Ligny D., Lazzari, O., Jean, A., Cinotora Gonzalez, O., Neauville, D.R. (2013) Photoreduction of iron by a synchrotron X-ray beam in low iron content soda-lime silicate glasses*: Chemical Geology*, **346**, 106–112.

Gualda GAR, Pamukcu AS, Ghiorso MS, Anderson AT, Sutton SR, Rivers ML (2012) Timescales of quartz crystallization and the longevity of the Bishop giant magma body. *PLoS ONE*, **7**, e37492.

Guzmics, T., Berkesi, M., Bodnar, R.J., Fall, A., Bali, E., Milke, R., Vetlényi, E., and Szabó, C. (2019) Natrocarbonatites: A hidden product of three-phase immiscibility: *Geology*, **47**, 527–530, doi: 10.1016/j.lithos.2006.03.018.

Halter, W.E., Pettke, T., Heinrich, C.A., and Rothen-Rutishauser, B. (2002) Major to trace element analysis of melt inclusions by laser-ablation ICP-MS: methods of quantification: *Chemical Geology*, **183**, 63–86.

Harlou, R., Pearson, D.G., Nowell, G.M., Ottley, C.J., and Davidson, J.P. (2009) Chemical Geology: *Chemical Geology*, **260**, 254–268, doi: 10.1016/j.chemgeo.2008.12.020.

Hartley, M.E., Thordarson, T., Taylor, C., Fitton, J.G., EIMF (2012) Evaluation of the effects of composition on instrumental mass fractionation during SIMS oxygen isotope analyses of glasses: *Chemical Geology*, **334**, 312–323, doi: 10.1016/j.chemgeo.2012.10.027.

Hartley, M.E., Maclennan, J., Edmonds, M., and Thordarson, T. (2014) Reconstructing the deep CO2 degassing behavior of large basaltic fissure eruptions. *Earth and Planetary Science Letters*, **393**, 120-121.

Hartley, M. E., Shorttle, O., Maclennan, J., Moussallam, Y. & Edmonds, M. (2017). Olivine-hosted melt inclusions as an archive of redox heterogeneity in magmatic systems. *Earth and Planetary Science Letters* **479**, 192–205.

Hauri, E.H., Wang, J., Dixon, J.E., King, P.L., Mandeville, C. and Newman, S. (2002a) SIMS investigations of volatiles in volcanic glasses, 1. Calibration, sensitivity and comparisons with FTIR. *Chem. Geol.* **183**, 99–114.

Hauri, E.H. (2002b) SIMS investigations of volatiles in volcanic glasses, 2. Isotopes and abundances in Hawaiian melt inclusions. *Chem. Geol.* **183**, 115–141.

Hauri, E.H., Weinreich, T., Saal, A.E., Rutherford, M.C., and Van Orman, J.A. (2011) High Pre-Eruptive Water Contents Preserved in Lunar Melt Inclusions: *Science*, **333**, 213–215, doi: 10.1126/science.1204626.

Hervig R. L., Mazab F. K., Moore G., McMillan P. F. (2003) Analyzing hydrogen (H_2O) in silicate glass by secondary ion mass spectrometry and reflectance Fourier transform infrared spectroscopy. *Developements in Volcanology,* **5**, 83-103, https://doi.org/10.1016/S1871-644X(03)80025-6

Hughes, E.C., Ben Buse, Kearns, S.L., Blundy, J.D., Kilgour, G., and Mader, H.M. (2019) Low analytical totals in EPMA of hydrous silicate glass due to sub-surface T

charging: Obtaining accurate volatiles by difference, *Chemical Geology*, **505**, 48–56, doi: 10.1016/j.chemgeo.2018.11.015.

Humphreys, M.C.S., Kearns, S.L., and Blundy, J.D. (2006) SIMS investigation of electron-beam damage to hydrous, rhyolitic glasses: Implications for melt inclusion analysis: *American Mineralogist*, **91**, 667–679, doi: 10.2138/am.2006.1936.

Jackson, M.G. and S.R. Hart, (2006) Strontium isotopes in melt inclusions from Samoan basalts: Implications for heterogeneity in the Samoan plume. *Earth and Planetary Science Letters*. **245**(1-2): p. 260-277.

Jarosewich, E., Parkes, A. S. and Wiggins, L. B. (1979) Microprobe Analysis of Four Natural Glasses and One Mineral: An Interlab- oratory Study of Precision and Accuracy, *Smithsonian Contrib. Earth Sci.* **22**, 53-67.

Jenner, F.E., and O'Neill, H.S.C. (2012) Analysis of 60 elements in 616 ocean floor basaltic glasses: *Geochemistry Geophysics Geosystems*, **13**, doi: 10.1029/2003GC000597.

Jugo, P.J., Wilke, M., and Botcharnikov, R.E. (2010) Sulfur K-edge XANES analysis of natural and synthetic basaltic glasses: Implications for S speciation and S content as function of oxygen fugacity: *Geochimica et Cosmochimica Acta*, **74**, 5926-5938.

Kamenetsky, V.S., Davidson, P., Mernagh, T.P., Crawford, A.J., Gemmell, J.B., Portnyagin, M.V., and Shinjo, R. (2002) Fluid bubbles in melt inclusions and pillow-rim glasses: high-temperature precursors to hydrothermal fluids?: *Chemical Geology*, **183**, 349-364.

Kamenetsky, V.S. and Kamenetsky, M.B. (2010) Magmatic fluids immiscible with silicate melts: examples from inclusions in phenocrysts and glasses, and implications for magma evolution and metal transport. *Geofluids*, **10**, 293-311.

Kelley, K.A., Plank, T., Ludden, J., and Staudigel, H. (2003) Composition of altered oceanic crust at ODP Sites 801 and 1149: *Geochemistry Geophysics Geosystems*, **4**, doi: 10.1016/0012-821X(94)00263-X.

Kelley, K.A., and Cottrell, E. (2012) The influence of magmatic differentiation on the oxidation state of Fe in a basaltic arc magma, *Earth and Planetary Science Letters*, **329-330**, 109–121, doi: 10.1016/j.epsl.2012.02.010.

King P. L., Larsen J. F. (2013) A micro-reflectance IR spectroscopy method for analyzing volatile species in basaltic, andesitic, phonolitic, and rhyolitic glasses. *American Mineralogist*, **98**, 1162-1171, https://doi.org/10.2138/am.2013.4277

Klimm, K., Kohn, S. C., O'Dell, L. A., Botcharnikov, R. E. & Smith, M. E. (2012). The dissolution mechanism of sulphur in hydrous silicate melts. I: Assessment of analytical techniques in determining the sulphur speciation in iron-free to iron-poor glasses. *Chemical Geology* **322–323**, 237–249.

Knipping, J. L., Behrens, H., Wilke, M., Göttlicher, J. & Stabile, P. (2015). Effect of oxygen fugacity on the coordination and oxidation state of iron in alkali bearing silicate melts. *Chemical Geology* **411**, 143–154.

Kobayashi, K., Tanaka, R., Moriguti, T., Shimizu, K. and Nakamura, E. (2004) Lithium, boron, and lead isotope systematics of glass inclusions in olivines from Hawaiian lavas: evidence for recycled components in the Hawaiian plume. *Chem. Geol.* **212**, 143–161.

Koga, K.T., Hauri, E.H., Hirschmann, M.M., and Bell, D.R. (2003) Hydrogen concentration analyses using SIMS and FTIR: Comparison and calibration for nominally anhydrous minerals: *Geochemistry Geophysics Geosystems*, **4**, doi: 10.1029/2002GC000378.

Koornneef, J.M., Bouman, C., Schwieters, J.B., and Davies, G.R. (2014) Measurement of small ion beams by thermal ionisation mass spectrometry using new 10^{13} Ohm resistors: *Analytica Chimica Acta*, 49–55, doi: 10.1016/j.aca.2014.02.007.

Koornneef, J.M., Nikogosian, I., Van Bergen, M.J., Smeets, R., Bouman, C., and Davies, G.R. (2015) TIMS analysis of Sr and Nd isotopes in melt inclusions from Italian potassium-rich lavas using prototype 10^{13} Ω amplifiers. *Chemical Geology*, 2015. **397**: p. 14-23, doi: 10.1016/j.chemgeo.2015.01.005.

Koornneef, J.M., Nikogosian, I., Bergen, M.J., Vroon, P.Z., and Davies, G.R. (2019) Ancient recycled lower crust in the mantle source of recent Italian magmatism: *Nature Communications*, 1–10, doi: 10.1038/s41467-019-11072-5.

Kress, V.C., and Carmichael, I.S.E. (1991) The compressibility of silicate liquids containing Fe2O3 and the effect of composition, temperature, oxygen fugacity and

pressure on their redox states: *Contributions to Mineralogy and Petrology*, **108**, 82–92, doi: 10.1007/BF00307328.

Lamadrid, H. M., Lamb, W. M., Santosh, M. & Bodnar, R. J. (2014) Raman spectroscopic characterization of H_2O in CO_2-rich fluid inclusions in granulite facies metamorphic rocks. Gondwana Research **26**, 301-310, http://dx.doi.org/10.1016/j.gr.2013.07.003

Lamadrid, H. M., Moore, L., Moncada, D., Rimstidt, J. D., Burruss, R. C. & Bodnar, R. J. (2017) Reassessment of the Raman CO_2 densimeter. Chemical Geology, **450**, 210-222. http://dx.doi.org/10.1016/j.chemgeo.2016.12.034

Lange R. A. (1997), A revised model for the density and thermal expansivity of K_2O-Na_2O-CaO-MgO-Al_2O_3-SiO_2 liquids from 700 to 1900 K: extension to crustal magmatic temperatures. *Contributions to Mineralogy and Petrology*, **130**, 1-11, https://doi.org/10.1007/s004100050345

Laubier M, Grove TL, Langmuir CH (2014) Trace element mineral/melt partitioning for basaltic and basaltic andesitic melts: An experimental and LA-ICP-MS study with application to the oxidation state of mantle source regions. *Earth and Planetary Science Letters* **392**: 265-278

Layne, G.D. and Shimizu, N., (1998a) Measurement of lead isotope ratios in common silicate and sulfide phases using the Cameca IMS 1270 Ion Microprobe, in G. Gillen et al., eds., *Secondary Ion Mass Spectrometry SIMS XI*, John Wiley, 63-65.

Layne, G.D. and Shimizu, N., (1998b) High resolution-high transmission Secondary Ion Mass Spectrometry (SIMS) for the in situ microanalysis of lead isotope ratios in minerals and melt inclusions, Eight Annual V.M. Goldschmidt Conference, *Mineralogical Magazine*, **62A**, 860-861.

Layne, G.D., (2006) Application of secondary ion mass spectrometry to the determination of traditional and non-traditional light stable isotopes in melt inclusions, in Melt Inclusions in Plutonic Rocks (J.D. Webster, ed.), *Min. Assoc. Can. Short Course* **36**, 27-50.

Layne, G.D., Kent, A.J.R. and Bach, W. (2009) δ^{37}Cl systematics of a back-arc spreading system: The Lau Basin, *Geology*, **37(5)**, 427–430; https://doi.org/10.1130/G25520A.1

Le Voyer, M. (2009), Rôle des fluides dans la genèse des magmas d'arcs : analyses *in situ* des éléments volatils et des isotopes du bore dans les inclusions magmatiques des olivines primitives, PhD dissertation, Université Blaise Pascal, Clermont-Ferrand, France, p. 276.

Le Voyer, M., Asimow, P.D., Mosenfelder, J.L., Guan, Y., Wallace, P.J., Schiano, P., Stolper, E.M., and Eiler, J.M. (2014) Zonation of H2O and F Concentrations around Melt Inclusions in Olivines: *Journal of Petrology*, **55**, 685–707.

Li, J. & Chou, I.-M. (2015) Hydrogen in silicate melt inclusions from granite detected with Raman spectroscopy. *Journal of Raman Spectroscopy*, 46, 983-986. https://doi.org/10.1002/jrs.4644

Lloyd, A.S., Plank, T., Ruprecht, P., Hauri, E.H., and Rose, W. (2013) Volatile loss from melt inclusions in pyroclasts of differing sizes, *Contributions to Mineralogy and Petrology*, **165**, 129–153, doi: 10.1007/s00410-012-0800-2.

Lloyd, A.S., Ruprecht, P., Hauri, E.H., Rose, W., Gonnermann, H.M., and Plank, T., (2014) NanoSIMS results from olivine-hosted melt embayments: Magma ascent rate during explosive basaltic eruptions : *Journal of Volcanology and Geothermal Research*, **283**, 1–18, doi: 10.1016/j.jvolgeores.2014.06.002.

Lowenstern, J.B. (1995) Applications of silicate-melt inclusions to the study of magmatic volatiles: *Magmas, fluids and ore deposits*, **23**, 71–99.

Lowenstern J. B., Pitcher B. W. (2013) Analysis of H_2O in silicate glass using attenuated total reflectance (ATR) micro-FTIR spectroscopy. American Mineralogist, 98, 1660-1668, https://doi.org/10.2138/am.2013.4466

Lytle, M.L., Kelley, K.A., Hauri, E.H., Gill, J.B., Papia, D., and Arculus, R.J. (2012) Tracing mantle sources and Samoan influence in the northwestern Lau back-arc basin: *Geochemistry Geophysics Geosystems*, **13**, doi: 10.1038/375774a0.

Maclennan, J. (2008) Lead isotope variability in olivine-hosted melt inclusions from Iceland. *Geochimica Et Cosmochimica Acta*, **72**, 4159-4176.

Manley CR (1996) Morphology and maturation of melt inclusions in quartz phenocrysts from the Badlands rhyolite lava flow, southwestern Idaho. American Mineralogist, **81**, 158-168.

Manzini, M., Bouvier, A.S., Barnes, J.D., Bonifacie, M., Rose-Koga, E.F., Ulmer, P., Métrich, N., Bardoux, G., Williams, J., Layne, G.D., Straub, S., Baumgartner, L.P., and John, T. (2017a) SIMS chlorine isotope analyses in melt inclusions from arc settings: *Chemical Geology*, **449**, 112–122.

Manzini, M., Bouvier, A.-S., Baumgartner, L.P., Müntener, O., Rose-Koga, E.F., Schiano, P., Escrig, S., Meibom, A., and Shimizu, N. (2017b) Weekly to monthly time scale of melt inclusion entrapment prior to eruption recorded by phosphorus distribution in olivine from mid-ocean ridges: *Geology*, doi: 10.1130/G39463.1.

Manzini, M., Bouvier, A.-S., Baumgartner, L.P., Rose-Koga, E.F., Schiano, P., and Shimizu, N. (2019) Grain scale processes recorded by oxygen isotopes in olivine-hosted melt inclusions from two MORB samples, *Chemical Geology*, **511**, 11–20, doi: 10.1016/j.chemgeo.2019.02.025.

Massare, D., Métrich, N., and Clocchiatti, R. (2002) High-temperature experiments on silicate melt inclusions in olivine at 1 atm: inference on temperatures of homogenization and H_2O concentrations, Chemical Geology, **183**, 87–98.

McMillan, P. (1984) Structural studies of silicate glasses and melts—applications and limitations of Raman spectroscopy, *American Mineralogist*, **69**, 622–644.

Mernagh, T. P. Kamentsky, V. S. & Kamenetsky, M. B. (2011) A Raman microprobe study of melt inclusions in kimberlites from Siberia, Canada, SW Greenland and South Africa. *Spectrochimica Acta Part A. Molecular and Biomolecular Spectroscopy*, **80**(1), 82-87. https://doi.org/10.1016/j.saa.2011.01.034

Métrich, N., Berry, A. J., O'Neill, H. S. C. & Susini, J. (2009). The oxidation state of sulfur in synthetic and natural glasses determined by X-ray absorption spectroscopy. *Geochimica et Cosmochimica Acta* **73**, 2382–2399.

Mercier, M., Di Muro, A., Métrich, N., and Giordano, D. (2010) Spectroscopic analysis (FTIR, Raman) of water in mafic and intermediate glasses and glass inclusions: *Geochimica et Cosmochimica Acta*, **74**, 5641–5656.

Milman-Barris, M.S., Beckett, J.R., Baker, M.B., Hofmann, A.E., Morgan, Z., Crowley, M.R., Vielzeuf, D., and Stolper, E. (2008) Zoning of phosphorus in igneous olivine: *Contributions to Mineralogy and Petrology*, **155**, 739– 765, https://doi.org/10.1007/s00410-007-0268-7.

Mironov, N., Portnyagin, M., Botcharnikov, R., Gurenko, A., Hoernle, K., and Holtz, F. (2015) Quantification of the CO2 budget and H2O–CO2 systematics in subduction-zone magmas through the experimental hydration of melt inclusions in olivine at high H2O pressure: *Earth and Planetary Science Letters*, **425**, 1–11.

Moore, L., Gazel, E., Tuohy, R., Lloyd, A., Esposito, R., Steele-MacInnis, M., Hauri, E., Wallace, P., Plank, T. & Bodnar, R. J. (2015) Bubbles matter: An assessment of the contribution of vapor bubbles to melt inclusion volatile budgets. *American Mineralogist*, **100**, 806-823. http://dx.doi.org/10.2138/am-2015-5036

Moore, L.R., Mironov, N., Portnyagin, M., Gazel, E., Bodnar, R.J. (2018) Volatile contents of primitive bubble-bearing melt inclusions from Klyuchevskoy volcano, Kamchatka: Comparison of volatile contents determined by mass-balance versus experimental homogenization. *Journal of Volcanology and Geothermal Research*, **358**, 124-131.

Morgan, G.B., and London, D. (1996) Optimizing the electron microprobe analysis of hydrous alkali aluminosilicate glasses : *American Mineralogist*, **81**, 1176–1185.

Morizet, Y., Brooker, R.A., Iacono-Marziano, G., and Kjarsgaard, B.A. (2013) Quantification of dissolved CO2 in silicate glasses using micro-Raman spectroscopy: *American Mineralogist*, **98**, 1788–1802, doi: 10.2138/am.2013.4516.

Mourey A., France L., Laporte D. & Gurenko A. (2017) Characterization of Volatile Contents in Primitive Magmas of an Active Carbonatitic Volcanic Complex (Oldoinyo Lengai, Tanzania). *Goldschmidt Abstracts*, 2821.

Moussallam, Y., Oppenheimer, C., Scaillet, B., Gaillard, F., Kyle, P., Peters, N., Hartley, M., Berlo, K. & Donovan, A. (2014). Tracking the changing oxidation state of Erebus magmas, from mantle to surface, driven by magma ascent and degassing. *Earth and Planetary Science Letters* **393**, 200–209.

Moussallam, Y., Edmonds, M., Scaillet, B., Peters, N., Gennaro, E., Sides, I. & Oppenheimer, C. (2016). The impact of degassing on the oxidation state of basaltic magmas: A case study of Kīlauea volcano. *Earth and Planetary Science Letters* **450**, 317–325.

Moussallam Y., Longpré M-A, McCammon C., Gomez-Ulla A., Rose-Koga E.F., Scaillet B., Peters N., Gennaro E., Paris R., Oppenheimer C. (2019a) Mantle plumes are

oxidized, *Earth and Planetary Science Letters* **527**, doi.org/10.1016/j.epsl.2019.115798.

Moussallam, Y., Rose-Koga, E.F., Koga, K.T., Médard, E., Bani, P., Devidal, J.-L., and Tari, D. (2019b) Fast ascent rate during the 2017–2018 Plinian eruption of Ambae (Aoba) volcano: a petrological investigation: *Contributions to Mineralogy and Petrology*, **174**, doi: 10.1007/s00410-019-1625-z.

Mujin, M. Nakamura, M. Miyake, A. (2017) Eruption style and crystal size distributions: Crystallization of groundmass nanolites in the 2011 Shinmoedake eruption. *American Mineralogist,* **102**, 2367-2380.

Mutchler, S.R., Fedele, L., Bodnar, R.J. (2008) Analysis Management System (AMS) for reduction of laser ablation ICP-MS data: *Mineralogical Association of Canada Short Course Series*, **40**.

Mysen, B. O. & Virgo, D. (1980) Solubility mechanisms of carbon dioxide in silicate melts: A Raman spectroscopic study. *American Mineralogist*, **65**, 885-899.

Newcombe, M.E., Fabbrizio, A., Zhang, Y., Ma, C., Le Voyer, M., Guan, Y., Eiler, J.M., Saal, A.E., and Stolper, E.M. (2014) Chemical zonation in olivine-hosted melt inclusions: *Contributions to Mineralogy and Petrology*, **168**, 1030–26, doi: 10.1007/s00410-014-1030-6.

Nichols A. R. L., Wysoczanski R. J. (2007) Using micro-FTIR spectroscopy to measure volatile contents in small and unexposed inclusions hosted in olivine crystals. Chemical *Geology*, **242**, 371-384, https://doi.org/10.1016/j.chemgeo.2007.04.007

Nielsen, C.H. and Sigurdsson, H. (1981) Quantitative methods for electron microprobe analysis of sodium in natural and synthetic glasses, American Mineralogist, 66, 547-552.

Nikogosian, I., Ersoy, Ö., Whitehouse, M., Mason, P. R. D., de Hoog J. C. M., Wortel, R., van Bergen, M. J. (2016). Multiple subduction imprints in the mantle below Italy detected in a single lava flow. *Earth and Planetary Science Letters*, **449**, 12-19, doi: 10.1016/j.epsl.2016.05.033.

Ochs F. A., Lange R. A. (1999), The density of hydrous magmatic liquids. *Science*, **283**, 1314-1317, https://doi.org/10.1126/science.283.5406.1314

O'Hara, M.J. (1968) Are Ocean Floor Basalts Primary Magma? *Nature*, **220**, 683–686, doi: 10.1038/220683a0.

Óladóttir, B.A., Sigmarsson, O., Larsen, G., and Devidal, J.-L. (2011) Provenance of basaltic tephra from Vatnajökull subglacial volcanoes, Iceland, as determined by major- and trace-element analyses: *The Holocene*, **21**, 1037-1048.

Pamukcu AS, Gualda GAR, Rivers ML (2013) Quantitative 3D petrography using x-ray tomography 4: Assessing glass inclusion textures with propagation phase-contrast tomography. *Geosphere*, **9**, 1704-1713.

Pamukcu AS, Gualda GAR, Begue F, Gravley DM (2015) Melt inclusion shapes: Timekeepers of short-lived giant magma bodies. *Geology*, **43**, 947-950.

Peppard, B. T., Steele A. M., Davis A. M., Wallace, P. J., Anderson, A. T. (2001) Zoned quartz phenocrysts from the rhyolitic Bishop Tuff, American Mineralogist, **86**, 1034-1052.

Portnyagin, M., Almeev, R., Matveev, S., and Holtz, F., 2008, Experimental evidence for rapid water exchange between melt inclusions in olivine and host magma: Earth and Planetary Science Letters, v. 272, p. 541–552.

Qin, Z., Lu, F., Anderson, A.T. (1992) Diffusive reequilibration of melt and fluid inclusions, American Mineralogist, 77, 565-576.

Rasmussen, D.J., Kyle, P.R., Wallace, P.J., Sims, K.W.W., Gaetani, G.A., and Phillips, E.H. (2017) Understanding Degassing and Transport of CO2-rich Alkalic Magmas at Ross Island, Antarctica using Olivine-Hosted Melt Inclusions. *Journal of Petrology*, *58*, 841–862.

Reinhard AA, Jackson MG, Koornneef JM, Rose-Koga EF, Blusztajn J, Konter JG, Koga KT, Wallace PJ, and Harvey J, (2018) Sr and Nd isotopic compositions of individual olivine-hosted melt inclusions from Hawai'i and Samoa: Implications for the origin of isotopic heterogeneity in melt inclusions from OIB lavas. *Chemical Geology*, **495**, 36-49.

Richard, A., Morlot, C., Créon, L., Beaudoin, N., Balistky, V.S., Pentelei, S., Dyja-Person, V., Giuliani, G., Pignatelli, I., Legros, H., Sterpenich, J., and Pironon, J. (2018) Advances in 3D imaging and volumetric reconstruction of fluid and melt

inclusions by high resolution X-ray computed tomography. *Chemical Geology*, 1–12, doi: 10.1016/j.chemgeo.2018.06.012.

Riker, J. (2005) The 1859 Eruption of Mauna Loa Volcano, Hawai'i: Controls on the Development of Long Lava Channels, PhD dissertation, University of Oregon, USA.

Roberge J, Wallace PJ, Kent AJR (2013) Magmatic processes in the Bishop Tuff rhyolitic magma based on trace elements in melt inclusions and pumice matrix glass. Contributions to Mineralogy and Petrology, 165:237-257

Roedder, E. (1963) Studies of fluid inclusions III: extraction and quanttative analysis of inclusions in the milligram range: *Economic Geology*, **58**, 353–374.

Roedder, E. (1979) Origin and significance of magmatic inclusions. Bulletin de Mineralogie, **102**, 467-510.

Roedder, E. (1984) Fluid Inclusions. Reviews in Mineralogy, **12**, Mineralogical Society of America, 644 p.

Roeder, P.L. and Emslie, R.F. (1970) Olivine-Liquid Equilibrium, *Contribution to Mineralogy and Petrology*, **29**, 275-289.

Rosasco, G.J., Roedder, E. & Simmons, J.H. (1975) Laser-excited Raman spectroscopy for nondestructive partial analysis of individual phases in fluid inclusions in minerals. *Science*, **190**, 557–560.

Rosasco, G.J. & Roedder, E. (1979) Application of a new Raman microprobe spectrometer to nondestructive analysis of sulfate and other ions in individual phases in fluid inclusions in minerals. *Geochimica et Cosmochimica Acta*, **43**, 1907–1915.

Rose, E.F., Shimizu, N., Layne, G.D., and Grove, T.L. (2001) Melt production beneath Mt. Shasta from boron data in primitive melt inclusions: *Science*, **293**, 281–283.

Rose-Koga, E.F., Koga, K., Schiano, P., and Le Voyer, M. (2012) Mantle source heterogeneity for South Tyrrhenian magmas revealed by Pb isotopes and halogen contents of olivine-hosted melt inclusions. *Chemical Geology*, **334**, 266-279.

Rose-Koga, E.F., Koga, K.T., Moreira, M., Vlastélic, I., Jackson, M.G., Whitehouse, M.J., Shimizu, N., and Habib, N. (2017) Geochemical systematics of Pb isotopes, fluorine, and sulfur in melt inclusions from Sao Miguel, Azores. *Chemical Geology*, 2017. **458**: p. 22-37.

Rose-Koga E.F., Koga K.T., Devidal J-L., Shimizu N., Le Voyer M., Dalou C., Döbeli M. (2020) *In-situ* measurements of magmatic volatile elements, F, S and Cl by electron microprobe, secondary ion mass spectrometry, and elastic recoil detection analysis, *American Mineralogist*, doi.org/10.2138/am-2020-7221.

Rowe, M. C., Kent, A. J. R. & Nielsen, R. L. (2007). Determination of sulfur speciation and oxidation state of olivine hosted melt inclusions. *Chemical Geology* **236**, 303–322.

Ruscitto, D.M., Wallace, P.J., Johnson, E.R., Kent, A.J.R., and Bindeman, I.N. (2010) Volatile contents of mafic magmas from cinder cones in the Central Oregon High Cascades: Implications for magma formation and mantle conditions in a hot arc: *Earth and Planetary Science Letters*, **298**, 153–161, doi: 10.1016/j.epsl.2010.07.037.

Ruscitto DM, Wallace PJ, Kent AJR (2011) Revisiting the compositions and volatile contents of olivine-hosted melt inclusions from the Mount Shasta region: Implications for the formation of high-Mg andesites. *Contributions to Mineralogy and Petrology*, **162**:109-132, DOI 10.1007/s00410-010-0587-y

Saal, A., Hart, S.R., Shimizu, N., Hauri, E.H., and Layne, G. (1998) Pb isotopic variability in melt inclusions from oceanic island basalts, Polynesia. *Science*, 1998. **282**, 1481-1484.

Sack RO, Walker D, Carmichael ISE (1987) Experimental petrology of alkalic lavas: constraints on cotectics of multiple saturation in natural basic liquids. *Contrib Mineral Petrol* **96**, 1–23.

Schiano, P. (2003) Primitive mantle magmas recorded as silicate melt inclusions in igneous minerals, Earth Sci. Rev. 63, 121-144.

Schiavi, F., Rosciglione, A., Kitagawa, H., Kobayashi, K., Nakamura, E., Nuccio, P. M., Ottolini, L., Paonita, A., Vannucci, R. (2015) Geochemical heterogeneities in magma beneath Mount Etna recorded by 2001-2006 melt inclusions. *Geochemistry Geophysics Geosystems*, **16**, 2109-2126.

Schiavi, F., Provost, A., Schiano, P., and Cluzel, N. (2016) P V T X evolution of olivine-hosted melt inclusions during high-temperature homogenization treatment: *Geochimica et Cosmochimica Acta*, **172**, 1–21, doi: 10.1016/j.gca.2015.09.025.

Severs, M. J., Azbej, T., Thomas, J. B., Mandeville, C. W., Jr. & Bodnar, R. J. (2007) Experimental determination of H_2O loss from melt inclusions during laboratory heating. *Chemical Geology*, **237**(3-4), 358-371, http://dx.doi.org/10.1016/j.chemgeo.2006.07.008

Shatsky, V., Zedgenizov, D., Ragozin, A. & Kalinina, V. (2019) Silicate melt inclusions in diamonds of eclogite paragenesis from placers on the northeastern Siberian craton. *Minerals,* **9**, 412. http://dx.doi.org/10.3390/min9070412

Shaw, A.M., Hauri, E.H., Fischer, T.P., Hilton, D.R., and Kelly, K.A. (2008) Hydrogen isotopes in Mariana arc melt inclusions: Implications for subduction dehydration and the deep-Earth water cycle. *Earth and Planetary Science Letters*, **275**, 138–145.

Shaw, A.M., Behn, M.D., Humphris, S.E., Sohn, R.A., and Gregg, P.M. (2010) Deep pooling of low degree melts and volatile fluxes at the 85°E segment of the Gakkel Ridge: Evidence from olivine-hosted melt inclusions and glasses: E*arth and Planetary Science Letters*, **289**, 311–322, doi: 10.1016/j.epsl.2009.11.018.

Shea, T., Costa, F., Krimer, D., and Hammer, J.E. (2015) Accuracy of timescales retrieved from diffusion modeling in olivine: A 3D perspective: *American Mineralogist*, **100**, 2026–2042, doi: 10.2138/am-2015-5163.

Shea, T., Hammer, J.E., Hellebrand, E., Mourey, A.J., Costa, F., First, E.C., Lynn, K.J., and Melnik, O. (2019) Phosphorus and aluminum zoning in olivine: contrasting behavior of two nominally incompatible trace elements: *Contributions to Mineralogy and Petrology*, 1–24, doi: 10.1007/s00410-019-1618-y.

Shorttle, O., Moussallam, Y., Hartley, M. E., Maclennan, J., Edmonds, M. & Murton, B. J. (2015). Fe-XANES analyses of Reykjanes Ridge basalts: Implications for oceanic crust's role in the solid Earth oxygen cycle. *Earth and Planetary Science Letters* **427**, 272–285.

Sinton, C.W., Christie, D.M., and Coombs, V.L., 1993, Near-primary melt inclusions in anorthite phenocrysts from the Galapagos Platform: *Earth and Planetary Science Letters*, **119**, 527–537.

Sobolev, A.V., Dmitriev, L.V., Barsukov, V.L., Nevsorov, V.N., Slutsky, A.B. (1980) The formation conditions of the high-magnesian olivines from the monomineralic fraction of Luna 24 regolith. *Proc. 11th Lunar Sci. Conf.*, 105–116.

Sobolev, A.V., and Danyushevsky, L.V. (1994) Petrology and Geochemistry of Boninites from the North Termination of the Tonga Trench: Constraints on the Generation Conditions of Primary High-Ca Boninite Magmas: *Journal of Petrology*, **35**, 1183–1211.

Sobolev, A.V., and Chaussidon, M. (1996) H_2O concentrations in primary melts from supra-subduction zones and mid-ocean ridges: Implications for H_2O storage and recycling in the mantle: *Earth and Planetary Science Letters*, **137**, 45–55.

Sobolev, A.V., Hofmann, A.W., Jochum, K.P., Kuzmin, D.V., and Stoll, B. (2011) A young source for the Hawaiian plume. *Nature*. **476**, 434-437.

Sorby, H.C. (1858) On the Microscopical, Structure of Crystals, indicating the Origin of Minerals and Rocks: *Quarterly Journal of the Geological Society*, **14**, 453–500, doi: 10.1144/GSL.JGS.1858.014.01-02.44.

Spandler C, HStC O'Neill, Kamenetsky VS (2007) Survival times of anomalous melt inclusions: constraints from element diffusion in olivine and chromite. *Nature* **447**:303–306.

Steele-MacInnis, M., Esposito, R., and Bodnar, R.J., (2011) Thermodynamic model for the effect of post-entrapment crystallization on the H_2O-CO_2 systematics of vapor-saturated, silicate melt inclusions. *Journal of Petrology*, **52**, 2461-2482.

Steele-Macinnis, M., Esposito, R., Moore, L.R., Hartley, M.E. (2017) "Heterogeneously entrapped, vapor-rich melt inclusions record pre-eruptive magmatic volatile contents," *Contributions to Mineralogy and Petrology*, 172:18, 1-13.

Stolper E (1982) Water in silicate glasses: An infrared spectroscopic study. *Contributions to Mineralogy and Petrology*, **81**, 1-17, https://doi.org/10.1007/BF00371154

Stracke, A., Genske, F., Berndt, J., and Koornneef, J.M. (2019). Ubiquitous ultra-depleted domains in Earth's mantle. *Nature Geoscience*, **12**, 851–855, doi: 10.1038/s41561-019-0446-z.

Straub, S.M. and Layne, G.D. (2002) The systematics of boron isotopes in Izu arc front volcanic rocks, *Earth Planet. Sci. Letters*, **198**, 25-39; https://doi.org/10.1016/S0012-821X(02)00517-4

Student, J.J., and Bodnar, R.J. (1999) Synthetic Fluid Inclusions XIV: Coexisting Silicate Melt and Aqueous Fluid Inclusions in the Haplogranite-H_2O-NaCl-KCl: *Journal of Petrology*, **40**, 1509–1525.

Student, J. J. & Bodnar, R. J. (2004) Silicate melt inclusions in porphyry copper deposits: Identification and homogenization behavior. *Canadian Mineralogist*, **42**,1583-1599.

Sun C and Liang Y (2013) The importance of crystal chemistry on REE partitioning between mantle minerals (garnet, clinopyroxene, orthopyroxene, and olivine) and basaltic melts. *Chemical Geology* **358**: 23-36

Tait, S. (1992) Selective preservation of melt inclusions in igneous phenocrysts: *American Mineralogist,* **77**, 146–155.

Tamic N., Behrens H., Holtz F. (2001) The solubility of H_2O and CO_2 in rhyolitic melts in equilibrium with a mixed CO_2-H_2O fluid phase. *Chemical Geology*, **174**, 333-347, https://doi.org/10.1016/S0009-2541(00)00324-7

Thomas, R., (2000) Determination of water contents of granite melt inclusions by confocal laser Raman microprobe spectroscopy : *American Mineralogist*, **85**, 868–872.

Thomas, J. B., Bodnar, R. J., Shimizu, N. & Sinha, A. K. (2002) Determination of zircon/melt trace element partition coefficients from SIMS analysis of melt inclusions in zircon. *Geochimica et Cosmochimica Acta*, **66**, 2887-2902.

Thomas, J. B., Bodnar, R. J., Shimizu, N. & Chesner, C. (2003) Melt Inclusions in Zircon. *in* ZIRCON, J.M. Hanchar & P.W.O. Hoskins, eds., *Mineralogical Society of America, Reviews in Mineralogy & Geochemistry*, **53**, 63-87.

Thomas, R. & Davidson, P. (2012) The application of Raman spectroscopy in the study of fluid and melt inclusions. *Zeitschrift der Deutschen Gesellschaft für Geowissenschaften (ZDGG)*, **162**, 113-126 doi: 10.1127/1860-1804/2012/0163-0113.

Thomas, R., Kamenetsky, V.S., and Davidson, P. (2006) Laser Raman spectroscopic measurements of water in unexposed glass inclusions. *American Mineralogist*, **91**, 467-470.

Tison, A. (2006) Étude expérimentale des inclusions magmatiques, Université Blaise Pascal, Clermont- Ferrand, 50p [in French].

Toplis, M.J. (2005) The thermodynamics of iron and magnesium partitioning between olivine and liquid: criteria for assessing and predicting equilibrium in natural and experimental systems, *Contributions to Mineralogy and Petrology*, **149**, 22–39.

Tollan, P., Ellis, P., Troch, J., Neukampf J. (2019) Assessing magmatic volatile equilibria through FTIR spectroscopy of unexposed melt inclusions and their host quartz: a new technique and application to the Mesa Falls Tuff, Yellowstone: *Contributions to Mineralogy and Petrology*, **174**, doi: 10.1007/s00410-019-1561-y.

Tuohy, R.M., Wallace, P.J., Loewen, M.W., Swanson, D.A., and Kent, A.J.R. (2016) *Geochimica et Cosmochimica Acta*, **185**, 1–55, doi: 10.1016/j.gca.2016.04.020.

Vigouroux N, Wallace P, Kent AJR (2008) Volatiles in high-K magmas from the western Trans-Mexican Volcanic Belt: Evidence for fluid-flux melting and extreme enrichment of the mantle wedge by subduction processes. *Journal of Petrology*, **49**:1589-1618

Von Aulock F. W., Kennedy B. M., Schipper C. I., Castro J. M., Martin D. E., Oze C., Watkins J. M., Wallace P. J., Puskar L., Nichols A. R. L., Tuffen H., (2014) Advances in Fourier transform infrared spectroscopy of natural glasses: From sample preparation to data analysis. *Lithos*, **206-207**, 52-64, http://dx.doi.org/10.1016/j.lithos.2014.07.017

Walker, D., Shibata, T. and DeLong, S.E. (1979) Abyssal tholeiites from the Oceanographer Fracture Zone, II. Phase equilibria and mixing. *Contributions to Mineralogy and Petrology,* **70**, 111-125.

Wallace, P., and Carmichael, I.S.E. (1992) Sulfur in basaltic magmas: *Geochimica et Cosmochimica Acta*, **56**, 1863–1874, doi: 10.1016/0016-7037(92)90316-B.

Wallace, P.J., and Carmichael, I.S.E. (1994) Sulfur speciation in submarine basal- tic glasses as determined by measurements of S*K*a X-ray wavelength shifts. *American Mineralogist*, **79**, 161–167.

Wallace P. J., Anderson A. T., Davis A. M. (1999) Gradients in H_2O, CO_2, and exsolved gas in a large-volume silicic magma system: Interpreting the record preserved in melt inclusions from the Bishop Tuff. *Journal of Geophysical Research*, **104** (B9), 20097–20122.

Wallace, P.J., Kamenetsky, V.S., Cervantes, P. (2015) Melt inclusion CO2 contents, pressures of olivine crystallization, and the problem of shrinkage bubbles, *American Mineralogist*, **100**, 787–794.

Watson, E.B. (1976) Two-Liquid Partition Coefficients: Experimental Data and Geochemical Implications, *Contributions to Mineralogy and Petrology*, **56**, 119–134.

Welsch, B., Hammer, J., and Hellebrand, E. (2014) Phosphorus zoning reveals dendritic architecture of olivine: *Geology*, **42**, 867–870, doi: 10.1130/G35691.1.

Wilke, M., Farges, F., Petit, P.-E., Brown, G. E. & Martin, F. (2001). Oxidation state and coordination of Fe in minerals: An Fe K-XANES spectroscopic study. *American Mineralogist* **86**, 714–730.

Wilke, M., Partzsch, G. M., Bernhardt, R. & Lattard, D. (2004). Determination of the iron oxidation state in basaltic glasses using XANES at the K-edge. *Chemical Geology* **213**, 71–87.

Wilke, M., Schmidt, C., Farges, F., Malavergne, V., Gautron, L., Simionovici, A., Hahn, M. & Petit, P.-E. (2006). Structural environment of iron in hydrous aluminosilicate glass and melt-evidence from X-ray absorption spectroscopy. *Chemical Geology* **229**, 144–161.

Wilke, M., Jugo, P. J., Klimm, K., Susini, J., Botcharnikov, R., Kohn, S. C. & Janousch, M. (2008). The origin of S4 detected in silicate glasses by XANES. *American Mineralogist* **93**, 235–240.

Wysoczanski R. J. & Tani K. (2006) Spectroscopic FTIR imaging of water species in silicic volcanic glasses and melt inclusions: An example from the Izu-Bonin arc. Journal of Volcanology and Geothermal Research, 156, 302-314, https://doi.org/10.1016/j.jvolgeores.2006.03.024

Yang, K. & Bodnar, R. J. (1994) Magmatic-hydrothermal evolution in the “bottoms” of porphyry copper systems: Evidence from silicate melt and aqueous inclusions in granitoid intrusions in the Gyeongsang Basin, South Korea. *International Geology Review*, **36**, 608-628.

Yasuda A. (2014) A new technique using FT-IR micro-reflectance spectroscopy for measurement of water concentrations in melt inclusions. *Earth, Planets and Space*, 66, 34, http://www.earth-planets-space.com/content/66/1/34

Yurimoto, H., Kogiso, T., Abe, K., Barsczus, H.G., Utsunomiya, A., and Maruyama, S., (2004) Lead isotopic compositions in olivine-hosted melt inclusions from HIMU basalts and possible link to sulfide components. *Physics of the Earth and Planetary Interiors*, 2004. **146**, 231-242.

Zajacz, Z., Halter, W., Malfait, W.J., Bachmann, O., Bodnar, R.J., Hirschmann, M.M., Mandeville, C.W., Morizet, Y., Müntener, O., Ulmer, P., and Webster, J.D. (2005) A composition-independent quantitative determination of the water content in silicate glasses and silicate melt inclusions by confocal Raman spectroscopy: *Contributions to Mineralogy and Petrology*, 150, 631–642, doi: 10.1007/s00410-005-0040-9.

Zhang, Y. (1998) Mechanical and phase equilibria in inclusion–host systems: *Earth and Planetary Science Letters*, **157**, p. 209–222.

Zhang, H. L., Hirschmann, M. M., Cottrell, E., Newville, M. & Lanzirotti, A. (2016). Structural environment of iron and accurate determination of Fe3+/ΣFe ratios in andesitic glasses by XANES and Mössbauer spectroscopy. *Chemical Geology* **428**, 48–58.

Zhang, H. L., Cottrell, E., Solheid, P. A., Kelley, K. A. & Hirschmann, M. M. (2018). Determination of Fe3+/ΣFe of XANES basaltic glass standards by Mössbauer spectroscopy and its application to the oxidation state of iron in MORB. *Chemical Geology* **479**, 166–175.

Figure 1A

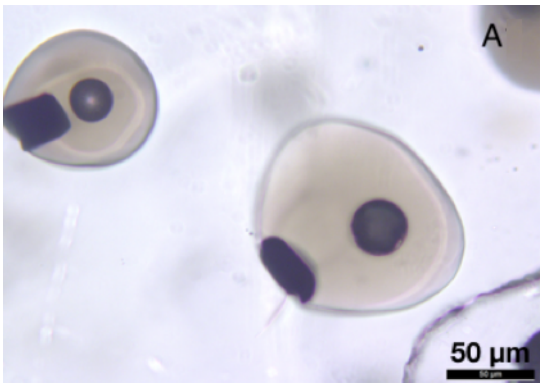

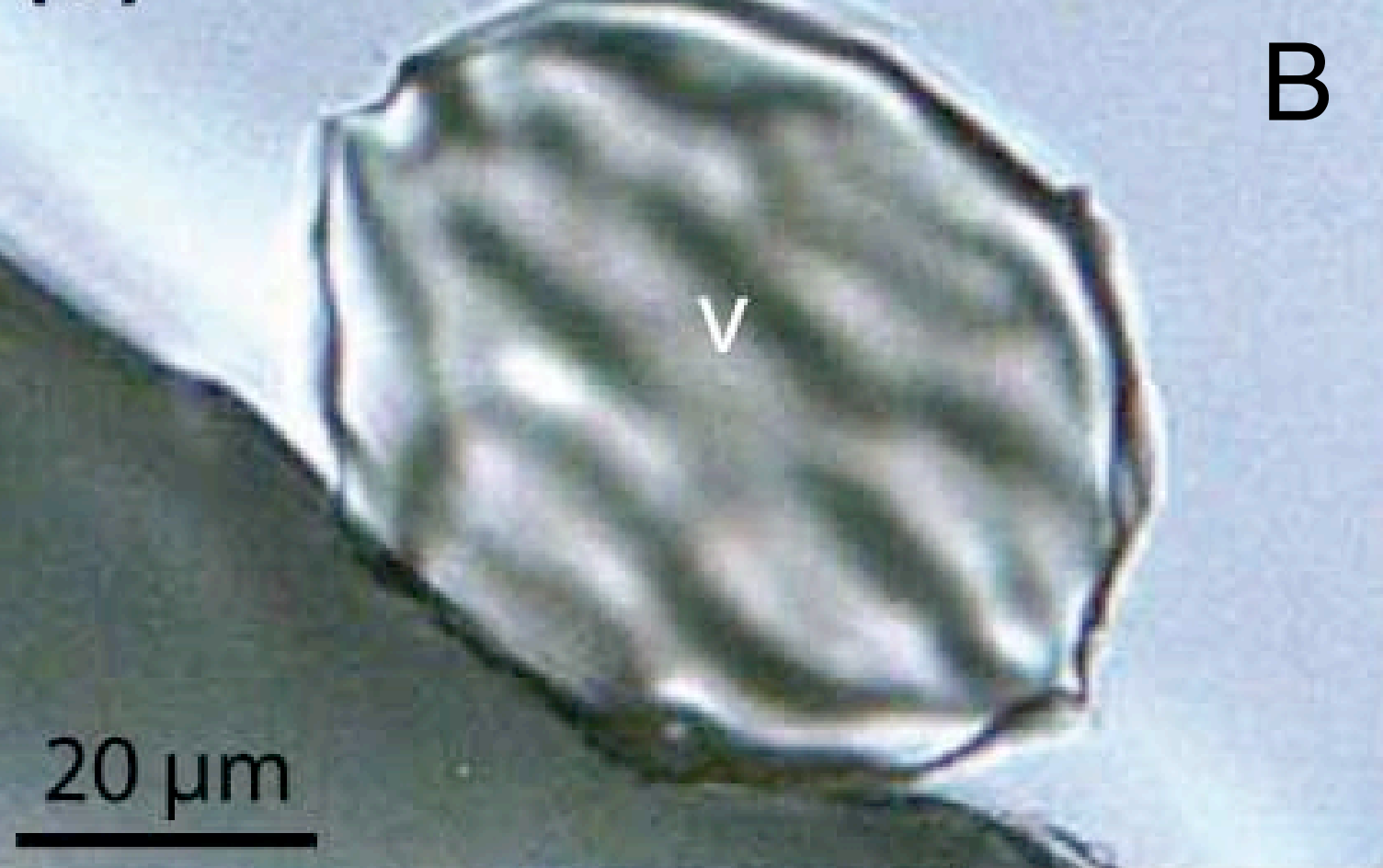
B
V
20 µm

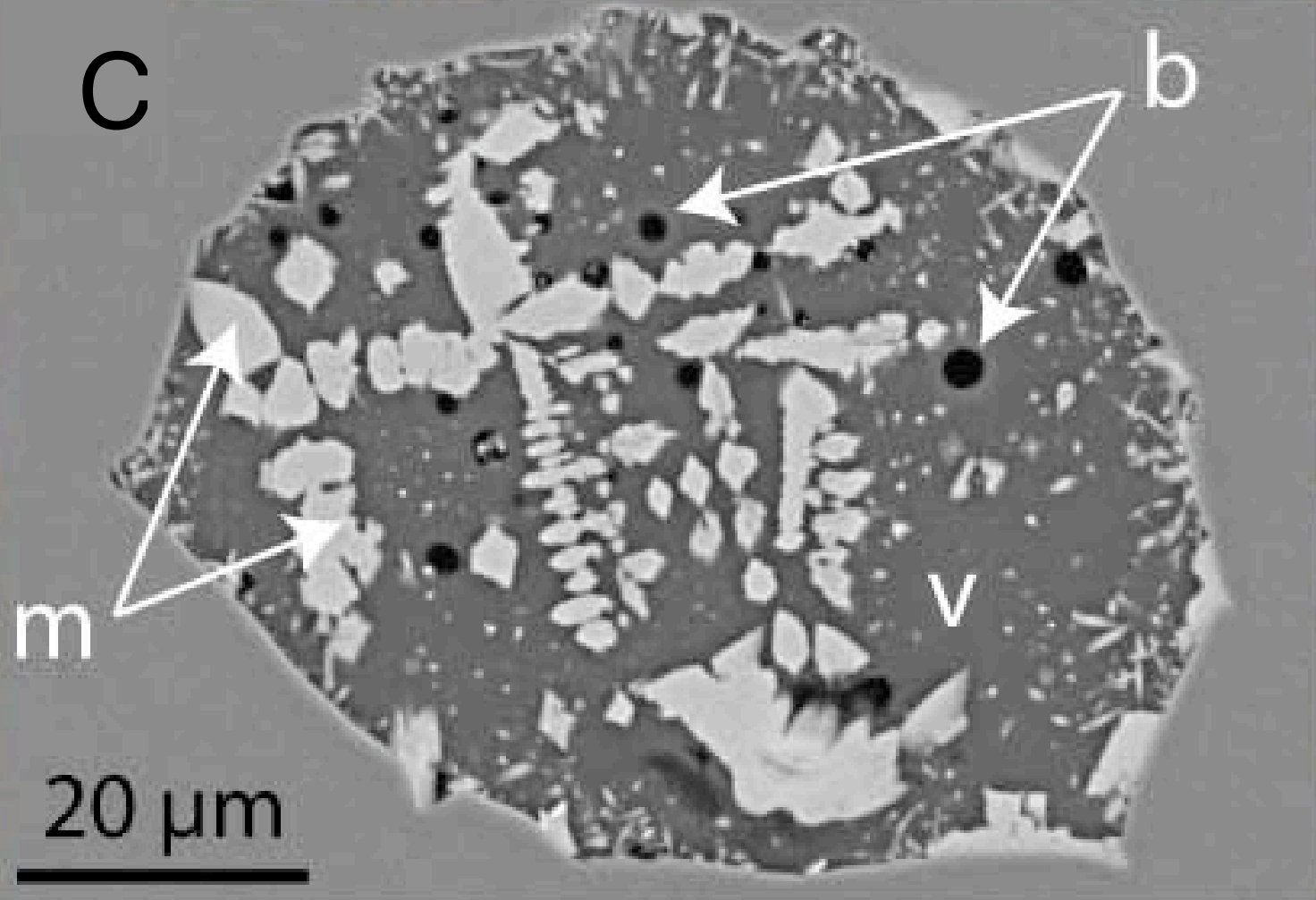
C
b
m
v
20 µm


D
15 µm

Figure 2

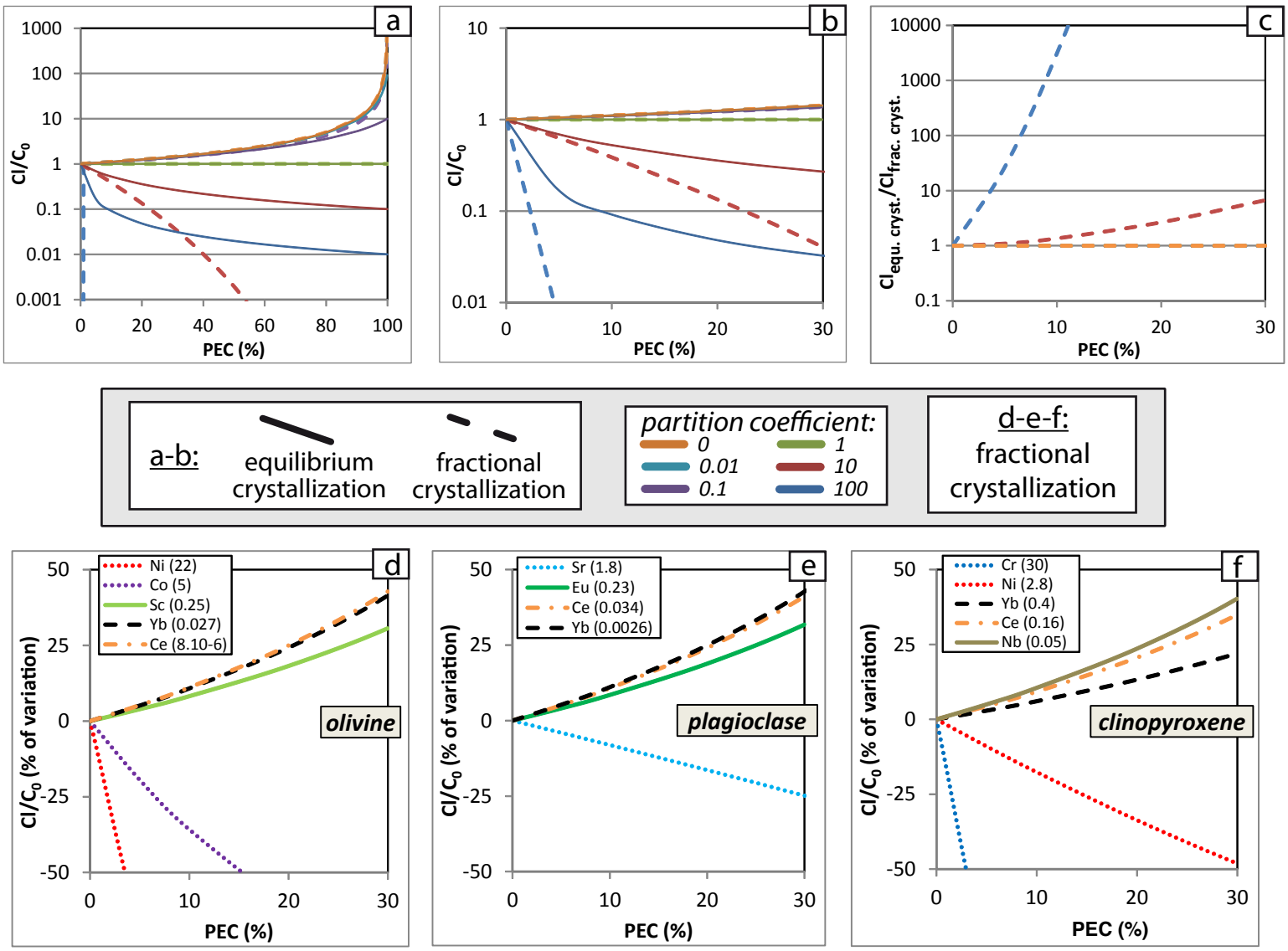
a
b
c
Cl/C0
Clequ. cryst./Clfrac. cryst.
PEC (%)
a-b:
equilibrium crystallization
fractional crystallization
partition coefficient:
0
0.01
0.1
1
10
100
d-e-f:
fractional crystallization
d
e
f
Ni (22)
Co (5)
Sc (0.25)
Yb (0.027)
Ce (8.10-6)
olivine
Sr (1.8)
Eu (0.23)
Ce (0.034)
Yb (0.0026)
plagioclase
Cr (30)
Ni (2.8)
Yb (0.4)
Ce (0.16)
Nb (0.05)
clinopyroxene
Cl/C0 (% of variation)

Figure 3

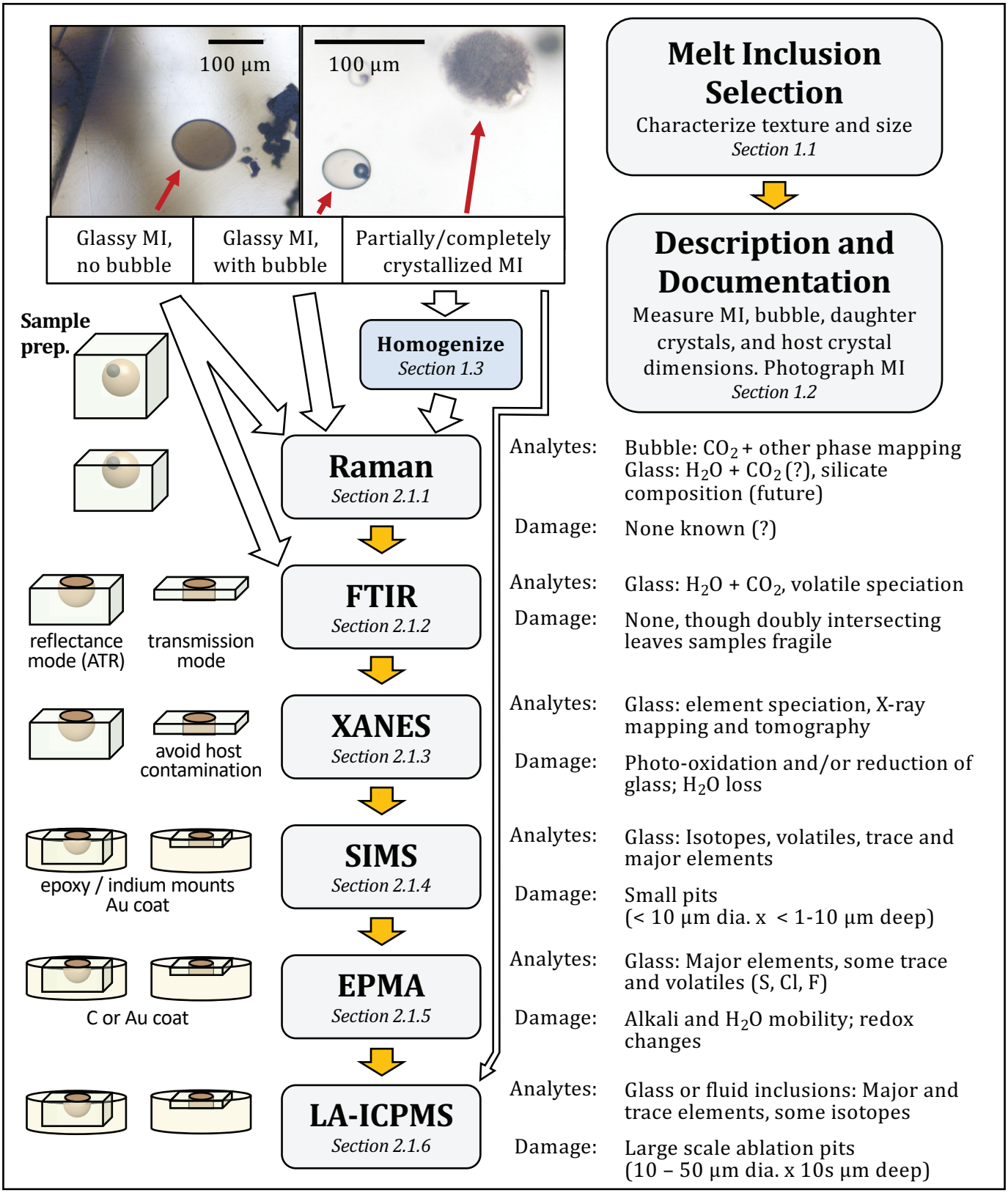
100 µm
100 µm
Glassy MI, no bubble
Glassy MI, with bubble
Partially/completely crystallized MI
Melt Inclusion Selection
Characterize texture and size
Section 1.1
Description and Documentation
Measure MI, bubble, daughter crystals, and host crystal dimensions. Photograph MI
Section 1.2
Sample prep.
Homogenize
Section 1.3
Raman
Section 2.1.1
Analytes: Bubble: CO_2 + other phase mapping Glass: H_2O + CO_2 (?), silicate composition (future)
Damage: None known (?)
FTIR
Section 2.1.2
reflectance mode (ATR)
transmission mode
Analytes: Glass: H_2O + CO_2, volatile speciation
Damage: None, though doubly intersecting leaves samples fragile
XANES
Section 2.1.3
avoid host contamination
Analytes: Glass: element speciation, X-ray mapping and tomography
Damage: Photo-oxidation and/or reduction of glass; H_2O loss
SIMS
Section 2.1.4
epoxy / indium mounts
Au coat
Analytes: Glass: Isotopes, volatiles, trace and major elements
Damage: Small pits (< 10 µm dia. x < 1-10 µm deep)
EPMA
Section 2.1.5
C or Au coat
Analytes: Glass: Major elements, some trace and volatiles (S, Cl, F)
Damage: Alkali and H_2O mobility; redox changes
LA-ICPMS
Section 2.1.6
Analytes: Glass or fluid inclusions: Major and trace elements, some isotopes
Damage: Large scale ablation pits (10 – 50 µm dia. x 10s µm deep)

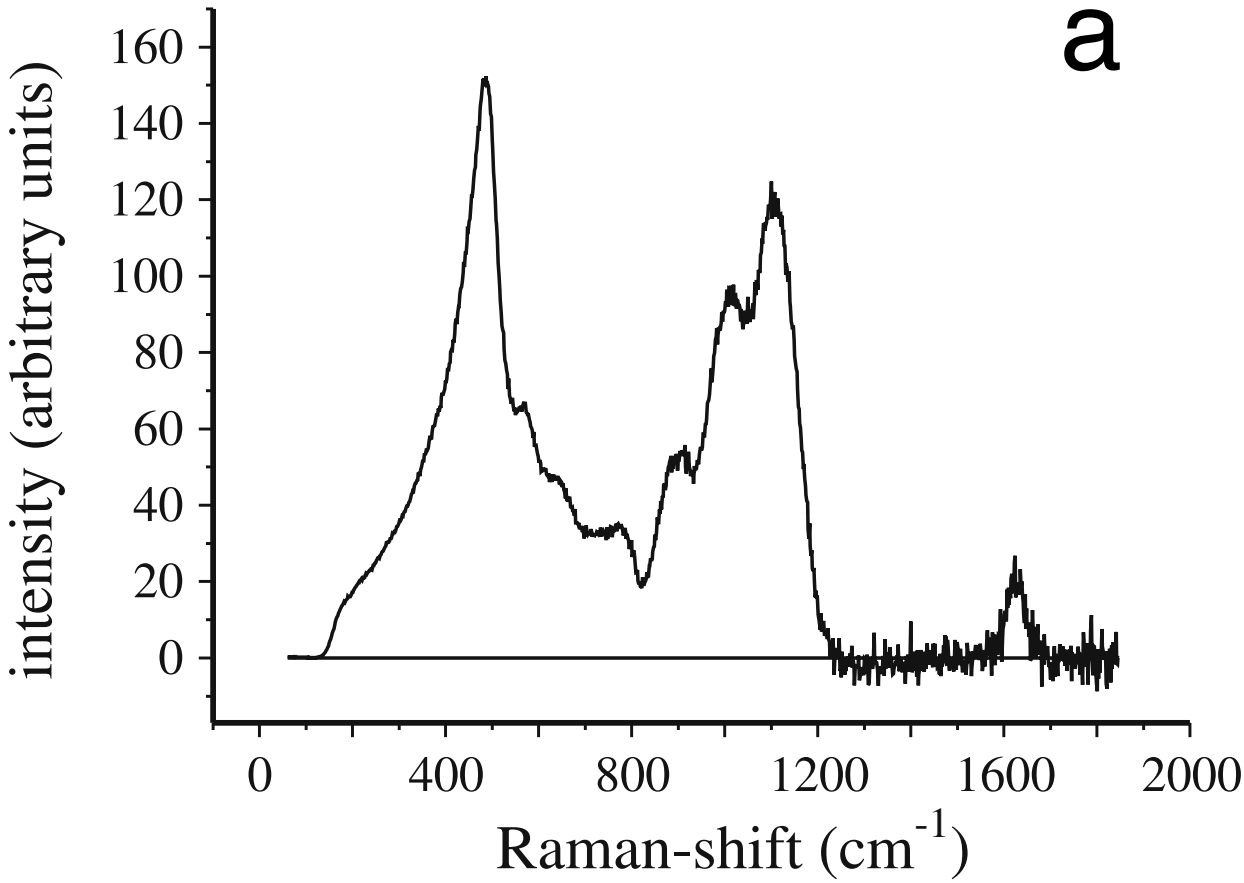
a
intensity (arbitrary units)
160
140
120
100
80
60
40
20
0
0
400
800
1200
1600
2000
Raman-shift (cm-1)

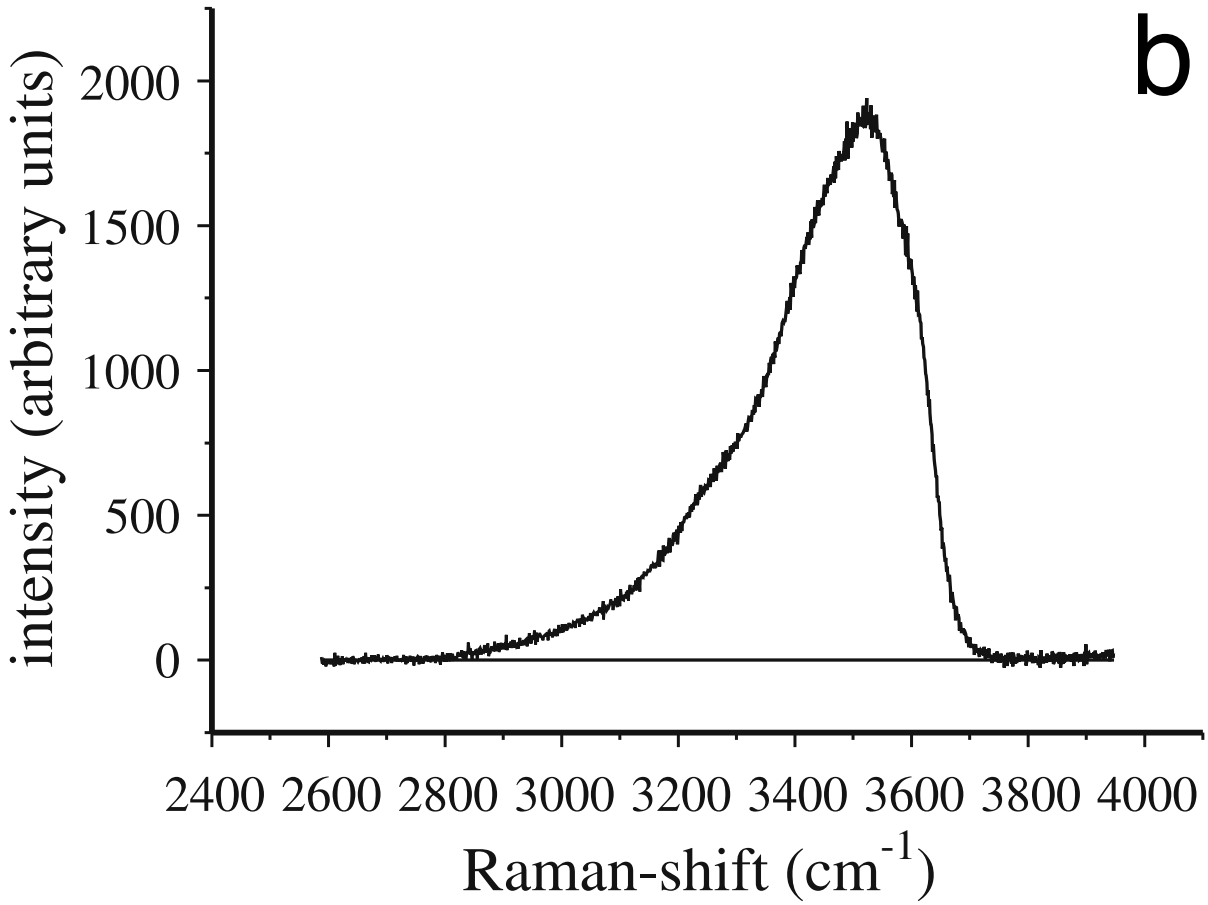
b
intensity (arbitrary units)
2000
1500
1000
500
0
2400 2600 2800 3000 3200 3400 3600 3800 4000
Raman-shift (cm-1)

Figure 5

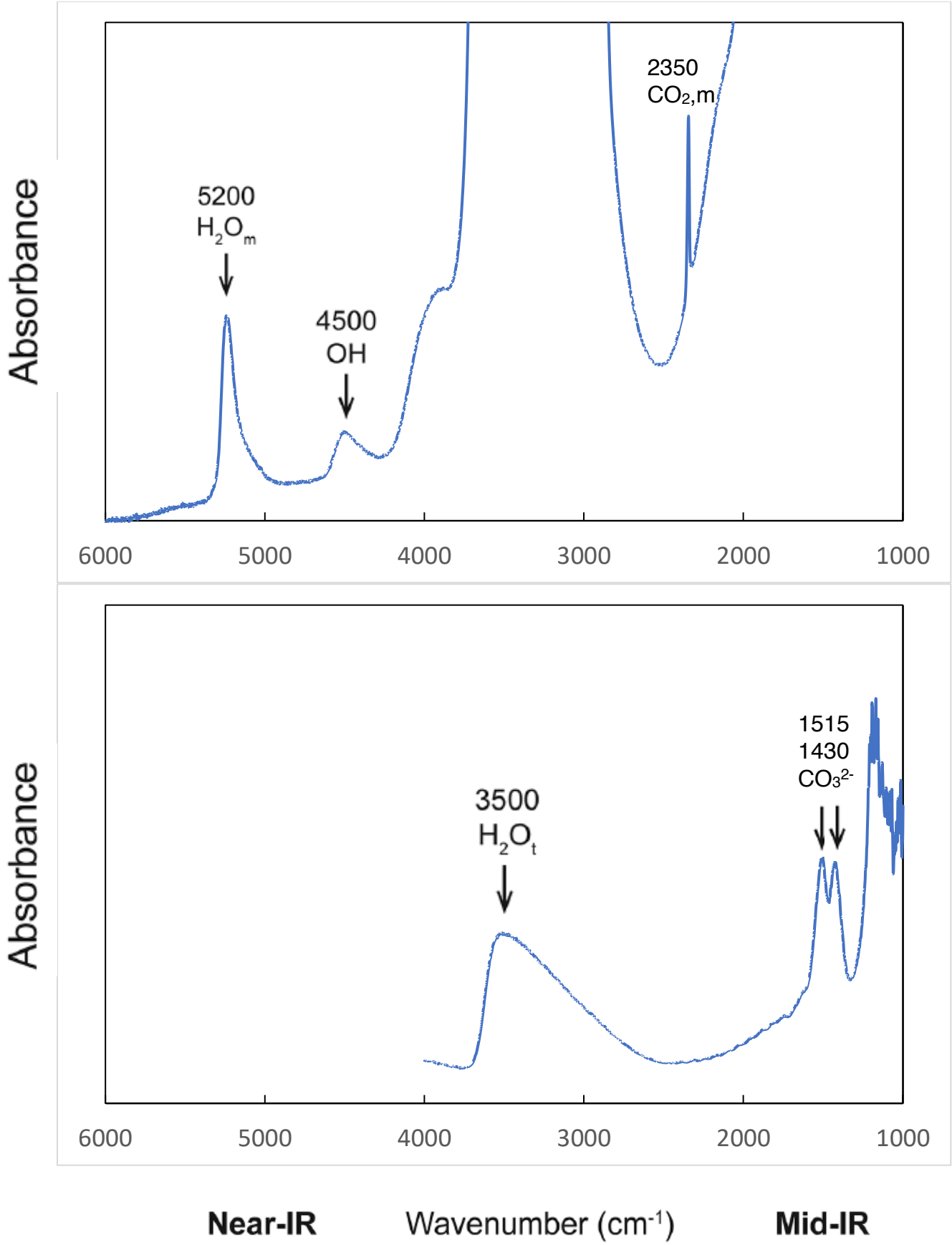
Absorbance
5200
H_2O_m
4500
OH
2350
CO_2,m
6000
5000
4000
3000
2000
1000
Absorbance
3500
H_2O_t
1515
1430
CO_3^{2-}
6000
5000
4000
3000
2000
1000
Near-IR
Wavenumber (cm^{-1})
Mid-IR

Figure 6

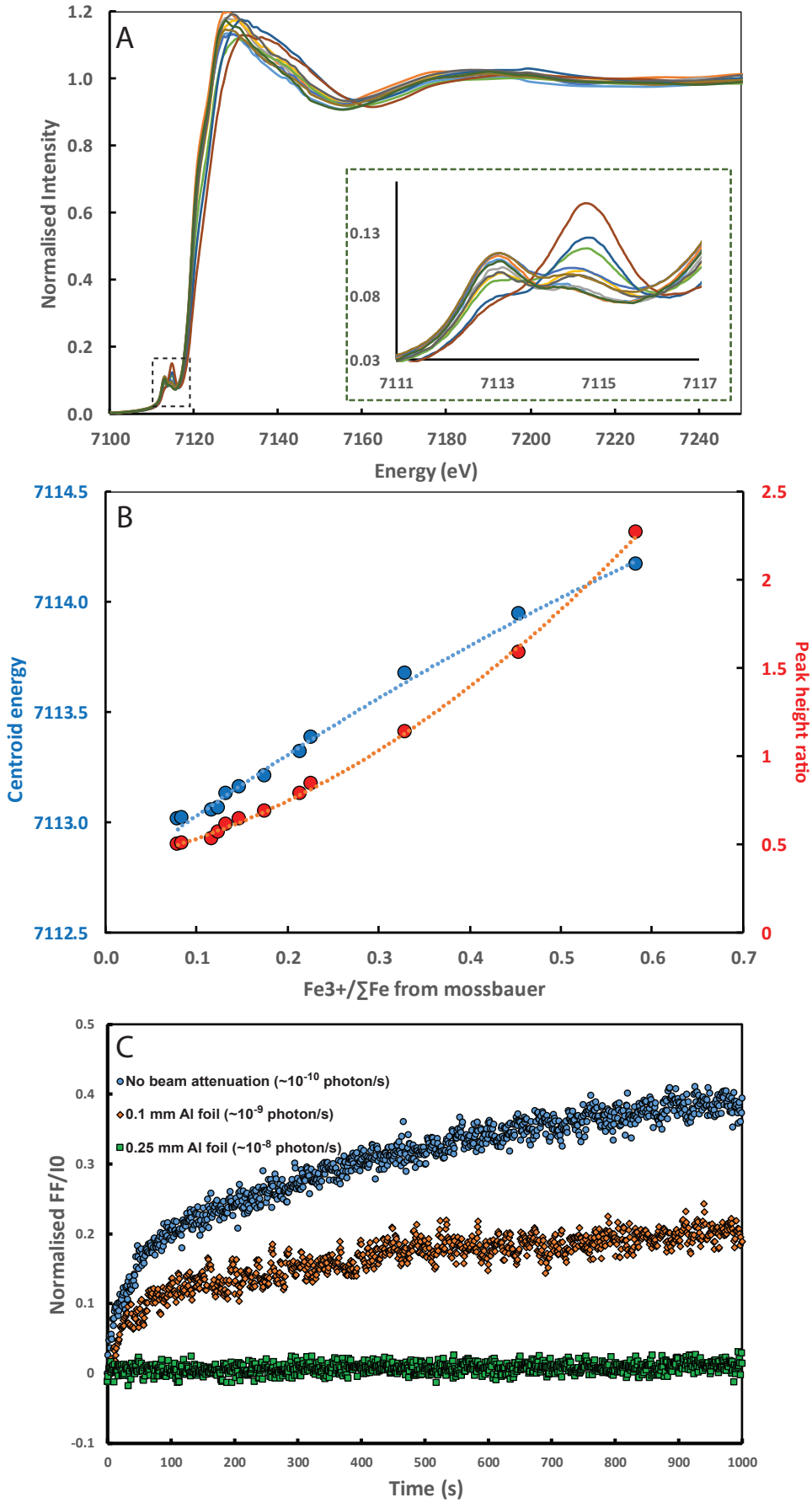

Figure 1: A. Edge-step normalised XANES spectra of the Smithsonian basaltic standard glasses. Inset shows show spectra over the pre-edge region energy range (data from Moussallam et al., 2016). B. Calibration curve for the centroid position (blue) and peak height ratio (red) determined by XANES compared with the Fe3+/∑Fe ratios of the Smithsonian basaltic standard glasses determined by Mößbauer spectroscopy (data from Moussallam et al., in prep.). C. Time series of normalised fluoresced intensity (FF) over I0 at 7114.3 eV integrated over 1 s intervals for a hydrated (5.2 wt.% H2O) basalt under three different beam attenuation conditions. A fresh spot was illuminated with a 2.5 x 1.2 µm beam for each analysis. Note that while photo-oxidation can clearly be seen with no beam attenuation and with an attenuation down to about 16% of the original beam flux (using a 0.1 mm Al foil), no photo-oxidation can be detected once the beam has been attenuated down to 1% of it's original flux (using a 0.25mm Al foil) (data from Moussallam et al., in prep.).

Figure 7

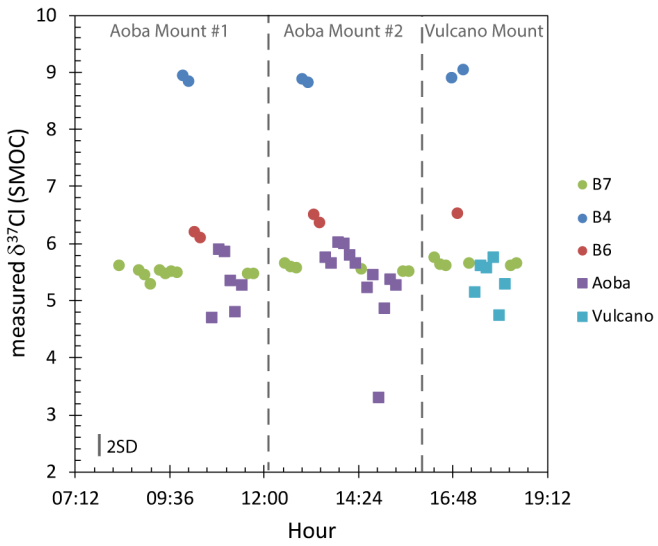
Aoba Mount #1
Aoba Mount #2
Vulcano Mount
measured δ37Cl (SMOC)
10
9
8
7
6
5
4
3
2
2SD
07:12
09:36
12:00
14:24
16:48
19:12
Hour
B7
B4
B6
Aoba
Vulcano

Figure 8

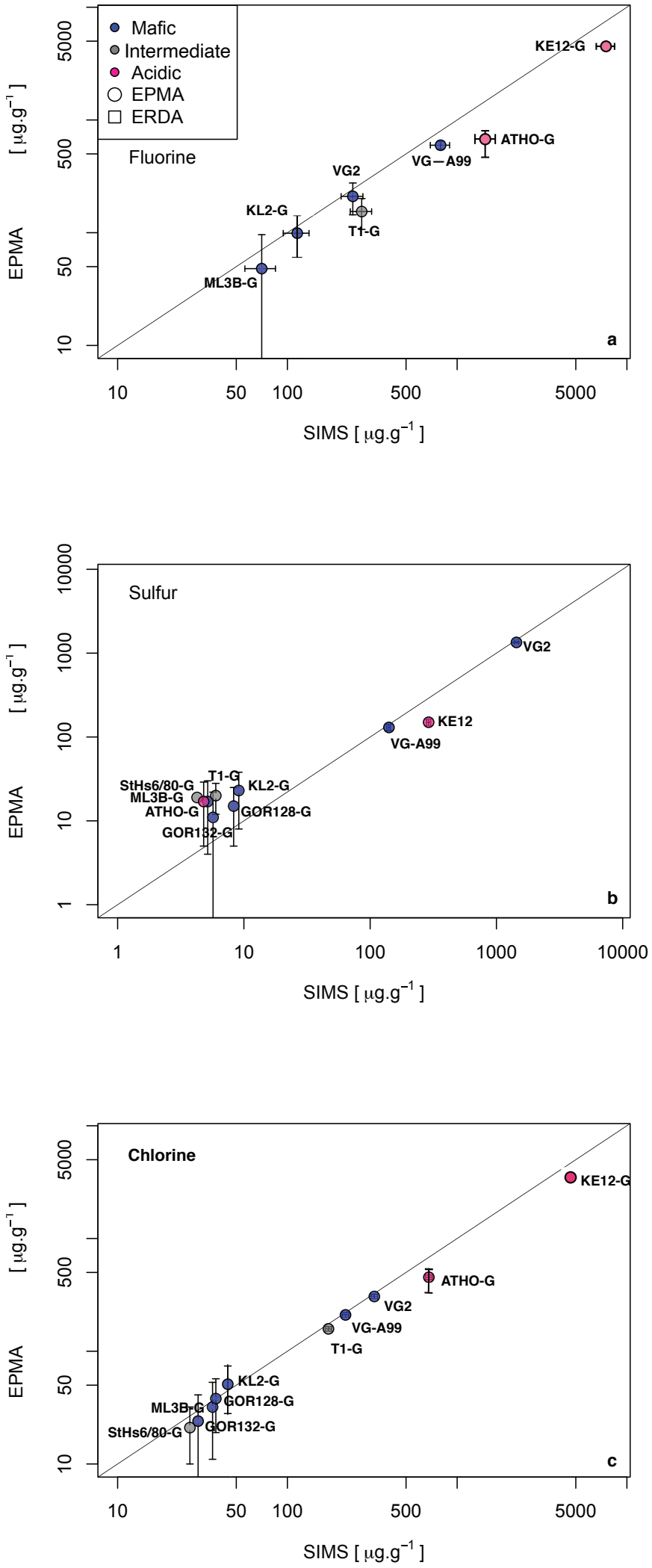
Mafic
Intermediate
Acidic
EPMA
ERDA
Fluorine
KE12-G
ATHO-G
VG—A99
VG2
KL2-G
T1-G
ML3B-G
a
EPMA [μg.g⁻¹]
SIMS [μg.g⁻¹]
10
50
100
500
5000
Sulfur
VG2
KE12
VG-A99
T1-G
StHs6/80-G
ML3B-G
KL2-G
ATHO-G
GOR128-G
GOR132-G
b
1
10
100
1000
10000
Chlorine
KE12-G
ATHO-G
VG2
VG-A99
T1-G
KL2-G
GOR128-G
ML3B-G
GOR132-G
StHs6/80-G
c

Table 1
Click here to download Table: Table templates.docx

Templates of table format for melt inclusion publications

Table: Deposit type, clast size, crystal size and orientation, melt inclusion and vapor bubble sizes.

Sample	Deposit type (lava flow; pyroclastic flow; tephra/ash fallout)	Clast size (cm)	Crystal size (mm)	Crystal orientation	Shortest distance between MI and olivine edge (µm or mm)	Melt inclusion size x(µm)	y(µm)	Bubble size (µm)

Table: Raw major and volatile element compositions of melt inclusions, melt inclusion and vapor bubble sizes (not normalized to 100%).

Sample	SiO_2 (wt. %)	TiO_2 (wt. %)	Al_2O_3 (wt. %)	FeO (wt. %)	MnO (wt. %)	MgO (wt. %)	CaO (wt. %)	Na_2O (wt. %)	K_2O (wt. %)	P_2O_5 (wt. %)	H_2O (wt. %)	CO_2 (ppm)	F (ppm)	S (ppm)	Cl (ppm)

Table: Composition of the olivine hosting the melt inclusions.

Sample	SiO_2 (wt. %)	TiO_2 (wt. %)	Al_2O_3 (wt. %)	FeO (wt. %)	MnO (wt. %)	MgO (wt. %)	CaO (wt. %)	NiO (wt. %)	Total (wt. %)	Mg#

Table : (example of) Trace element compositions of melt inclusions measured by LA-ICPMS.

Sample	Sc (ppm)	Ti (ppm)	Sr (ppm)	Y (ppm)	Zr (ppm)	Nb (ppm)	Ba (ppm)	La (ppm)	Ce (ppm)	Pr (ppm)	Nd (ppm)	Sm (ppm)	Eu (ppm)	Dy (ppm)	Er (ppm)	Yb (ppm)	Hf (ppm)	Pb (ppm)	U (ppm)

Table: Major and volatile element compositions of melt inclusions corrected to be in equilibrium with host olivine.

Sample	SiO_2 (wt. %)	TiO_2 (wt. %)	Al_2O_3 (wt. %)	FeO (wt. %)	MnO (wt. %)	MgO (wt. %)	CaO (wt. %)	Na_2O (wt. %)	K_2O (wt. %)	P_2O_5 (wt. %)	H_2O (wt. %)	CO_2 (ppm)	F (ppm)	S (ppm)	Cl (ppm)	Mg#	±olivine (%)

Table: Trace element corrected compositions.

Sample	SiO_2 (wt. %)	TiO_2 (wt. %)	Al_2O_3 (wt. %)	FeO (wt. %)	MnO (wt. %)	MgO (wt. %)	CaO (wt. %)	Na_2O (wt. %)	K_2O (wt. %)	P_2O_5 (wt. %)	H_2O (wt. %)	CO_2 (ppm)	F (ppm)	S (ppm)	Cl (ppm)	Mg#	±olivine (%)

*Declaration of Interest Statement

Declaration of interests

☒ The authors declare that they have no known competing financial interests or personal relationships that could have appeared to influence the work reported in this paper.

☐The authors declare the following financial interests/personal relationships which may be considered as potential competing interests: